

Optimisation of the  
search for MSSM Higgs Bosons  
in the decay channel

$$A/H/h \rightarrow \tau^+ \tau^- \rightarrow \mu + \tau_{had} + \nu_\mu + 2\nu_\tau$$

with the ATLAS detector

Diplomarbeit  
zur Erlangung des wissenschaftlichen Grades  
Diplom-Physiker

vorgelegt von

Stefanie Langrock  
geboren am 31.01.1988 in Dresden

Institut für Kern- und Teilchenphysik  
der Technischen Universität Dresden  
2012

Eingereicht am 25.05.2012

1. Gutachter: Jun.-Prof. Dr. A. Straessner
2. Gutachter: Prof. Dr. D. Stöckinger

# Abstract

The optimisation of the search for the neutral MSSM Higgs bosons in the decay channel  $A/H/h \rightarrow \tau^+\tau^- \rightarrow \mu + \tau_{had} + \nu_\mu + 2\nu_\tau$  with the ATLAS detector is presented. The ATLAS data of the data taking period in 2011 at  $\sqrt{s} = 7\text{ TeV}$  with an overall integrated luminosity of  $L_{\text{int}} = 4.7\text{ fb}^{-1}$  is used. For the optimisation, multivariate methods such as Boosted Decision Trees and Likelihood Estimators were trained against two of the major backgrounds in this decay channel, the  $W$ +jets background and the QCD background. The training was carried out separately for both backgrounds using a potential signal at  $m_A = 120\text{ GeV}$  and  $\tan\beta = 20$  within the  $m_h^{\text{max}}$  benchmark scenario. The Boosted Decision Trees were found to give the best performance in both cases. An overall background rejection of 57.9% was achieved and the  $\frac{s}{\sqrt{b}}$  significance for the given working point was improved by 8.1% to 4.36.

# Kurzdarstellung

Die Optimierung der Suche nach den neutralen MSSM Higgs Bosonen im Zerfallskanal  $A/H/h \rightarrow \tau^+\tau^- \rightarrow \mu + \tau_{had} + \nu_\mu + 2\nu_\tau$  mit dem ATLAS Detektor wird in dieser Arbeit vorgestellt. Es wurden die ATLAS Daten des Jahres 2011 mit einer Schwerpunktsenergie von  $\sqrt{s} = 7\text{ TeV}$  und einer integrierten Luminosität von  $L_{\text{int}} = 4.7\text{ fb}^{-1}$  verwendet. Um die Suche zu optimieren, wurden multivariate Methoden, wie Boosted Decision Trees und Likelihood Schätzer, gegen zwei der Hauptuntergründe des Zerfallskanals, den  $W$ +jets Untergrund sowie den QCD Untergrund, trainiert. Das Training wurde separat für jeden der Untergründe durchgeführt, unter Annahme einer Signalthypothese mit  $m_A = 120\text{ GeV}$  und  $\tan\beta = 20$  im  $m_h^{\text{max}}$  Benchmark Szenario. In beiden Fällen war das Ergebnis der Boosted Decision Trees das zuverlässigste. Der gesamte Untergrund wurde um 57.9% unterdrückt und die  $\frac{s}{\sqrt{b}}$  Signifikanz für die gewählte Signalthypothese wurde um 8.1% auf 4.36 verbessert.



# Contents

<b>List of Figures</b>	<b>ix</b>
<b>List of Tables</b>	<b>xi</b>
<b>1. Introduction</b>	<b>1</b>
<b>2. Theoretical Framework</b>	<b>3</b>
2.1. The Standard Model . . . . .	3
2.1.1. Overview . . . . .	3
2.1.2. Quantum Chromodynamics . . . . .	5
2.1.3. Electroweak Interaction . . . . .	6
2.1.4. The Higgs Mechanism . . . . .	8
2.2. Supersymmetry . . . . .	11
2.2.1. Motivation . . . . .	11
2.2.2. The Minimal Supersymmetric Standard Model . . . . .	13
<b>3. The LHC and the ATLAS Detector</b>	<b>15</b>
3.1. The LHC . . . . .	15
3.2. The ATLAS Detector . . . . .	18
3.2.1. The ATLAS Coordinate System . . . . .	19
3.2.2. The Magnet System . . . . .	20
3.2.3. The Inner Detector . . . . .	20
3.2.4. The Calorimeter System . . . . .	22
3.2.5. The Muon Spectrometer . . . . .	24
3.2.6. The Forward Detectors . . . . .	25
3.2.7. The Trigger System . . . . .	25
<b>4. Event Selection and Background Estimation</b>	<b>27</b>
4.1. Event Topology . . . . .	27
4.1.1. The Higgs Boson Production . . . . .	27

4.1.2.	The Tau Lepton . . . . .	28
4.1.3.	Background Processes . . . . .	29
4.2.	Event Selection . . . . .	30
4.2.1.	Data Samples and Monte Carlo Simulation . . . . .	30
4.2.2.	Preselection . . . . .	31
4.2.3.	Analysis Level Cuts . . . . .	34
4.3.	Background Estimation . . . . .	36
4.3.1.	W+jets Background . . . . .	36
4.3.2.	QCD Background . . . . .	37
<b>5.</b>	<b>TMVA Analysis</b>	<b>41</b>
5.1.	Multivariate Methods . . . . .	42
5.1.1.	Rectangular Cuts . . . . .	42
5.1.2.	Projective Likelihood Estimator . . . . .	43
5.1.3.	Boosted Decision Trees . . . . .	43
5.2.	Reduction of W+jets Background . . . . .	43
5.2.1.	Variable Decision . . . . .	44
5.2.2.	Multivariate Analysis and Performance . . . . .	46
5.2.3.	Results and Conclusion . . . . .	48
5.3.	Reduction of QCD Background . . . . .	50
5.3.1.	Variable Decision . . . . .	50
5.3.2.	Multivariate Analysis . . . . .	53
5.3.3.	Results and Conclusion . . . . .	54
<b>6.</b>	<b>Systematic Uncertainties</b>	<b>57</b>
6.1.	General Systematics . . . . .	57
6.1.1.	Luminosity . . . . .	57
6.1.2.	Cross-Section . . . . .	57
6.1.3.	Statistical Uncertainties . . . . .	58
6.2.	Systematics on the Muon Candidate . . . . .	59
6.2.1.	Energy Scale . . . . .	59
6.2.2.	Resolution . . . . .	59
6.2.3.	Identification Efficiency . . . . .	59
6.3.	Systematics on the Hadronic Tau Candidate . . . . .	59
6.3.1.	Energy Scale . . . . .	60
6.3.2.	Identification Efficiency . . . . .	60
6.4.	Systematics on the Background Estimation . . . . .	61

6.4.1. W+jets Scaling Factor . . . . .	61
6.4.2. QCD Estimation . . . . .	62
6.5. Results and Conclusion . . . . .	62
<b>7. Results</b>	<b>65</b>
7.1. Signal Efficiency Loss . . . . .	65
7.2. Significance . . . . .	66
7.3. Comparison between Backgrounds and Data . . . . .	66
<b>8. Conclusion</b>	<b>69</b>
<b>A. Appendix - Monte Carlo Samples and Event Selection</b>	<b>71</b>
<b>B. Appendix - Background Estimation</b>	<b>75</b>
<b>C. Appendix - Optimisation of the Event Selection</b>	<b>81</b>
<b>D. Appendix - Systematics</b>	<b>89</b>
<b>E. Appendix - Results</b>	<b>93</b>
<b>Bibliography</b>	<b>99</b>





# List of Figures

2.1.	Feynman diagrams of gluon processes . . . . .	6
2.2.	An example of hadronization . . . . .	7
2.3.	Feynman diagrams of electroweak interactions in $e^+e^-$ -scattering . . . . .	8
2.4.	The Standard Model Higgs Potential . . . . .	9
2.5.	The Standard Model Higgs interaction vertices . . . . .	10
2.6.	Branching Ratios of the Standard Model Higgs . . . . .	11
2.7.	The coupling constant evolution . . . . .	12
3.1.	The injector complex for the LHC . . . . .	17
3.2.	The underground structures of the LHC and LEP . . . . .	18
3.3.	The ATLAS detector with its detector components . . . . .	19
3.4.	A sketch of the ATLAS magnet windings . . . . .	21
3.5.	The ATLAS Inner Detector . . . . .	22
3.6.	The ATLAS calorimeter system . . . . .	23
3.7.	A view of the ATLAS muon spectrometer and its barrel part . . . . .	24
3.8.	A sketch of the ATLAS trigger system . . . . .	26
4.1.	Feynman diagrams of gluon fusion Higgs production . . . . .	28
4.2.	Feynman diagrams of b-associated Higgs production . . . . .	28
4.3.	The $\tau$ -lepton decay . . . . .	29
4.4.	$m_T$ in the $W$ control region before normalisation . . . . .	37
4.5.	$m_T$ in the $W$ control region after normalisation . . . . .	38
4.6.	QCD control regions for background estimation . . . . .	39
4.7.	$m_T$ in the $W$ control region after normalisation with QCD background . . . . .	40
5.1.	Variable Selection for $W$ +jets background reduction . . . . .	44
5.2.	Likelihood and BDT score for training against the $W$ +jets background . . . . .	47
5.3.	Background rejection over signal efficiency for $W$ background analysis . . . . .	48
5.4.	$m_{\text{vis}}$ distribution before and after application of the $\text{BDT}_W$ . . . . .	49
5.5.	Variable Selection for QCD background reduction, BDT and Likelihood . . . . .	52

5.6.	Likelihood and BDT score for training against the QCD background . . . .	53
5.7.	Background rejection over signal efficiency for QCD background analysis .	55
5.8.	$m_{\text{vis}}$ distribution before and after application of the $\text{BDT}_{\text{QCD}}$ . . . . .	56
7.1.	The significance after applying the optimised event selection for different Higgs samples . . . . .	67
7.2.	The final distribution of the visible mass . . . . .	68
B.1.	The $\sum \cos\Delta\Phi$ distribution . . . . .	75
B.2.	$m_{\text{T}}$ in the $W$ +jets control region before renormalisation, logarithmic scale	76
B.3.	Kinematic plots in control region B . . . . .	77
B.4.	Kinematic plots in control region C . . . . .	78
B.5.	Kinematic plots in control region D . . . . .	79
B.6.	Kinematic plots in signal region A . . . . .	80
C.1.	Linear Correlation Coefficients for the Variables involved in $W$ +jets background reduction . . . . .	81
C.2.	Overtraining check for the $W$ +jets background reduction . . . . .	82
C.3.	Linear Correlation Coefficients for the Variables involved in QCD background reduction . . . . .	82
C.4.	Overtraining check for the QCD background reduction . . . . .	83
C.5.	Control plots for QCD training variables I . . . . .	86
C.6.	Control plots for QCD training variables II . . . . .	87
D.1.	$m_{\text{vis}}$ for all Systematics I . . . . .	91
D.2.	$m_{\text{vis}}$ for all Systematics II . . . . .	92
E.1.	Final kinematic plots after new event selection . . . . .	97

# List of Tables

2.1. The leptons in the SM . . . . .	4
2.2. The quarks in the SM . . . . .	4
2.3. The gauge bosons in the SM . . . . .	4
2.4. The particle content of the MSSM . . . . .	14
2.5. MSSM Higgs content . . . . .	14
4.1. Event yield after the event selection . . . . .	35
4.2. Event yield for the three QCD control regions . . . . .	39
5.1. Separation and Discrimination Significance for the $W$ +jets background . .	47
5.2. Event yields after application of multivariate methods against the $W$ +jets background . . . . .	49
5.3. Event Selection for QCD background reduction with and without applied BDT $_W$ . . . . .	51
5.4. Separation and Discrimination Significance for the QCD background . . . .	54
5.5. Event yields after application of multivariate methods against the QCD background . . . . .	55
6.1. General systematic uncertainties and statistical uncertainties for all samples	58
6.2. Muon systematic uncertainties for all samples . . . . .	60
6.3. Tau systematic uncertainties for all samples . . . . .	61
6.4. Systematic Uncertainties on background estimation . . . . .	63
6.5. Combined relative uncertainties . . . . .	63
7.1. Signal efficiency loss for different Higgs masses $m_A$ . . . . .	66
7.2. Final event yields after applying new selection with uncertainties . . . . .	68
A.1. Background Monte Carlo Samples . . . . .	71
A.2. Signal Monte Carlo Samples . . . . .	72
A.3. Masses for MSSM Higgs bosons . . . . .	72
A.4. Event Preselection . . . . .	73

A.5. LAr Hole Treatment . . . . .	74
A.6. Analysis Level Selection . . . . .	74
B.1. Control region cuts for the QCD background estimation . . . . .	76
C.1. Variables considered for multivariate training . . . . .	83
C.2. Configuration options for multivariate training, $W$ +jets . . . . .	84
C.3. Configuration options for multivariate training, QCD . . . . .	85
D.1. Systematic uncertainties for the energy scale of the hadronic tau . . . . .	89
D.2. Event yield for the three QCD control regions after applying the new event selection . . . . .	89
D.3. Statistical Uncertainties for the QCD control regions . . . . .	90
D.4. Total Systematic Uncertainties for the QCD control regions . . . . .	90
E.1. The Event yield for different Higgs masses and $\tan\beta$ before applying the new event selection . . . . .	93
E.2. The Event yield for different Higgs masses and $\tan\beta$ after applying the new event selection . . . . .	93
E.3. The Event yield for different Higgs masses and $\tan\beta$ after applying a different event selection I . . . . .	94
E.4. The Event yield for different Higgs masses and $\tan\beta$ after applying a different event selection II . . . . .	94
E.5. The Event yield for different Higgs masses and $\tan\beta$ after applying a different event selection III . . . . .	94
E.6. The Event yield for different Higgs masses and $\tan\beta$ after applying a different event selection IV . . . . .	95
E.7. The Event yield for different Higgs masses and $\tan\beta$ after applying a different event selection V . . . . .	95
E.8. The Event yield for different Higgs masses and $\tan\beta$ after applying a different event selection VI . . . . .	95
E.9. The Event yield for different Higgs masses and $\tan\beta$ after applying a different event selection VII . . . . .	96
E.10. The Event yield for different Higgs masses and $\tan\beta$ after applying a different event selection VIII . . . . .	96

# 1. Introduction

The Standard Model of particle physics was developed throughout the 20th century. It describes three of the four known interactions with great precision. Within the Standard Model, the mechanism, which causes electroweak symmetry breaking, is implemented. This mechanism is responsible for the fermions in the Standard Model and three of the known gauge bosons gaining mass. An experimental proof for this mechanism is the only theoretical prediction of the Standard Model, which still needs to be found. This experimental proof is finding the scalar particle required by this mechanism, the Higgs boson. Discovering the origin of mass is one of the main purposes of the LHC and the ATLAS detector at CERN in Geneva.

In the minimal supersymmetric extension of the Standard Model (MSSM), the mechanism leads to five Higgs bosons, three neutral ones ( $A/H/h$ ) and two charged ones ( $H^\pm$ ). This thesis concentrates on the search of the three neutral MSSM Higgs bosons. With a branching ratio of  $\sim 10\%$  for the  $A/H/h \rightarrow \tau\tau$  decay, this decay channel is a very promising search channel. As final state for the  $\tau\tau$  decay, the semileptonic decay is considered. More specifically, this work concentrates on the muon-hadron final state. Thus, one of the two tau leptons decays into a muon ( $\tau \rightarrow \mu + \nu_\mu + \nu_\tau$ ), the other one decays hadronically. The branching ratio for this semileptonic decay channel of the  $\tau\tau$  decay is  $23\%$  [1].

In order to optimise the MSSM Higgs boson search in the  $A/H/h \rightarrow \tau^+\tau^- \rightarrow \mu + \tau_{had} + \nu_\mu + 2\nu_\tau$  decay channel, several multivariate methods are trained and compared with respect to output performance, background rejection and signal efficiency loss. The optimisation will concentrate on two of the main backgrounds in this decay channel, the  $W$ +jets background and the QCD background. The multivariate method with the best overall performance is then included in the event selection.

The thesis starts with a brief overview of the theoretical background. The Standard Model is described as well as an introduction to the Minimal Supersymmetric Standard Model is given. In the following chapter, the LHC and the ATLAS detector are portrayed. Before the multivariate methods are trained and applied, the event topology, the event selection and the background estimation have to be understood and employed, as outlined in Chapter 4. Then, the training and selection of the multivariate methods for the

background reduction of the  $W$ +jets and QCD events are described. In Chapter 6, the systematic uncertainties considered are discussed. Finally, the results are summarised and a conclusion and outlook for future analyses is given.

# 2. Theoretical Framework

## 2.1. The Standard Model

The Standard Model (SM) of particle physics is a well developed theoretical framework, which describes elementary particles and their interaction. This theory is tested to a very high degree, to which it precisely defines three of the known types of particle interaction (strong, electromagnetic and weak) [2] [3]. In this section, a brief overview of the SM and the involved particles and interactions is given. This is followed by a more detailed description of the Quantum Chromodynamics (QCD), the gauge symmetry which represents the strong interaction. The section will be finished by an illustration of the electroweak SM and, closely linked to that, the Higgs mechanism.

### 2.1.1. Overview

In the SM, a distinction is made between two types of particles: the matter particles and the interaction particles. These particles have presently no known substructure and can thus be described as point-like. Therefore, the particles are called elementary particles, referring to them being the basic elements of the universe.

The elementary particles can be separated into fermions with spin  $s = \frac{1}{2}$  and bosons with an integer spin of  $s = 1$ . The matter particles (the fermions) are categorised into quarks and leptons. Each of them occur in three generations, which are summarised with their properties in Table 2.1 and Table 2.2. Gauge bosons, the interaction particles, mediate the known SM processes. All gauge bosons are briefly characterised in Table 2.3 [3].

Theoretically, the SM is described by gauge symmetries and a set of Lagrangians. This leads to the gauge group of

$$SU(3)_C \times SU(2)_L \times U(1)_Y. \quad (2.1)$$

$SU(3)_C$  corresponds to the QCD, whilst  $SU(2)_L \times U(1)_Y$  is needed in the electroweak theory. The electromagnetic interaction is a subset of the electroweak symmetry and is defined by the symmetry group  $U(1)_{em}$ . Since the gauge bosons of the weak interaction

Generation	Leptons	Charge $Q$	Weak isospin $ I_3 $		Mass/MeV
			left-handed	right-handed	
1	$e$	$\pm 1$	$1/2$	0	0.511
	$\nu_e$	0	$1/2$	none	$< 2 \cdot 10^{-6}$
2	$\mu$	$\pm 1$	$1/2$	0	105.66
	$\nu_\mu$	0	$1/2$	none	$< 2 \cdot 10^{-6}$
3	$\tau$	$\pm 1$	$1/2$	0	1776.99
	$\nu_\tau$	0	$1/2$	none	$< 2 \cdot 10^{-6}$

**Table 2.1.:** The leptons in the SM and their properties [4].

Generation	Quarks	Charge $Q$	Weak isospin $ I_3 $		Color
			left-handed	right-handed	
1	down	$\pm 1/3$	$1/2$	0	red, blue, green
	up	$\pm 2/3$	$1/2$	0	red, blue, green
2	strange	$\pm 1/3$	$1/2$	0	red, blue, green
	charm	$\pm 2/3$	$1/2$	0	red, blue, green
3	bottom	$\pm 1/3$	$1/2$	0	red, blue, green
	top	$\pm 2/3$	$1/2$	0	red, blue, green

**Table 2.2.:** The quarks in the SM and their properties [4].

Boson	Interaction	Charge $Q$		Color	Mass/GeV
Photon $\gamma$	electromagnetic	0		none	0
$Z$	weak	0		none	91.2
$W^\pm$	weak	$\pm 1$		none	80.4
Gluon $g_\alpha, \alpha = 1, \dots, 8$	strong	0	1 color and 1 anticolor		0

**Table 2.3.:** The gauge bosons in the SM and their properties [4].



are not massless, as shown in Table 2.3, the electroweak symmetry has to be spontaneously broken. Hence, the Higgs mechanism was added to the theory, which lead to an additional particle in the SM. This new particle, the Higgs boson  $H$ , is scalar, i.e. has a spin of  $s = 0$ , and has no electromagnetic charge [3] [5].

### 2.1.2. Quantum Chromodynamics

The strong interaction of the SM is described by the gauge theory of Quantum Chromodynamics (QCD). The gauge bosons mediating the strong interaction are the gluons, which couple to  $N_C = 3$  color charges.

There are three different types of color charge with their corresponding anti-colors, which are a property of quarks as well as gluons. Thus, gluons cannot only couple to quarks, but also to themselves, which is why three- and four-gluon vertices occur in nature. An example of gluon interaction is shown in Figure 2.1, where also examples of three- and four-gluon vertices are depicted. Gluons always carry a color and an anti-color, hence eight different kinds of gluons exist. Quarks  $q$  are carriers of color, whilst the anti-color is found to be a property of antiquarks  $\bar{q}$ . As already stated in Section 2.1.1, there are three generations of quarks, each with an up-type (up  $u$ , charm  $c$ , top  $t$ ) and a down-type quark (down  $d$ , strange  $s$ , bottom  $b$ ). The quark masses  $m_q$  as well as the strong coupling constant  $g_s$  are the fundamental parameters of the SM and QCD [4].

The quarks  $u$ ,  $d$ ,  $s$ ,  $c$  and  $b$  hadronize into mesons (a  $q\bar{q}$ -combination) or baryons (a  $qqq$ -combination), i.e. free quarks have never been observed <sup>1</sup>. Hence, only color-neutral particles can be found, as these hadrons (mesons and baryons) are color-singlet quark and gluon compositions. The attempt to free a quark from a hadron results in the production of more hadrons. By trying to separate two quarks from each other, the field energy between the quarks is increasing until it is high enough, to create a new  $q\bar{q}$ -pair. With these new particles, the original quarks form new hadrons, i.e. color-neutral particles. This behaviour is called confinement and can lead to a shower of hadrons [6]. In the detector, these showers form collimated bunches, which are called jets [4]. Figure 2.2 shows the process of hadronization in an  $e^+e^-$ -collision after the formed gauge boson decays into a pair of quarks.

---

<sup>1</sup>The top quark  $t$  has a very short lifetime, because of its mass. Therefore it decays before it has time to hadronize [6].

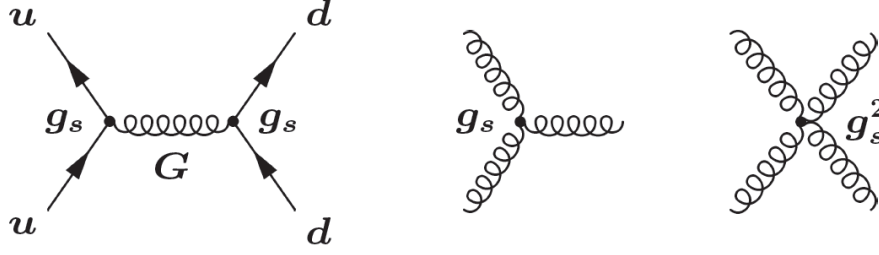


**Figure 2.1.:** Feynman diagrams of gluon processes, with examples of gluon exchanges between quarks, as well as three and four gluon interaction [7].

### 2.1.3. Electroweak Interaction

The electroweak SM is constructed from the gauge group  $SU(2)_L \times U(1)_Y$ , with the elementary fermions representing this group. The left handed fermion fields form doublets, whilst the right-handed ones transform as singlets:

$$\begin{aligned}
 & \begin{pmatrix} \nu_e \\ e \end{pmatrix}_L, \quad \begin{pmatrix} \nu_\mu \\ \mu \end{pmatrix}_L, \quad \begin{pmatrix} \nu_\tau \\ \tau \end{pmatrix}_L, \quad e_R, \quad \mu_R, \quad \tau_R & \text{for leptons} \\
 & \begin{pmatrix} u \\ d' \end{pmatrix}_L, \quad \begin{pmatrix} c \\ s' \end{pmatrix}_L, \quad \begin{pmatrix} t \\ b' \end{pmatrix}_L, \quad d_R, \quad d_R, \quad c_R, \quad s_R, \quad t_R, \quad b_R & \text{for quarks}
 \end{aligned} \tag{2.2}$$

These multiplets can be described with three quantum numbers:  $I$  (weak isospin),  $I_3$  (third component of the weak isospin) and  $Y$  (weak hypercharge).  $I_3$  and  $Y$  fulfill the Gell-Mann-Nishima relation, which links them to the electric charge  $Q$ :

$$Q = I_3 + \frac{Y}{2}. \tag{2.3}$$

The isospin components  $I_{1,2,3}$  are connected to a triplet of vector fields  $W_\mu^i$ ,  $i = 1, 2, 3$ , whilst a singlet field  $B_\mu$  relates to  $Y$  [9]. The analogous gauge coupling constants are  $g$  and  $g'$  respectively [4].

The two neutral vector fields mix into the physical gauge bosons  $Z_\mu$  and  $A_\mu$ , where  $Z_\mu$  corresponds to the  $Z$  boson and  $A_\mu$  describes the photon field. This mixing can be described as a rotation with the Weinberg angle  $\Theta_W$ :

$$\begin{aligned}
 |A_\mu\rangle &= \cos\Theta_W |B_\mu\rangle - \sin\Theta_W |W_\mu^3\rangle \\
 |Z_\mu\rangle &= \sin\Theta_W |B_\mu\rangle + \cos\Theta_W |W_\mu^3\rangle
 \end{aligned} \tag{2.4}$$

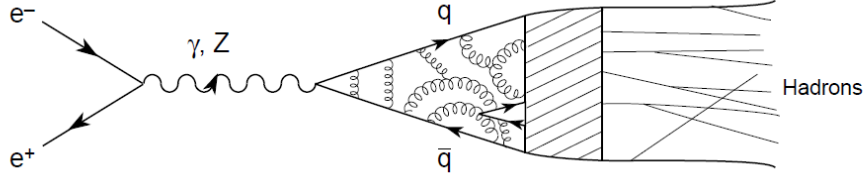


**Figure 2.2.:** An example of hadronization after an  $e^+e^-$ -collision [8].

The two remaining weak eigenstates  $W_\mu^1, W_\mu^2$  combine to the two charged mass eigenstates  $W^\pm$  [9]. The vector bosons can also couple to themselves, which is why three and four gauge boson vertices occur, as can be seen in Figure 2.3.

Depending on the nature of the vector bosons transmitting the weak interaction, a distinction can be made between charged currents ( $W^\pm$ ) and neutral currents ( $Z$ ). Charged currents only occur for left-handed fermions, since  $W^\pm$  only couple to particles with this chirality. The neutral current interaction has both, left- and right-handed couplings [10]. The left- and right-handed components are defined by the  $\gamma_5$ -operator<sup>2</sup>, e.g [3]:

$$\begin{aligned} e_L^- &= \frac{1}{2} (1 - \gamma_5) e^- \\ e_R^- &= \frac{1}{2} (1 + \gamma_5) e^- \end{aligned} \quad (2.5)$$

Another important aspect of the electroweak interaction is the quark mixing. The electroweak eigenstates of the quarks, which couple to the  $W^\pm$  vector bosons, are a superposition of the mass eigenstates of the quarks. The coupling strength of the  $W^\pm$  bosons to the quarks, is given by the Cabbibo-Kobayashi-Maskawa matrix (CKM) [4]:

$$V_{\text{CKM}} = \begin{pmatrix} V_{ud} & V_{us} & V_{ub} \\ V_{cd} & V_{cs} & V_{cb} \\ V_{td} & V_{ts} & V_{tb} \end{pmatrix}. \quad (2.6)$$

The matrix elements thus provide the linear coefficients for the quark mixing, e.g. the electroweak eigenstate  $|d'\rangle$  composes from the mass eigenstates with:

$$|d'\rangle = V_{ud} |d\rangle + V_{us} |s\rangle + V_{ub} |b\rangle \quad (2.7)$$

---

<sup>2</sup> $\gamma_5 = i\gamma_0\gamma_1\gamma_2\gamma_3$ , with  $\gamma_i$  being the gamma matrices (see e.g. [11] for further information)

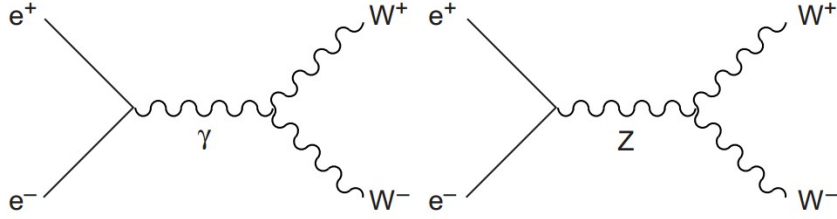


**Figure 2.3.:** Feynman diagrams of electroweak interactions in  $e^+e^-$ -scattering with three boson vertices [12].

The probability of an up-type quark  $q_i$  decaying via weak interaction into a down-type quark  $q_j$  is given by  $|V_{q_i q_j}|^2$  [13][4].

#### 2.1.4. The Higgs Mechanism

In order to construct masses for  $W^\pm$  and  $Z$ , the Higgs mechanism has to be employed to the electroweak gauge theory. Since the photon is massless, the electromagnetic symmetry group  $U(1)_{em}$  must provide a good vacuum symmetry. Thus, the mechanism applied, has to follow the pattern:

$$SU(3)_C \times SU(2)_L \times U(1)_Y \rightarrow SU(3)_C \times U(1)_{em} \quad (2.8)$$

To implement symmetry breaking, a scalar field  $\Phi$  is applied. More specifically, the self-interaction of  $\Phi$ , which is described by a potential  $V(\Phi)$ , employs the symmetry breaking. The Lagrangian and the self-interaction of  $\Phi$  are proposed to be

$$\begin{aligned} L_{SBS} &= (D_\mu \Phi)^\dagger (D^\mu \Phi) - V(\Phi) \\ V(\Phi) &= \mu^2 \Phi^\dagger \Phi + \lambda (\Phi^\dagger \Phi)^2; \lambda > 0 \end{aligned} \quad (2.9)$$

in the simplest possible way. The scalar field  $\Phi$  has two components:

$$\Phi = \begin{pmatrix} \Phi^+ \\ \Phi^0 \end{pmatrix}. \quad (2.10)$$

The coupling of the electroweak vector fields to  $\Phi$  is introduced using the covariant derivative [3]:

$$D_\mu = \partial_\mu - \frac{1}{2}ig\vec{\sigma} \cdot \vec{W}_\mu - \frac{1}{2}ig'B_\mu. \quad (2.11)$$

If the parameter  $\mu^2$  in the potential  $V(\Phi)$  is chosen to be negative, the field  $\Phi$  has a non-vanishing vacuum expectation value

$$\langle \Phi \rangle = \frac{1}{\sqrt{2}} \begin{pmatrix} 0 \\ v \end{pmatrix}. \quad (2.12)$$

In this case, the potential has the form shown in Figure 2.4, which is why it is often referred to as the "mexican hat" potential. Approximating the vacuum value around the minimum and using a gauge transformation then leads to

$$\Phi = \frac{1}{\sqrt{2}} \begin{pmatrix} 0 \\ v + H \end{pmatrix} \quad (2.13)$$

$H$  is a real field, which describes a new scalar, massive particle with no electric charge. The mass of this Higgs boson can be determined by [9]

$$M_H = \sqrt{2}\mu. \quad (2.14)$$

The result of the spontaneous symmetry breaking is the weak bosons gaining masses by coupling to the Higgs field:

$$\begin{aligned} M_W^2 &= \frac{\pi\alpha}{\sqrt{2}G_\mu} \cdot \frac{1}{\sin^2\Theta_W} \\ M_Z^2 &= \frac{\pi\alpha}{\sqrt{2}G_\mu} \cdot \frac{1}{\sin^2\Theta_W \cos^2\Theta_W} \end{aligned} \quad (2.15)$$

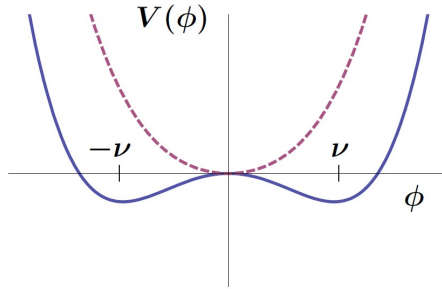


**Figure 2.4.:** The Standard Model Higgs Potential for the cases of  $\mu^2 < 0$  (solid blue) and  $\mu^2 > 0$  (dashed purple) [7].

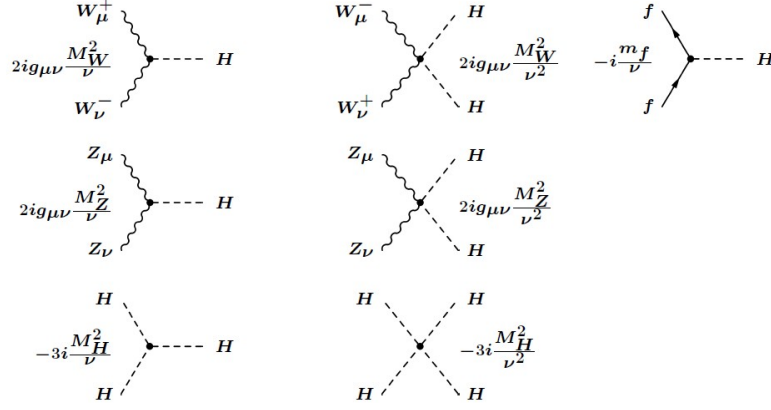


**Figure 2.5.:** The Standard Model Higgs interaction vertices for the SM particles [7].

Here,  $\alpha = \frac{e^2}{4\pi}$  and  $e$  is the elementary electric charge:

$$e = \frac{gg'}{g^2 + g'^2}. \quad (2.16)$$

In this breaking algorithm, one unbroken phase symmetry remains. Therefore, the photon, with the coupling constant  $e$ , stays massless.

A value for the vacuum expectation value  $v$  can be obtained from charged-current interactions:

$$v = \left( G_F \sqrt{2} \right)^{-\frac{1}{2}} \approx 246 \text{ GeV} \quad (2.17)$$

with  $G_F$  being the Fermi coupling constant. The fermion masses arise from Yukawa couplings to the scalar field [14]. The possible interaction vertices of the SM Higgs with the SM particles are summarised in Figure 2.5. Figure 2.6 shows the branching ratios of the SM Higgs for different decay channels, depending on the yet to be determined Higgs mass  $m_H$ .

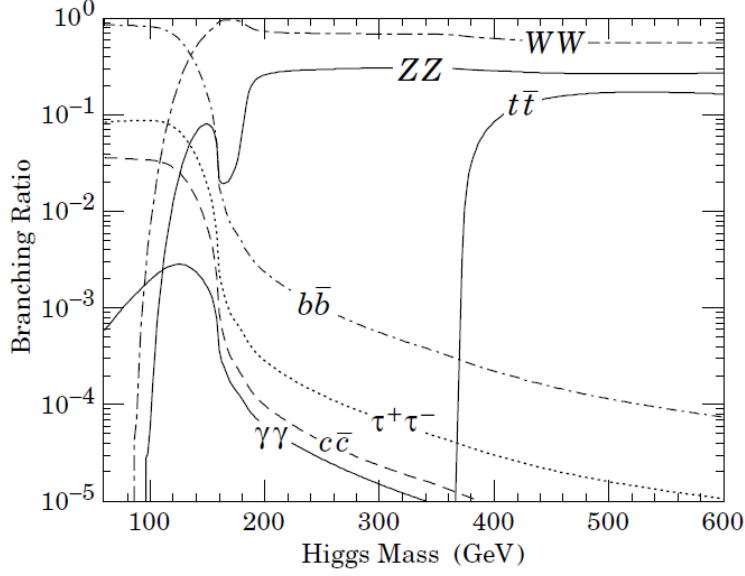


**Figure 2.6.:** Branching Ratios of the Standard Model Higgs [3].

## 2.2. Supersymmetry

The SM describes occurring physical phenomena very well, but it is clear, that it cannot provide an answer to the unsolved problems in particle physics. Therefore, the SM needs to be extended. Supersymmetry, which essentially describes a fermion-boson symmetry, is one possible extension of the SM. To date it has not been observed, it is merely a theoretical construction, which provides answers to the open questions of the SM [15] [16]. In this section, the motivation for introducing supersymmetry is outlined, followed by a brief description of the minimal supersymmetric extension of the SM.

### 2.2.1. Motivation

Especially with respect to a potential Grand Unified Theory (GUT), the SM does not provide satisfying solutions to all occurring problems. The main limitations of the SM, which can be solved by introducing Supersymmetry (SUSY), are described in this section.

The hierarchy problem occurs, when one tries to extend the SM to describe physics with higher energies. Especially the Higgs field proves to be very sensitive to any addition to the SM. More specifically, any particle that couples to the Higgs field in one way or

another, results in heavy quantum corrections for  $m_H^2$ . These corrections are at least of the order of magnitude of the energy scale, where the new physics would occur. For the GUT framework this would be the planck scale  $M_P$ . All known physics takes place at the weak scale  $M_W$ . If those corrections are of order  $M_P$ , the corrections for  $m_H^2$  would exceed the value of  $m_H^2$  by at least 30 orders of magnitude. Thus, a new symmetry, which relates fermions and bosons is needed, to provide a cancellation of these enormous contributions to  $\Delta m_H^2$ . Supersymmetry naturally provides a particle content with the necessary properties, to solve the problem [15] [17].

Closely related to this, with respect to a GUT, is the possible unification of the gauge couplings. As seen in Figure 2.7, in the SM the gauge couplings do not unify when extrapolated to high energies. If, however, the particle content of the SM is extended by SUSY, they naturally meet at an energy scale of  $M_U \approx 2 \cdot 10^{16}$  GeV. This indicates a possible GUT, of which the SM would represent the low energy limit.

Last but not least, SUSY could also answer the Dark Matter (DM) problem. Sufficient evidence for the existence of DM has been observed, but the nature of non-baryonic DM has not yet been uncovered. DM particles only interact weakly and gravitationally. The only known particles with these properties are the neutrinos. However, even with adding the observation of massive neutrinos to the SM, the observed upper limits on neutrino masses are too low to explain the gravitational effects of DM. The particle content of SUSY, however, offers a great DM candidate, the lightest supersymmetric particle (LSP). For reasons outlined in the next section, the LSP can only be destroyed through annihilation with itself [17].

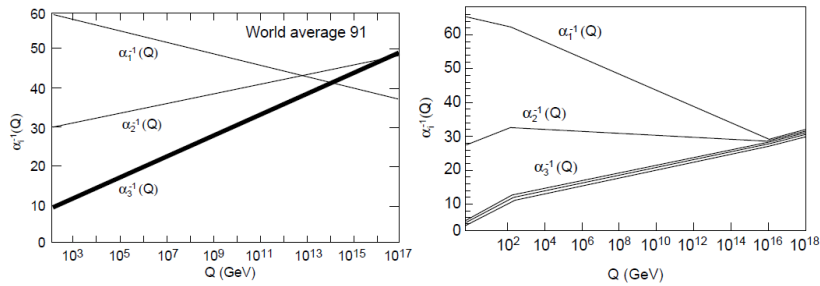


**Figure 2.7.:** The coupling constant evolution as measured at the LEP for SM (left) and SUSY (right) [17].



### 2.2.2. The Minimal Supersymmetric Standard Model

The Minimal Supersymmetric Standard Model (MSSM) is the minimal possible extension to the SM, i.e. it holds the smallest possible field content required [17]. A transformation in supersymmetry, essentially, turns a fermionic state into a bosonic state. The fermionic anticommuting operator  $Q$  is responsible for this transformation [15]:

$$\begin{aligned} Q |\text{Boson}\rangle &= |\text{Fermion}\rangle \\ Q |\text{Fermion}\rangle &= |\text{Boson}\rangle \end{aligned} \quad (2.18)$$

Consequently, all gauge fields ( $g$ ,  $W$ ,  $B$ ) have fermionic superpartners, namely the gluinos, winos and binos. Equally, all SM fermions get scalar superpartners, the sfermions, which are called squarks and sleptons [17].

Both superpartners, i.e. the fermion and the boson state of a particle, are combined in supermultiplets. The properties of the supersymmetric generator  $Q$  ensure, that each particle in a supermultiplet is in the same gauge group. Hence, they have to have the same electric charges, weak isospin and color charge. For sparticles, the same symbols are used as for their standard model superpartners, the only addition is a tilde on top of the letter [15]. Table 2.4 summarises the particle content of the MSSM.

In the MSSM, an additional Higgs field is presented, leading to two doublets  $H_1$ ,  $H_2$ . The two Higgs doublets are defined in Equation 2.19, and the corresponding Higgs potential can be described with two parameters,  $\tan\beta = \frac{v_1}{v_2}$  and  $m_A^2$ , which are independent from each other. Here,  $v_1$  and  $v_2$  are the vacuum expectation values of the two Higgs fields respectively and  $m_A$  is the mass of the neutral  $\mathcal{CP}$ -odd Higgs boson. These Higgs doublets lead to five physical Higgs bosons, which are summarised in Table 2.5 [18].

$$\begin{aligned} H_1 &= \begin{pmatrix} H_1^0 \\ H_1^- \end{pmatrix} = \begin{pmatrix} v_1 + \frac{1}{\sqrt{2}} (\phi_1^0 + i\chi_1^0) \\ -\phi_1^- \end{pmatrix} \\ H_2 &= \begin{pmatrix} H_2^+ \\ H_2^0 \end{pmatrix} = \begin{pmatrix} \phi_2^+ \\ v_2 + \frac{1}{\sqrt{2}} (\phi_2^0 + i\chi_2^0) \end{pmatrix} \end{aligned} \quad (2.19)$$

In SUSY, an additional quantum number is introduced, the  $R$ -parity, which is conserved in the MSSM. It is defined as

$$R = (-1)^{3B+L+2s}, \quad (2.20)$$

where  $B$  is the baryon number,  $L$  is the lepton number and  $s$  is the spin. For all SM particles,  $R = 1$  applies, whilst for their superpartners  $R = -1$  is valid. Hence, if the  $R$ -parity is conserved, sparticles can only decay into an uneven amount of other sparticles. Therefore, the lightest sparticle will be unable to decay [17].

SM particles		Supersymmetric partners		
particles	spin	particles	name	spin
$q$	1/2	$\tilde{q}_L, \tilde{q}_R$	squark	0
$l$	1/2	$\tilde{l}_L, \tilde{l}_R$	slepton	0
$\nu$	1/2	$\tilde{\nu}$	sneutrino	0
$g$	1	$\tilde{g}$	gluino	1/2
$W_i, i = 1, 2, 3$	1	$\tilde{W}_i$	wino	1/2
$B$	1	$\tilde{B}$	bino	1/2
$H^\pm$	0	$\tilde{H}^\pm$	higgsino	1/2
$H_i^0, i = 1, 2, 3$	0	$\tilde{H}_j^0, j = 1, 2$	higgsino	1/2

**Table 2.4.:** The particle content of the MSSM, adapted from [17].

number	electric charge	$\mathcal{CP}$	symbol
2	0	+1 ( $\mathcal{CP}$ -even)	$h, H$
1	0	-1 ( $\mathcal{CP}$ -odd)	$A$
2	$\pm 1$		$H^\pm$

**Table 2.5.:** The MSSM Higgs bosons [18].

## 3. The LHC and the ATLAS Detector

### 3.1. The LHC

The Large Hadron Collider (LHC) is a two ring superconducting hadron accelerator and collider. Its purpose is to uncover physics beyond the Standard Model. Thus, it was constructed to collide proton beams with a center of mass energy of  $\sqrt{s} = 14$  TeV, as well as heavy ion beams (Pb beams) with  $\sqrt{s} = 2.8$  TeV [19]. The tunnel in which it was installed was previously used for the Large Electron Positron Collider (LEP). This tunnel has a circumference of 26.7 km and is located between 50 to 175 m underground [20]. In 1989, the LEP started operating and it was closed down in 2000, to be replaced by the LHC.

One of the key differences between the LHC and the LEP are the type of particles which are accelerated in the beam line. Unlike the LEP, the LHC is a particle - particle collider. For the particle - anti-particle collisions that took place in the LEP, the tunnel was built with an internal diameter of 3.8 m [20]. Since electrons and positrons can share the same phase space in the ring, only one collider ring had to be designed and fitted into the tunnel. Being a particle - particle accelerator, the LHC needs two rings to provide counter-rotating beams. There was not enough room in the 3.8 m-wide tunnel to install two separate rings of magnets, which are necessary to keep the particles on the beam line. Thus, the LHC uses twin bore magnets on both rings, with two sets of coils. The rest of the mechanical structure and the cryostatic system are the same for the two beam channels. The tunnel also consists of eight arcs and eight straight lines, in which the collision points are located. There are in total 4 interaction points, where the two beam lines cross each other and where the experimental detectors are located [19]. The main magnetic bending field is applied by 1232 superconducting dipole magnets, which are located around the ring. During operation, they are cooled down to a temperature of 1.9 K by super fluid helium [21]. The collider peak energy depends on the magnetic field applied by those dipole magnets. For a proton energy of 7 TeV, a magnetic field of 8.33 T needs to be

applied [19].

The particles colliding at the LHC undergo a preacceleration to meet the requirements needed by the LHC. This preacceleration is performed by two different set-ups for the proton beams and the Pb beams. One proton beam in the LHC consists of 2808 high intensity proton bunches with a 25 ns bunch spacing between each bunch [22]. Such a proton bunch, which is a collection of protons seized into a restricted region, contains  $1.15 \cdot 10^{11}$  protons [21]. In order to provide these proton bunches, they have to be sent through an injection chain, which includes four different stages. The primary proton source at CERN is the linear accelerator Linac2, which delivers protons for the whole accelerator complex. In the Linac2, the protons gain an energy of 50 MeV. From there they are transported to the Proton Synchrotron Booster (PSB) via an 80 m long beam line. Leaving the PSB with an energy of 1.4 GeV, the protons are passed on to the Proton Synchrotron (PS). Here, they are accelerated up to 25 GeV, before they reach the final link of the injector chain. In the Super Proton Synchrotron (SPS), the protons attain an energy of 450 GeV. Over two transfer lines, these protons are then injected into the LHC [22][19]. Figure 3.1 shows a sketch of the LHC injector system.

In order to operate the LHC as an ion collider, a slightly different injection chain is needed. As shown in Figure 3.1, instead of the Linac2, the ion linear accelerator Linac3 represents the first part of the chain. Also, due to insufficient ion phase-space density produced by the PSB, the second part is replaced by the Low Energy Ion Ring (LEIR) [22].

Once the proton beams are injected into the LHC, they can be brought to collision at each of the interaction points. The generated number of collision events can be evaluated with

$$N_{\text{event}} = L \cdot \sigma_{\text{event}} \quad (3.1)$$

where  $\sigma_{\text{events}}$  describes the cross-section of the investigated event type.  $L$  is the machine luminosity, which can be calculated by using the beam parameters of the operation. Assuming a Gaussian beam distribution leads to the luminosity:

$$L = \frac{N_b^2 n_b f_{\text{rev}} \gamma_r}{4\pi \epsilon_n \beta^*} F \quad (3.2)$$

in which  $N_b$  represents the number of particles per bunch and  $n_b$  is the number of bunches per beam. Those are multiplied by the revolution frequency  $f_{\text{rev}}$  and the relativistic gamma factor  $\gamma_r$ , whilst  $\epsilon_n$  stands for the normalized transverse beam emittance. The beta function at the interaction point is described by the parameter  $\beta^*$ . Finally, the factor  $F$  is called the luminosity reduction factor, which is an effect of the crossing angle at the collision point

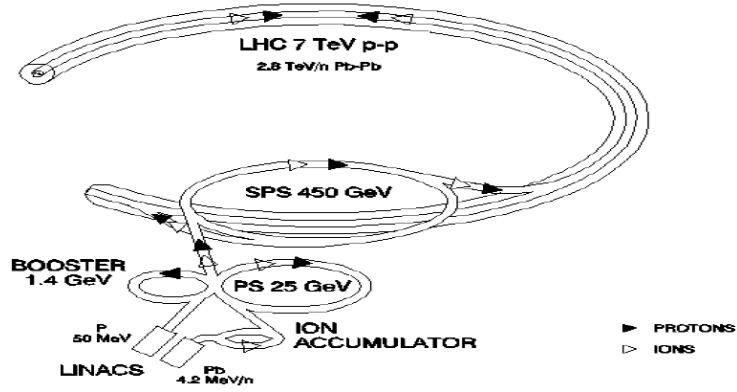


**Figure 3.1.:** The injector complex for the LHC [19]

[19].

Over a physics run, the luminosity is not constant. It reduces mainly due to beam losses from the collisions. This decay can be described as a function of time and henceforth a luminosity lifetime can be determined. This can be used to define the integrated luminosity, another essential variable, which is generally used in ATLAS publications. To define the integrated luminosity, the initial machine luminosity from Equation 3.2 is integrated over one data run time, which gives

$$L_{\text{int}} = L\tau_L [1 - e^{-T_{\text{run}}/\tau_L}] . \quad (3.3)$$

$T_{\text{run}}$  describes the full time of one luminosity run and the luminosity lifetime is represented by  $\tau_L$  [19].

At the four collision points, the four main LHC experiments are located. Figure 3.2 shows the underground structure of the LHC compared to the LEP underground structure. Two high luminosity and multi-purpose experiments at the LHC are ATLAS (A Toroidal LHC ApparatuS, [23]) at point 1 and CMS (Compact Muon Solenoid, [24]) at point 5, which are aiming at a peak luminosity of  $L = 10^{34} \text{ cm}^{-2}\text{s}^{-1}$  [19]. At the collision points 2 and 8 the two other main experiments are located. Positioned at point 8 is the LHCb experiment, which investigates B hadron decays and achieves precision measurements on CP violation [25]. The aimed peak luminosity of the LHCb is  $L = 10^{32} \text{ cm}^{-2}\text{s}^{-1}$ , thus the LHCb is a low luminosity experiment [19]. ALICE (A Large Ion Collider Experiment, [27])

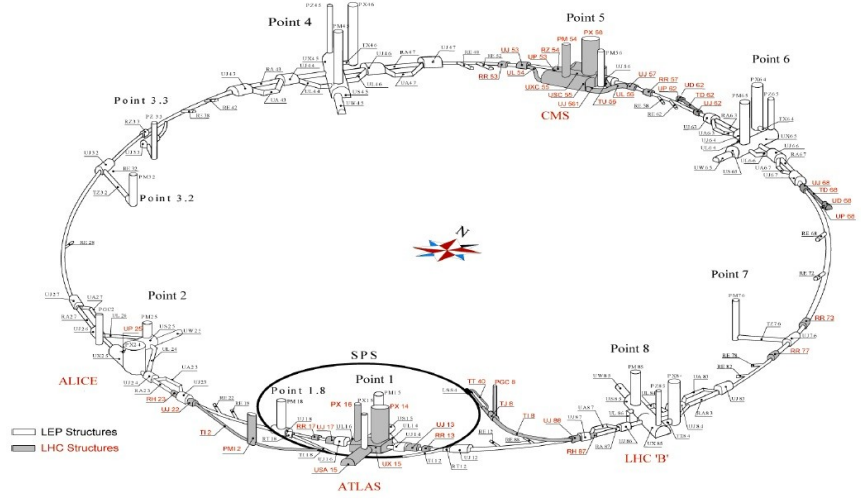


**Figure 3.2.:** The underground structures of both, LHC and LEP, with the four main LHC experiments ATLAS, ALICE, CMS and LHCb and collision points 1, 2, 5 and 8 [26]

at point 2 is a detector dedicated to measure heavy ion collisions. With a peak luminosity of  $L = 10^{27} \text{ cm}^{-2} \text{ s}^{-1}$  it is constructed to target QCD measurements at very high matter densities.

The LHC started operating in 2009. The first proton - proton collisions at a center of mass energy of  $\sqrt{s} = 7 \text{ TeV}$  were proceeded on the 30<sup>th</sup> of March in 2010. By the end of the running period in 2011, data with an overall integrated luminosity of  $L_{\text{int}} = 5.25 \text{ fb}^{-1}$  were taken by the ATLAS detector. Starting in April 2012, collisions at a center of mass energy of  $\sqrt{s} = 8 \text{ TeV}$  have been taken place at the LHC [28] [29].

## 3.2. The ATLAS Detector

As shown in Figure 3.2, the ATLAS detector is located at interaction point 1. Like the CMS detector, it is a general purpose detector, constructed to study particle physics in the TeV energy range. With dimensions of  $25 \text{ m} \times 44 \text{ m}$  it is one of the biggest experiments at the LHC. Nonetheless it only weighs around 7000 tonnes, thus it is considerably light for its size in comparison to the other LHC detectors [23]. The several detector systems

of ATLAS are structured concentrically around the beam line (see Figure 3.3). The inner-most detector component is the Inner Detector (ID), followed by the electromagnetic and hadronic calorimeters and the muon spectrometer [30]. The following sections will review the coordinate system used to describe the ATLAS detector, as well as the single detector components and the ATLAS trigger system.

### 3.2.1. The ATLAS Coordinate System

The ATLAS coordinate system is based on a right-handed Cartesian system, with the origin being the collision point in the beam line. whilst the x-y-plane is situated perpendicular to the beam line, the z-axis is parallel to the beam line. The x-y-plane is usually described by the azimuthal angle  $\Phi$ , whereas the polar angle  $\Theta$  is measured from the z-axis. With the help of the polar angle  $\Theta$ , a new variable can be defined, the pseudorapidity  $\eta$  [23]

$$\eta = -\ln \left( \tan \left( \frac{\Theta}{2} \right) \right). \quad (3.4)$$

Using the pseudorapidity  $\eta$  over  $\Theta$  has the advantage, that the transformation of  $\eta$  from one reference frame to another by using the Lorentz transformation along the beam axis is simply additive. This results from  $\eta$  being the high energy approximation of the rapidity  $y$  (see Equation 3.5) [31] [32].

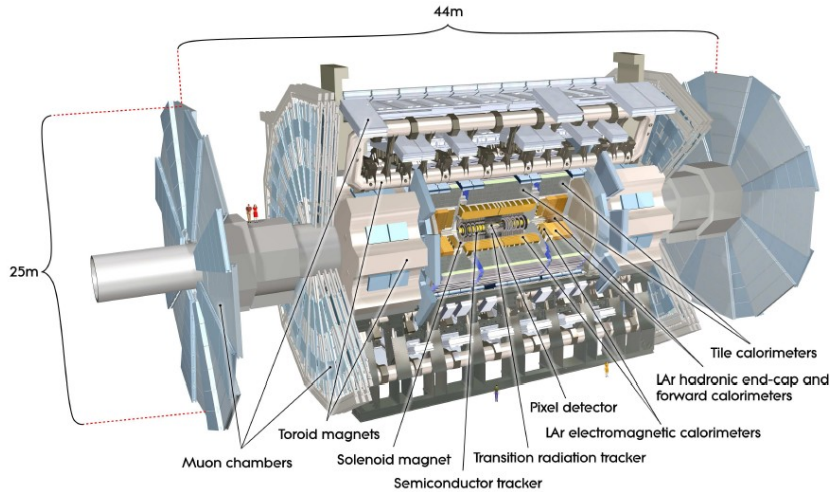


**Figure 3.3.:** A view from the ATLAS detector with all main detector components [23].

$$y = \frac{1}{2} \ln \left( \frac{p_0 + p_z}{p_0 - p_z} \right). \quad (3.5)$$

A different important variable is the distance  $\Delta R$  in angular phase space. It is defined by using the variables  $\eta$  and  $\Phi$

$$\Delta R = \sqrt{\Delta\eta^2 + \Delta\Phi^2}. \quad (3.6)$$

Variables with the subscript "T" refer to the transverse plane. Subsequently, the transverse momentum  $p_T$  for example is defined in the x-y-plane [23].

### 3.2.2. The Magnet System

The magnet system in the ATLAS detector is built for charge-determination of the passing particles. Additionally, it is used for  $p_T$ -measurement purposes by using the effects of the Lorentz force applied to the particles in the magnetic field [13]. It consists of four superconducting magnets: one solenoid, one barrel toroid and two end-cap toroids. Overall the system extends over a volume of 12,000 m<sup>3</sup>.

The solenoid is the inner part of the magnet system. It delivers a magnetic field for the inner detector of a strength of 2 T, which is oriented in the axial direction. Having a weight of 5.4 tonnes and an outer diameter of 2.56 m, the solenoid is the lightest and smallest part of the magnet system. It only exceeds the end-cap toroids in length by 0.8 m, having a total axial size of 5.8 m.

Being the second part of the magnet system, the barrel toroid provides a magnetic field for the muon spectrometer. The barrel toroid stretches over 25.3 m with an outer diameter of 20.1 m. With a sum of eight coils it yields a magnetic field of 0.5 T for the barrel region of the muon system. Its coils are supported by rings of struts, giving it a total weight of 830 tonnes.

The end-cap toroids deliver a field of 1 T strength to increase the track-bending power in the end-caps of the muon spectrometer. On each side of the ATLAS detector, one of the end-cap toroids is located, built with eight coils. Both toroids weigh 240 tonnes and have an outside diameter of 10.7 m [23]. Figure 3.4 depicts the magnet windings of the toroid.

### 3.2.3. The Inner Detector

The Inner Detector (ID) is the first detector the particles cross after being created in the collision. It uses the Lorentz force in the magnetic field of the solenoid (compare to Section 3.2.2) to determine the  $p_T$  and charge of charged particles of which the  $p_T$  exceeds



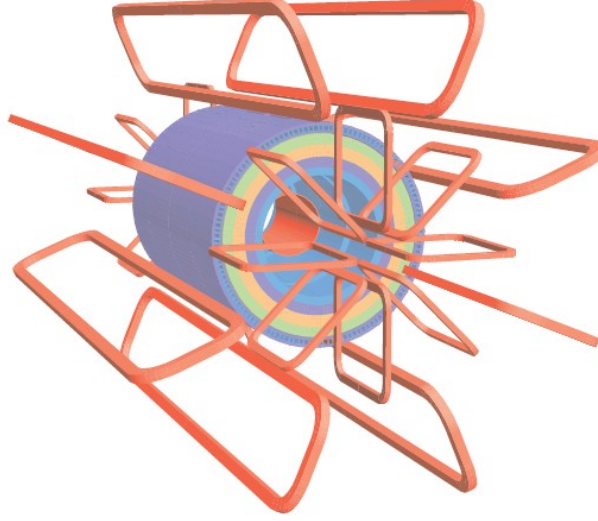


**Figure 3.4.:** A sketch of the magnet windings with the eight barrel toroid coils and the end-cap coils [23].

0.5 GeV [30]. With its three subdetectors, it covers a pseudorapidity of  $|\eta| < 2.5$ . The Pixel Detector, the Semiconductor Tracker (SCT) and the Transition Radiation Tracker (TRT) add up to a diameter of 2.3 m. Altogether they cover a range of 7 m in the axial direction [33]. In Figure 3.5 the ID with all its components is shown.

**The Pixel Detector** The pixel detector is made of 1744 silicon pixel layers in total. Each of them contains 47232 pixels, one pixel being  $50 \mu\text{m} \times 400 \mu\text{m}$  in size. Its main purpose is to identify B-meson decays and thus b-quark content in jets. The pixel detector is divided into three barrel layers and in each case three disc layers in the end-caps [23] [34].

**The Semiconductor Tracker** Like the pixel detector, the SCT is using semiconductor technology to precisely detect particle tracks in the detector. The semiconductor sensors consist of p-in-n silicon microstrips. In the barrel region, the SCT is built out of four layers, with overall 8448 p-in-n strips. The end-caps contain 6944 p-in-n sensors spread out over nine layers on each side [33].

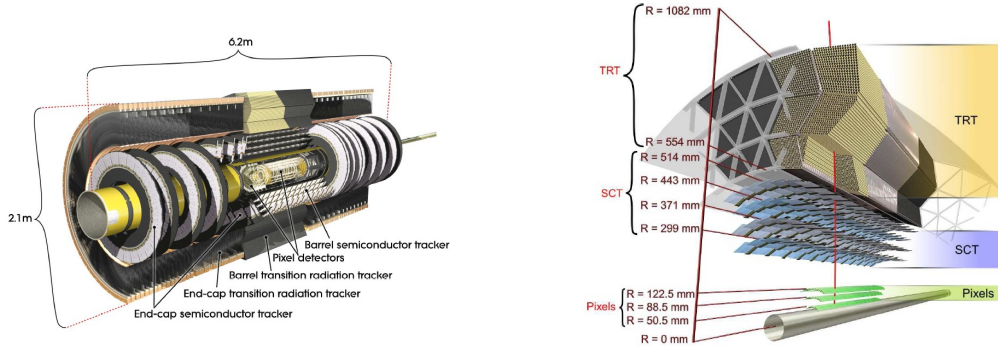


**Figure 3.5.:** A cut-away from the Inner Detector (left) and a view of the barrel section of the Inner Detector (right) [23].

**The Transition Radiation Tracker** The main components of the TRT are gaseous straw-tubes, interrupted by transition radiation material. These strawtubes are essentially proportional drift tubes. The TRT's barrel part is made with 52544 straws, in each end-cap 122880 straws are built-in. Passing particles cross about 35 to 40 of those straws. The cathode part in the straws consists of a thin aluminium layer, whilst the anode wire is made of gold-plated tungsten. The gas mixture used in the drift tubes is 70 % Xe, 27 % CO<sub>2</sub>, 3 % O<sub>2</sub> [35].

### 3.2.4. The Calorimeter System

The ATLAS calorimeter system is set up to measure the energies of passing particles. In order to do that, the particle and the resulting shower (see below) has to be fully absorbed. Hence, the electromagnetic calorimeter has to cover between 15 and 25 so called radiation lengths ( $X_0$ ). The radiation length is the distance, after which the energy of a particle is reduced by the factor  $e$ . For the hadronic calorimeter, the equivalent to the radiation length is called the hadronic interaction length  $\lambda$  [13].

The calorimeters are constructed with a barrel region and one end-cap at each side of the detector. The barrel region is divided into an electromagnetic and a hadronic calorimeter, whilst the end-caps include three parts: The forward calorimeter (FCal), the hadronic end-cap calorimeter (HEC) and the electromagnetic end-cap calorimeter (EMEC). The active material in the electromagnetic barrel, EMEC, HEC and FCal is liquid argon (LAr). The hadronic tile calorimeter is a scintillator sampling calorimeter [23]. Figure 3.6 shows the calorimeter system with all its components.

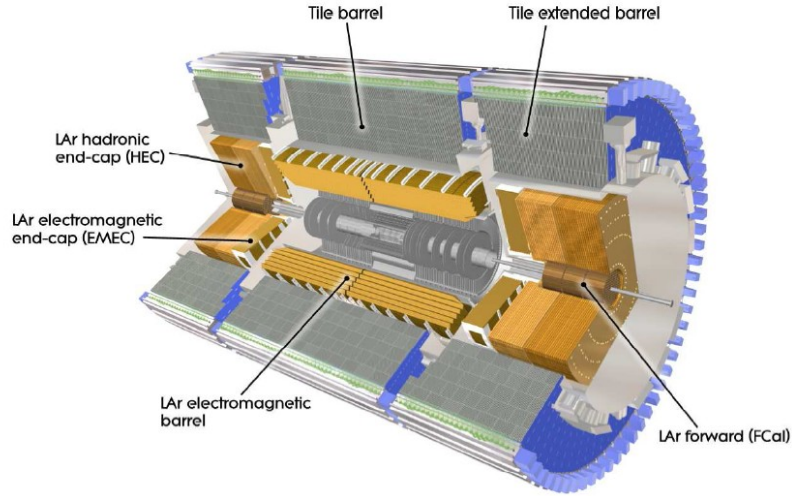


**Figure 3.6.:** The ATLAS calorimeter system [23].

**The Electromagnetic Calorimeter** The electromagnetic calorimeter as the innermost part of the system, was built to measure energies of electrons, positrons and photons. To determine the energies, particle showers are enforced through bremsstrahlungs and pair production effects. This cascade of secondary particles produces a measurable signal in the detector [13]. The absorber material used in the ATLAS electromagnetic calorimeter are lead plates. These are designed in an accordion-shaped style to provide full  $\Phi$  coverage.

In the barrel region, the calorimeter is split in two half barrels. Each of them is 3.2 m long, with an outer diameter of 4 m, and weighs 57 tonnes. They include 2048 absorbers spread over 32 modules with a thickness of  $22X_0$ . Both of the end-cap wheels, the EMEC calorimeters, are 63 cm wide and weigh 27 tonnes. Having 16 modules overall, they cover the pseudorapidity region of  $1.375 < |\eta| < 3.2$  [23].

**The Hadronic Calorimeter** In the hadronic calorimeter, showers of secondary particles are induced from hadrons. These showers are produced in the absorber material through inelastic scattering. In comparison to the electromagnetic shower, they penetrate deeper into the detector material. Additionally, the shower particles have an electromagnetic and a hadronic component [13].

In ATLAS, the absorber medium used in the hadronic tile calorimeter is steel. Scintillator tiles are built-in as sampling medium. As depicted in Figure 3.6, the tile calorimeter

is split in one central barrel part (5.8m wide in axial direction), as well as two extended barrels (2.6 m in length). The tile calorimeter can measure particle energies in the pseudorapidity range of  $0 < |\eta| < 1.7$ . This range is extended by the HEC and the FCal to  $|\eta| < 4.9$ .

The HEC uses copper as absorber material and is located within the end-caps. It is divided into two wheels on each side of the end-caps. The FCal, on the contrary, consists of one electromagnetic detector (FCal1) and two hadronic detectors (FCal2 and FCal3). In the latter two, the absorber medium was chosen to be tungsten, whilst in the electromagnetic module copper provides the absorber substance. Behind the FCal3 a shield made of a copper alloy was installed to stop non-muonic particles from reaching the muon spectrometer [23].

### 3.2.5. The Muon Spectrometer

The muon spectrometer, the outermost part of the ATLAS detector, is designed to determine the transverse momentum,  $p_T$ , of particles escaping the calorimeters. It is located within the toroidal magnet system described in Section 3.2.2. Hence, it is penetrated by a magnetic field of up to 1 T in order to bend the particle tracks for  $p_T$  determination. The muon chambers span over a range of  $|\eta| < 2.7$ . Within a slightly smaller range,  $|\eta| < 2.4$ , they can also trigger on particles [23].

The eight octants of the muon system are constructed with overlapping layers of muon chambers to avoid detector gaps (see Figure 3.7) [23]. In the barrel region the muon system forms three concentric layers, the Barrel Inner (BI), the Barrel Middle (BM) and the Barrel Outer (BO). The end-caps are structured as wheels with four discs on each

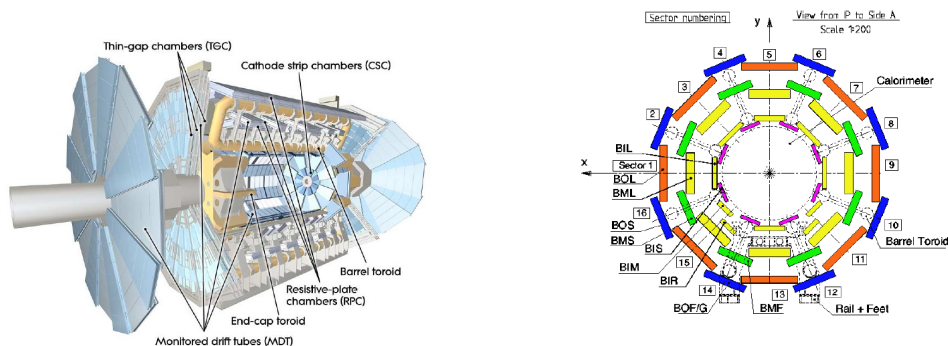


**Figure 3.7.:** A view of the ATLAS muon spectrometer (left) and the barrel part of the muon spectrometer perpendicular to the beam axis [23].

side. Additionally, a collection of sub-detectors are placed in the end-cap system, which is structured similar to the barrel system [36]. In Figure 3.7, a sketch of the muon system is shown.

To measure the  $p_T$  of passing particles, Monitored Drift Tube Chambers (MDT's) are used in the barrel and end-cap region. The exception is the inner detector layer for  $2 < |\eta| < 2.7$  [37]. In the forward  $\eta$ -range, large particles fluxes and a high track density occur after the collision [23]. Thus, proportional multi-wire chambers called Cathode Strip Chambers (CSC) were installed for their capability of measuring higher rates of particles [37].

For triggering on particles, the detector signals have to be provided within nanoseconds. Therefore, fast Resistive Plate Chambers (RPC) are mounted in the barrel region. In the end-caps, proportional multi-wire chambers, Thin Gap Chambers (TGC), are used for triggering [23].

### 3.2.6. The Forward Detectors

Next to the three major detectors described in the previous sections, an additional detector system was constructed for ATLAS. Those three detectors are located very close to the beam line in the forward direction. Placed from the center with increasing  $|z|$ , these detectors are called LUCID (LUMinosity measurement using Čerenkov Integrating Detector), Zero-Degree Calorimeter (ZDC) and ALFA (Absolute Luminosity For ATLAS).

LUCID is a čerenkov detector installed to measure the relative luminosity. For inelastic proton-proton scattering, it determines the integrated luminosity, as well as it observes the immediate luminosity. The ZDC mainly detects neutrons from heavy-ion collisions in  $|\eta| > 8.3$ . The amount of neutrons measured gives information about the centrality of these collisions. ALFA is an absolute luminosity detector, which is made of scintillating fibre trackers. Using elastic scattering, the absolute luminosity is measured at small angles [23].

### 3.2.7. The Trigger System

The purpose of the trigger system is to cut the incoming data rate from 40 MHz to approximately 200 Hz, the maximum storage capability. Thus, it is mainly selecting events with photons, leptons and jets with significant  $p_T$  or large missing transverse energy. Being divided into three parts, the trigger system starts with the Level-1 trigger (L1), followed by the Level-2 (L2) and the event filter. The High-Level-Trigger (HLT) is a combination of the L2 and the event filter. Figure 3.8 shows a diagram of the ATLAS trigger system

[38].

The L1 trigger as the first component of the system, is a hardware trigger [38]. It triggers on leptons, photons and jets with a substantial  $p_T$ . In case of muons it uses a combination of RPC and TGC signals (compare to Section 3.2.5). Its output is an event rate of about 75 kHz after  $2.5 \mu s$ . The objects, which were accepted by the L1, are passed on to the L2. Within 40 ms the L2 filters the event rate to approximately 3.5 kHz. For that intent, the L2 uses information on energies and coordinates of particles as well as the type of particle signatures. The event filter then reduces the event rate even further, to about 200 Hz, so that the data can be recorded [23]. Both, the L2 and the event filter, are trigger based on software algorithms [38]. They use all detector components for the event selection. Especially the track signatures in the Inner Detector and muon spectrometer are crucial to identify passing particles. The calorimeter information on the other side is used to provide energy threshold cuts [23].

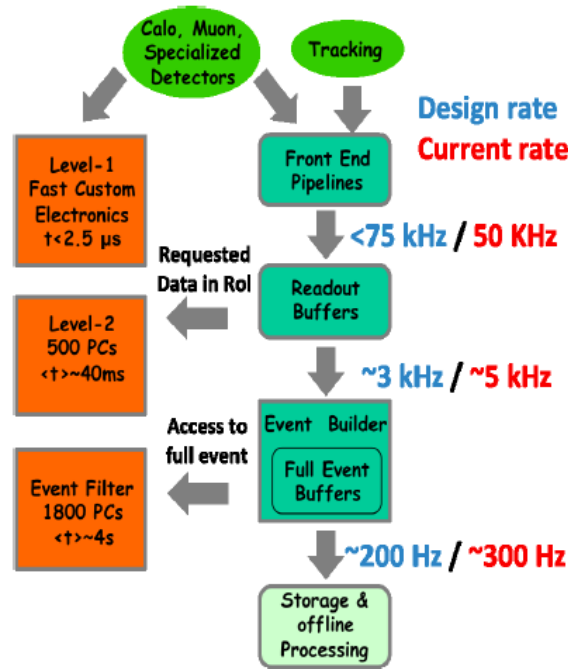


**Figure 3.8.:** A sketch of the ATLAS trigger system with current data rates and design data rates [38].

# 4. Event Selection and Background Estimation

## 4.1. Event Topology

Before the selection criteria for the analysis are described, a brief overview of the event topology studied in the analysis is given. Therefore, the MSSM Higgs production process is outlined, followed by an explanation of the  $\tau$  lepton properties and the background processes, which are considered in this analysis.

### 4.1.1. The Higgs Boson Production

The two major production channels for the MSSM Higgs boson in proton-proton collisions are gluon fusion and b-associated production. Which of the two processes is the dominant one, depends on the proposed Higgs mass and the suggested value of  $\tan\beta$  [39]. Other production processes such as vector boson fusion ( $WW/ZZ$ ) have a negligible influence for the SUSY Higgs boson production [40].

The gluon fusion process

$$gg \rightarrow A/H/h$$

is the main production channel for light Higgs bosons in the low  $\tan\beta$  regions [39]. The fusion process progresses via heavy quark loops, but squark loops are also possible, as shown in Figure 4.1 [41]. The cross-sections of these processes were calculated using HIGLU [42] and ggh@nnlo [43].

In large  $\tan\beta$  regions, the b-associated production of Higgs bosons dominates for which examples are shown in Figure 4.2. The analysis is an inclusive analysis, so no tag on the additionally to the Higgs bosons produced one or two b-quarks was applied [41]. For evaluation of the cross-sections, the Santander matching for 4- and 5-flavor schemes was used [44].

The key decay channels for the MSSM neutral Higgs bosons are  $b\bar{b}$  quark decay ( $\sim 90\%$ ) and  $\tau^+\tau^-$  lepton decays ( $\sim 10\%$ ). Cascade decays involving SUSY particles can occur as

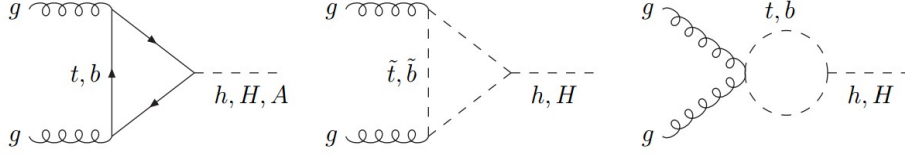


**Figure 4.1.:** Feynman diagrams of gluon fusion Higgs boson production processes, mediated by a heavy quark loop and and squark loops [45].

well [40]. Here, the  $\tau^+\tau^-$  final state is analysed, since  $A/H/h \rightarrow b\bar{b}$  decays are difficult to detect in the hadronic enviroment of the LHC collisions.

#### 4.1.2. The Tau Lepton

The tau lepton is with a mass of 1.777 GeV [4] the heaviest particle in the lepton family. Due to its mass its lifetime is very short ( $3 \cdot 10^{-13}$  [4]) and its potential decay modes involve all other leptons and the lightest quarks in association with neutrinos, e.g. in the case of a  $\tau^-$  [13]:

$$\begin{aligned}\tau^- &\rightarrow e^- + \bar{\nu}_e + \nu_\tau \\ \tau^- &\rightarrow \mu^- + \bar{\nu}_\mu + \nu_\tau \\ \tau^- &\rightarrow d' + \bar{u} + \nu_\tau\end{aligned}\tag{4.1}$$

The decay process, which is mediated by a  $W$  boson exchange, is depicted in Figure 4.3.

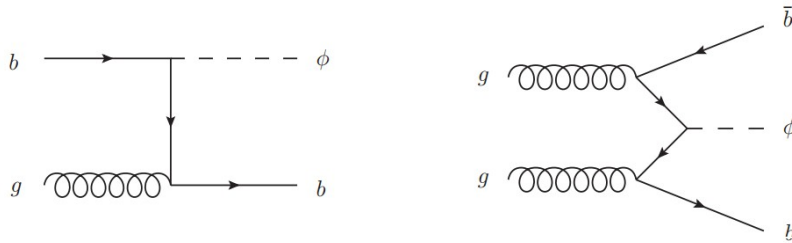


**Figure 4.2.:** Feynman diagrams of b-associated Higgs boson production [46].



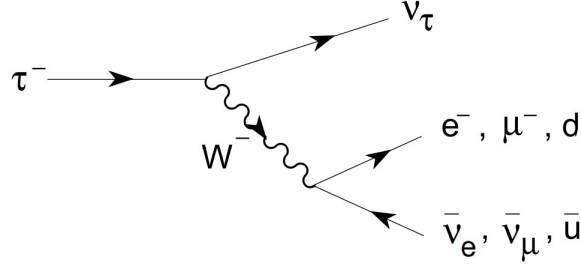


**Figure 4.3.:** A Feynman Diagram of the  $\tau$ -decay with all possible decay channels [8].

In 65 % of the cases, the  $\tau$  decays hadronically [4], the main decay products being charged and neutral mesons, namely pions and kaons. These tau candidates leave a narrow jet signature in the detector, with mostly 1 or 3 charged tracks [47]. The electron and muon decay channels both have a branching ratio of  $\sim 17\%$  [4].

The consequences for the  $A/H/h \rightarrow \tau\tau$  channel are three different possible decay modes:

- leptonic:  $\tau\tau \rightarrow ll + 2\nu_l + 2\nu_\tau$
- semileptonic:  $\tau\tau \rightarrow l + \text{hadrons} + \nu_l + 2\nu_\tau$
- hadronic:  $\tau\tau \rightarrow \text{hadrons} + 2\nu_\tau$

This analysis concentrates on the muon channel of the semileptonic decay mode.

### 4.1.3. Background Processes

To optimise the event selection, possible background processes have to be understood. The following list states the background modes, which were studied in this analysis.

**$\gamma^*/Z$ +jets** The  $\tau\tau$  decay channel of the  $Z$  boson and the Drell-Yan process  $q\bar{q} \rightarrow \gamma^* \rightarrow \tau\tau$  provide the largest background to the  $A/H/h \rightarrow \tau\tau$  decay. Because of the similar decay signature to the signal process, it is an irreducible background, especially for small Higgs masses, where the visible mass  $m_{vis}$  spectra overlap. The visible mass is defined as:

$$m_{vis}^2 = (p_\mu + p_{vis})^2, \quad (4.2)$$

with the four vectors  $p_\mu$  and  $p_{vis}$ . The four vector  $p_\mu$  corresponds to the reconstructed muon, whilst  $p_{vis}$  is the sum of four-vectors of the measured hadronic tau decay products.

In the  $\gamma^*/Z \rightarrow \mu\mu$  decays, the additional jet or one of the muons may be misidentified as a hadronic tau [39].

**$W$ +jets (leptonic decays)**  $W$ +jets decays have a very large cross-section (compare to Table A.1). The accompanying jet can be misidentified as a hadronic tau. Due to the lepton and the neutrino in the decay signature, this process delivers a large background to the signal process [39].

**QCD jets** One of the QCD jets may be misidentified as a hadronic tau candidate and a second jet can be misidentified as a muon. With its large production rate at the hadron collider, it provides significant background for  $A/H/h \rightarrow \tau\tau$  [39].

**$t\bar{t}$  and single- $t$**  The top quark decays practically exclusively [48] to

$$t \rightarrow Wb,$$

with subsequent decay of the  $W$  boson with missing transverse energy and one lepton in the final state. The b-jet with its displaced B-decay vertex is then misidentified as a hadronic tau and thus also contributes to the total background [39].

## 4.2. Event Selection

In order to separate the signal from the background distribution, selection criteria are applied. The section starts with an explanation of the Monte Carlo and data samples used in this analysis. In the then following section, the reconstruction of the measured objects is explained as well as the criteria applied to ensure the quality of the objects. Finally, the selection cuts employed to suppress the background distributions are outlined.

### 4.2.1. Data Samples and Monte Carlo Simulation

In the analysis, the data taking periods B-M10 of the ATLAS 2011 proton run at  $\sqrt{s} = 7$  TeV were used. Thus, the integrated luminosity is

$$L_{\text{int}} = 4.7 \text{ fb}^{-1}.$$

The signal samples were simulated using SHERPA[49] (b-associated Higgs production) and POWHEG+PYTHIA[50] (gluon fusion) for different mass points of the  $\mathcal{CP}$ -odd Higgs

boson  $A$ , with  $\tan\beta = 20$ . The masses of the  $H$  and  $h$  were calculated within the  $m_h^{\max}$  benchmark scenario [51]. In order to obtain samples for  $H/h$ , the samples for  $A$  with nearest mass to  $m_H$  and  $m_h$  were scaled to the appropriate cross-section. To attain a sample for the  $A/H/h$  decay process, all these samples were combined [52]. The masses for  $H$  and  $h$  in the  $m_h^{\max}$  benchmark scenario, depending on  $m_A$  for  $\tan\beta = 20$  are given in Table A.3. A list of the combined cross-sections for different  $m_A$  mass points and  $\tan\beta = 20$  is provided in Table A.2. The optimisation of the event selection was carried out for  $m_A = 120 \text{ GeV}$  and  $\tan\beta = 20$ . The background samples were generated with ALPGEN[53] ( $W$ +jets,  $\gamma^*/Z$ +jets), MC@NLO[54] and ACERMC[55] ( $t\bar{t}$  and single- $t$ ) as listed in Table A.1. The combined cross-sections are also stated in this Table.

To match the real background and a potential signal contribution in the data, the Monte Carlo samples have to be rescaled to the integrated luminosity according to

$$w = \frac{L_{\text{int}} \cdot \sigma \cdot \epsilon}{N}, \quad (4.3)$$

where  $\sigma$  is the production cross-section,  $\epsilon$  is the filter efficiency of the sample and  $N$  is the number of events in the sample. The Monte Carlo filter efficiency takes preselection cuts on generator level into account.

## 4.2.2. Preselection

An object preselection is applied to both, data and Monte Carlo samples, respectively. The selection is described in this section, starting by an explanation of the reconstructed objects. Electrons are not regarded in the event selection, since the analysis concentrates on the  $A/H/h \rightarrow \tau^+\tau^- \rightarrow \mu + \tau_{\text{had}} + \nu_\mu + 2\nu_\tau$  channel only. This is followed by a portrayal of all other preselection requirements employed.

### 4.2.2.1. Object Reconstruction

A brief description of the criteria, the reconstructed objects have to meet is given. The selection criteria of this section and the next section are also summarised in Table A.4.

**Muons** To reconstruct the muon candidates, the "staco" muon reconstruction algorithm is used. This algorithm uses straight track segments in the muon spectrometer, which point towards the center of the ATLAS detector. When more than two such track segments are found in different spectrometer parts, three-dimensional tracking is used to build the muon track [56]. In order to lower the rate of misidentification, the reconstructed muons

have to pass further selection criteria. The reconstructed objects have to have a  $p_T > 10 \text{ GeV}$  and they have to be found within an  $|\eta|$  region less than 2.5. Furthermore, only events with one muon candidate are selected, to reject the  $\gamma^*/Z \rightarrow \mu\mu$  background [57].

**Taus** The hadronically decaying taus are reconstructed by looking for narrow jets with 1 or 3 charged pions (therefore 1 or 3 charged tracks) and a transverse energy contribution from neutral hadrons. To reject jets from QCD events, a Boosted Decision Tree (BDT) algorithm at the medium working point with a  $\tau$  identification efficiency of about 45% is applied. This BDT uses calorimeter and tracking variables for the discrimination between QCD events and real hadronic tau decays [57] [58]. Other requirements for the tau candidates are  $p_T > 20 \text{ GeV}$  and  $|\eta| < 2.5$  as well as a total charge of  $|Q| = 1$ .

**Jets** To reconstruct jets, the anti- $k_T$  algorithm is used. Essentially, the algorithm builds a three-dimensional shower pattern by using calorimeter information [59]. The transverse momentum of the jets must be  $p_T > 20 \text{ GeV}$  and they have to be found within  $|\eta| < 4.5$ .

**Missing Transverse Energy** The missing transverse energy is reconstructed by using energy found in the calorimeter cells as well as contributions from muons [57] [60].

#### 4.2.2.2. Other Preselection Criteria

The following preselection criteria are applied to ensure the quality of the reconstructed objects. Also, the Monte Carlo samples are adapted to match the properties of the data, by reweighting procedures.

**Trigger Selection** The trigger used selects on muons with  $p_T > 18 \text{ GeV}$ . Due to the increasing instantaneous luminosities during the data run in 2011, the required muon identification quality was increased<sup>3</sup> [57]. Thus, for later run periods, the muons have to be of medium quality. The change in the applied trigger was also implemented for the Monte Carlo samples.

**Readout Problem in the Liquid Argon Calorimeter** For some of the data taking periods in 2011, a small part of the electromagnetic calorimeter was essentially inoperative. This was due to readout problems of the optical electronics of the LAr calorimeter after a power cut. Therefore, the potential to reconstruct fake missing transverse energy as result of the readout problem had to be reduced. Hence, events with jets and taus found in the

---

<sup>3</sup>The aim was to use only unscaled triggers.

affected region during this time period were rejected. This treatment has been applied to the data as well as the Monte Carlo samples. The specific regions can be found in Table A.5.

**Pile-up Correction** Pile-up is the overlap of simultaneous proton-proton collisions in the same bunch crossing. In 2011, the separation between the bunches was 50 ns. The Monte Carlo samples are generated with some pile-up conditions applied, but these do not completely meet the data pile-up conditions. This is simply, because the Monte Carlo samples are generated before the data runs. Thus, the reweight conditions were estimated by using the average amount of pile-up events in each data run. These reweight factors are then used, to simulate the same pile-up conditions in the Monte Carlo as occurred in the data [52].

**Correction on the Gluon Fusion induced Higgs samples** Next-to-next-to-leading order (NNLO) calculations provide still some uncertainties for the gluon fusion Higgs production process. The spectrum of the transverse momentum of the Higgs boson is therefore evaluated by the numerical code **HqT**. The accuracy<sup>4</sup> of the NLL+LO(NNLL+NLO) calculations provided by the **HqT** leads to a better description of the differential cross-sections at NLO(NNLO) level. To match the  $p_T$  distribution of the POWHEG gluon fusion samples with the results of the **HqT**, an additional reweighting is applied to the gluon fusion samples [61] [62].

**Jet Cleaning** The jet cleaning is applied on data, to reject jets from other sources than proton-proton collisions. These other sources, such as cosmic rays, hardware problems and beam conditions, can provide a fake jet signal or it can affect the quality of the identified jets [63].

**Overlap Removal and Vertex Reconstruction** When a geometrical overlap between the reconstructed objects described above within a cone of  $\Delta R < 0.2$  is found, one of the objects is removed. If a muon is detected and overlapping with an electron, a tau or a jet, the latter objects are removed. This is repeated similarly for electrons, taus and jets in the given order. Vertices of the events are also reconstructed and they are required to have at least 4 associated tracks. A primary vertex is identified by having associated tracks with the greatest  $\sum p_T^2$  of all reconstructed vertices [57].

---

<sup>4</sup>NLL = next-to-leading-logarithmic accuracy, LO = leading order, NNLL = next-to-next-to-leading logarithmic accuracy, NLO = next-to-leading order

### 4.2.3. Analysis Level Cuts

The final part of the event selection is the analysis selection. Here, cuts are applied to reduce the background distributions and to select signal specific events with regards to the event topology. A summary of these cuts can be found in Table A.6.

**Muon Selection** The cuts on the muons are tightened in this part of the selection. The  $p_T$  is required to be greater than 20 GeV. Since the muons in the final states of the  $A/H/h \rightarrow \tau\tau$  decay are isolated, some isolation criteria are applied to the muons. This means, that in a certain distance around the muon track, no significant transverse energy or transverse momentum entry should be found (for more details see Table A.6). Additionally, the muons are required to be measured in both, the muon chambers and the Inner Detector. The  $p_T$  is then reconstructed from the combined  $p_T$  measurement [56].

**Charge Correlation** The MSSM Higgs bosons  $A/H/h$  have no electric charge. Thus, the decay products have to have opposite charge, which is applied by requiring the charge product between muon and hadronic tau to be  $-1$ . Furthermore, all events with more than one hadronic tau are rejected, since the observed decay channel is semileptonic.

**Missing Energy and Transverse Mass** The missing transverse energy is required to be larger than 20 GeV. Applying this cut reduces the QCD background as well as the  $\gamma^*/Z \rightarrow \mu\mu$  backgrounds, where no missing transverse energy occurs. The transverse mass between lepton and missing transverse energy of an event is

$$m_T = \sqrt{2 \cdot E_T^{miss} \cdot E_{T,\mu} \cdot (1 - \cos\Delta\Phi(\mu, E_T^{miss}))}. \quad (4.4)$$

Here,  $E_{T,\mu}$  is the transverse energy of the muon,  $E_T^{miss}$  the missing transverse energy.  $\Delta\Phi$  describes the polar angle between the two objects. In order to suppress backgrounds from  $W$ +jets and  $t\bar{t}$  production, this variable is set to be  $m_T < 30$  GeV [39].

Table 4.1 shows a summary of the event yields for  $L_{\text{int}} = 4.7 \text{ fb}^{-1}$  after all the described selection cuts are applied. All considered background processes are listed, as well as a potential signal for the parameters  $m_A = 120$  GeV and  $\tan\beta = 20$ . The event yields for the  $W$ +jets and the QCD background were obtained by the methods described in Section 4.3.1 and Section 4.3.2.

Process	Number of Events
$\gamma^*/Z \rightarrow \mu^+\mu^-/e^+e^-$	431
$\gamma^*/Z \rightarrow \tau^+\tau^-$	5187
$W \rightarrow l\nu_l$	787
QCD	3231
top ( $t\bar{t}$ and single $t$ events)	172
$A/H/h \rightarrow \tau_\mu\tau_{had}$	399

**Table 4.1.:** Remaining events after all selection criteria have been applied for  $L_{\text{int}} = 4.7 \text{ fb}^{-1}$ , for all background distributions and the signal for  $m_A = 120 \text{ GeV}$  and  $\tan\beta = 20$ . The background estimation methods, with which those backgrounds have been obtained are, described in Section 4.3.

## 4.3. Background Estimation

In order to search for the neutral MSSM Higgs bosons it is important to understand the normalisation and shape of the background distributions. It is beneficial to use data-driven background estimation methods to ensure the right evaluation of the background processes. The top and single-top backgrounds are negligible in the  $\tau_\mu\tau_h$  channel. Therefore their shape and normalisation is taken from the Monte Carlo simulations. All  $Z$ +jet backgrounds are also estimated using Monte Carlo samples. It was verified [64], that the predicted background shapes agree well with  $\gamma^*/Z \rightarrow ll$  data. The other two main backgrounds,  $W$ +jets and QCD events, are estimated as described in this section.

### 4.3.1. $W$ +jets Background

The  $W$ +jets Monte Carlo simulations overestimate the actual amount of the  $W$ +jet background included in the data. In the  $W$ +jet Monte Carlo production, the probabilities for the creation of quark and gluon jets is miscalculated. This overestimation leads to a higher rate of misidentified hadronic taus for the  $W$ +jets background <sup>5</sup> [65].

Thus, the normalisation of the Monte Carlo simulations has to be corrected. In order to correct the Monte Carlo, a  $W$ +jets enriched control region is defined. All selection cuts described in Section 4.2 are carried out as stated, with the exception of two cuts. The key cut for the  $W$ +jets background rejection is inverted and the cut value is set to  $m_T > 70$  GeV. Additionally, a cut on the variable

$$\sum \cos\Delta\Phi = \cos\Delta\Phi(\mu, E_T^{miss}) + \cos\Delta\Phi(\tau, E_T^{miss}) \quad (4.5)$$

is applied. This value is small for the  $W$ +jets background (compare to Figure B.1), hence the cut is set to  $\sum \cos\Delta\Phi < -0.2$ . The  $m_T$  distribution after the  $\sum \cos\Delta\Phi$  cut, but before the  $m_T$  cut is shown in Figure 4.4.

The described discrepancy between the data and the  $W$ +jets background can clearly be seen in this figure. The red line depicts the cut on  $m_T = 70$  GeV, beyond which the normalisation process is carried out. It is assumed, that the  $W$ +jets control region is free of QCD events for  $m_T > 70$  GeV. This is important, since in the QCD estimation the normalised  $W$ +jets samples are used, as will be described in the next section. To obtain the normalisation factor  $k_W$ , all other remaining backgrounds ( $\gamma^*/Z$  and top) are subtracted from the data in each bin of the histogram. The normalisation factor is then

---

<sup>5</sup>The associated jet in the  $W$ +jets background gets misidentified as hadronic tau. The muon candidate originates in the decay of the  $W$  boson [64].



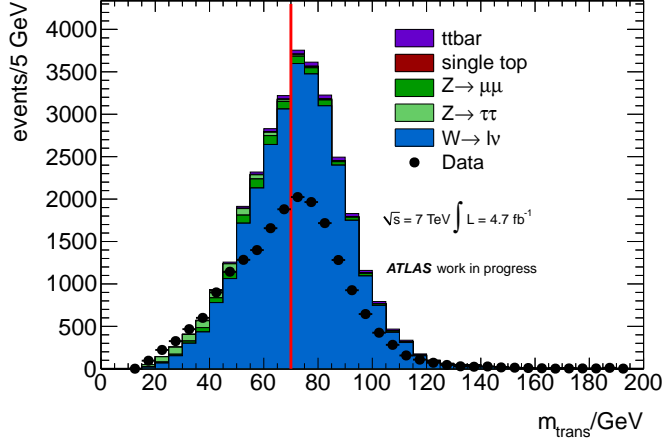


**Figure 4.4.:** The transverse mass,  $m_T$ , in the  $W$ +jets control region before normalisation, after the cut on  $\sum \cos \Delta \Phi$ , but before the cut on  $m_T$ , for  $L_{\text{int}} = 4.7 \text{ fb}^{-1}$ . It is assumed to be QCD and signal free beyond  $m_T > 70 \text{ GeV}$ . The normalisation factor  $k_W$  is obtained after the cut on  $m_T$  which is shown by the red line.

evaluated by

$$k_W = \frac{\int (N^{\text{data}} - N^{\text{Z,top}})}{\int N^W} = 0.51 \quad (4.6)$$

The value for  $k_W$  is found to be in good agreement with the one in [64]. To justify the use of the integrals over the taken data and  $W$ +jets distributions, the  $m_T$  distribution is shown in Figure B.2 with a logarithmic scale for  $m_T > 70 \text{ GeV}$ . The ratio between the data and the  $W$ +jets is almost constant, which is why an extra evaluation of  $k_W$  for each bin is not needed. After applying  $k_W$  to the  $W$ +jets samples, the  $m_T$  distribution is again displayed in Figure 4.5 (with the  $\sum \cos \Delta \Phi$  cut, but no cut on  $m_T$ ). A mismatch between the data and the sum of the Monte Carlo samples can be seen in the lower  $m_T$  region. This is believed to be due to the QCD background, which is not displayed in this plot.

### 4.3.2. QCD Background

At a hadron-hadron collider, the QCD background contribution is considerably large. To provide a background for the  $\tau_\mu \tau_h$  channel, a fake muon emerges from one jet and another jet gets misidentified as a hadronic tau candidate. To estimate the QCD background, a signal region and three QCD enriched control regions are defined. In the signal region, referred to as region A, the event selection as described in Section 4.2 is applied. For the

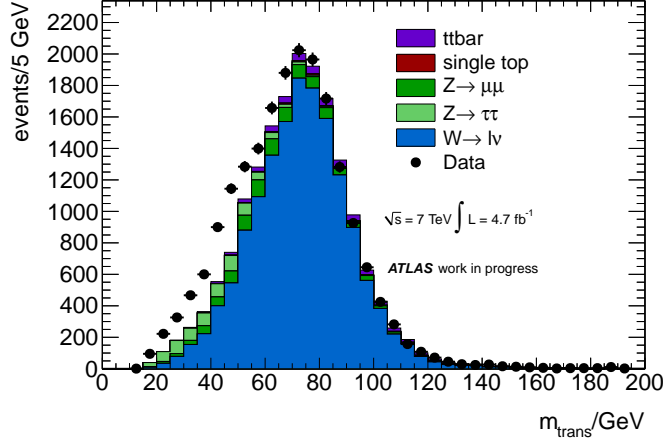


**Figure 4.5.:** The transverse mass  $m_T$  in the  $W$  control region after normalisation, after the cut on  $\sum \cos \Delta \Phi$ , but before the cut on  $m_T$ , for  $L_{\text{int}} = 4.7 \text{ fb}^{-1}$ .

three control regions, the cuts on the muon isolation and the charge product between muon and hadronic tau are inverted. Thus, four different selection criteria are used to evaluate the four regions: opposite sign (OS) or same sign (SS) for the charge of the muon and the hadronic tau candidates, and an isolated muon or a non-isolated muon. Combining these criteria in different ways leads to the four regions. The specific selection criteria are listed in Table B.1 and the event yields in all three control regions for  $L_{\text{int}} = 4.7 \text{ fb}^{-1}$  are summarised in Table 4.2. Figure 4.6 shows a sketch of the four regions, with the selection criteria applied for each region.

It is assumed, that the ratio of the number of QCD events between the OS and SS regions is the same for the isolated muon regions and the non-isolated muon regions respectively. The ratio factor  $r_{\text{OS/SS}}$  is obtained by subtracting the data events in region B and D by the  $W$ +jets,  $Z$ +jets and top background samples (compare to Equation 4.7). For this, a second  $k_W$  factor has to be obtained for the SS region, as the ratio of quark- and gluon-induced jets changes by inverting the charge product cut [64][65]. The new normalisation factor is found to be  $k_W(\text{SS}) = 0.61$ . The ratio factor for OS/SS is:

$$r_{\text{OS/SS}} = \frac{N_B^{\text{data}} - N_B^{\text{MC(EW,top)}}}{N_D^{\text{data}} - N_D^{\text{MC(EW,top)}}} = 1.14, \quad (4.7)$$

which matches the value which was evaluated by [64].

This factor is now applied to the data in region C to attain the shape of the QCD in region A. For this, the electroweak and the top background have to be subtracted from

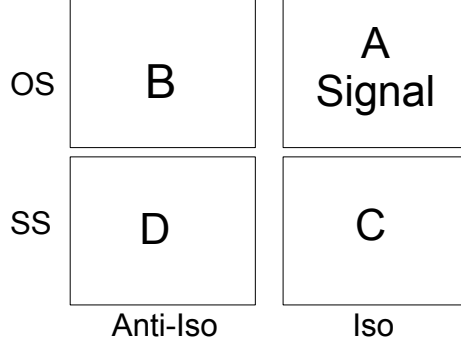


**Figure 4.6.:** The four QCD regions for the background estimation. The selection criteria are opposite sign (OS), meaning the charge product between  $\mu$  and  $\tau_h$  is negative; same sign (SS), meaning the charge cut for  $\mu$  and  $\tau_h$  is positive; isolated muon (Iso), compare to the muon isolation criteria in Table A.6 and non-isolated muon, therefore reversing the isolation cuts in A.6.

the data in region C first. The amount of QCD events in region A is:

$$N_A^{\text{QCD}} = r_{\text{OS/SS}} \cdot \left( N_C^{\text{data}} - N_C^{\text{MC(EW,top)}} \right) = 3231. \quad (4.8)$$

In Figure 4.7 the QCD estimation method is applied to the  $W$ +jets control region (left plot). The data and the sum of the background distributions match very well. Additionally, a plot of the  $m_T$  distribution in the signal region is shown in Figure 4.7, after the cut on the charge product. Background and data distribution also agree well in this plot. Thus, the background estimation is considered to be successful. Distributions of the variables

Process	Region B	Region C	Region D
$\gamma^*/Z \rightarrow \mu^+\mu^-/e^+e^-$	7	162	3
$\gamma^*/Z \rightarrow \tau^+\tau^-$	93	110	8
$W \rightarrow l\nu_l$	22	240	7
top ( $t\bar{t}$ and single $t$ events)	95	31	68
$A/H/h \rightarrow \tau_\mu\tau_{had}$	6	2	0
data	23207	3403	20089

**Table 4.2.:** Event yield for all three QCD control regions after the event selection was applied, for  $L_{\text{int}} = 4.7 \text{ fb}^{-1}$ . The QCD content in each region is obtained by subtracting the simulated background from the data. In all three regions the contributions from the signal ( $m_A = 120 \text{ GeV}$ ,  $\tan\beta = 20$ ) are negligible.

$p_T$ ,  $\eta$  and  $\Phi$  for both, muon and hadronic tau, are shown in Figures B.3 - B.6 for all four QCD estimation regions.

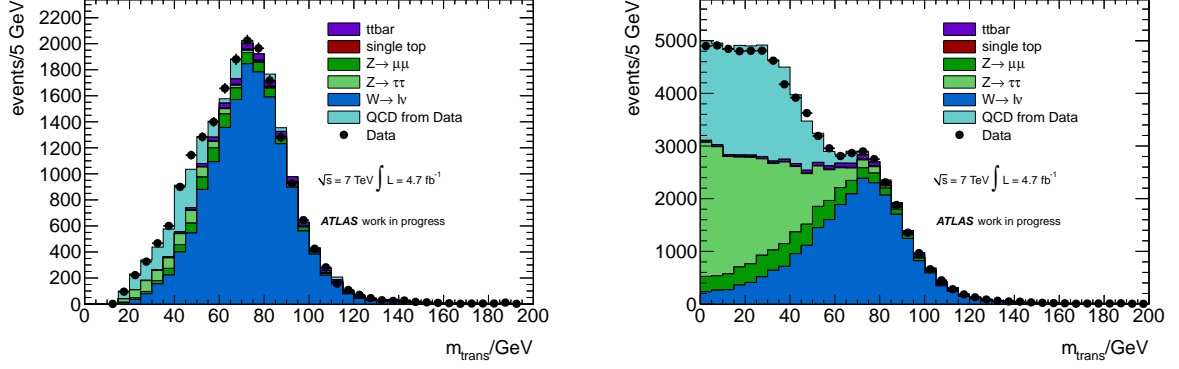


**Figure 4.7.:** The transverse mass  $m_T$  in the  $W$  control region after normalisation, after the cut on  $\sum \cos \Delta \Phi$  (left), but before the cut on  $m_T$ , with QCD background. The  $m_T$  distribution before the  $\sum \cos \Delta \Phi$  cut, but after the cut on the charge product, is shown on the right. Both distributions are for  $L_{\text{int}} = 4.7 \text{ fb}^{-1}$

## 5. TMVA Analysis - Optimisation of the Event Selection

The next step in the analysis is the optimisation of the event selection. This is done by using multivariate methods. The aim is to achieve a high background reduction rate without too much signal efficiency loss. The process of the selection optimisation will be described in this chapter.

The event yields shown in Table 4.1 lead to several conclusions. Initially it can be seen, that a potential Higgs signal is considerably small. In the process of the selection optimisation, the Higgs simulation for  $m_A = 120$  GeV and  $\tan\beta = 20$  is used. In this case, the mass for the other two neutral supersymmetric Higgs bosons are  $m_H = 132$  GeV and  $m_h = 118$  GeV, within the  $m_h^{\max}$  benchmark scenario. These get combined to an  $A/H/h$  sample as described in Section 4.2.1. The resulting cross-section is listed in Table A.2. The  $\gamma^*/Z \rightarrow \tau\tau$  background is the largest background, but will not be considered in the optimisation process, since its signature is too close to the signal signature. Thus it cannot be reduced without losing too much of the signal and it is considered to be an irreducible background.

Hence, this analysis concentrates on the reduction of the QCD and  $W$ +jets backgrounds, which provide the second and third largest backgrounds (Table 4.1). The optimisation was chosen to be carried out separately for the  $W$ +jets and the QCD background. Since the QCD estimation is a data-driven method, only data can be used as a QCD sample (see below). Therefore, the aim must be to find a QCD control region, where the QCD content in the data is as pure as possible. Another important requirement for the chosen region is, that the shape of the distributions for the QCD background in the control region is the same as in the signal region. The only control region used in the background estimation, which provides the QCD background shapes of the signal region is region C [39]. As can be seen in Table 4.2, out of all QCD control regions, region C has the smallest relative QCD content. Thus, the  $W$ +jets background is tried to be reduced first, in order to reduce the main background left in region C and to gain a QCD sample of higher purity.

For the optimisation process, the Toolkit for Multivariate Analysis (TMVA) is used.

TMVA is a ROOT implementation for multivariate classification. For the training of the classifiers, the given background and signal samples are divided into a training and a test sample. The training sample is used to define a mapping function which provides a decision boundary. The test sample is used to validate the results of the classification. TMVA is an event based analysis tool, which means the results of the QCD estimation cannot directly be used as training sample, since the QCD estimation only provides a shape of the QCD content in the signal region. Also, this is the reason, why the content of the electroweak background and the top background cannot simply be subtracted from the data in region C, to get a QCD training sample. [66]. The classification methods investigated in the analysis are briefly described in the next section. This is followed by a description of the  $W$ +jets background reduction process and the QCD background reduction process.

## 5.1. Multivariate Methods

In order to optimise the event selection, multivariate classification methods were trained in TMVA. A list of all available classification methods can be found in [66]. For this analysis, the focus was laid on three of these methods, with a comparison of their performance for both  $W$ +jets and QCD background respectively. In this section, a brief description of all three methods is given.

### 5.1.1. Rectangular Cuts

The rectangular cut classifier is the simplest classifier. It uses cuts on the given discriminating variables, to distinguish between background and signal. Therefore it gives a binary response. All objects which do not meet the cut requirements, are immediately rejected. This way, a given signal efficiency is achieved whilst maximising the background rejection. The signal efficiency,  $\epsilon_{\text{sig}}^{\text{n-prong}}$ , and the background efficiency,  $\epsilon_{\text{bkg}}^{\text{n-prong}}$ , are defined as<sup>6</sup>

$$\begin{aligned}\epsilon_{\text{sig}}^{\text{n-prong}} &= \frac{\text{\# of tau candidates with n reconstructed tracks, passing ID}}{\text{\# of true visible hadronic tau decays with n prongs}} \\ \epsilon_{\text{bkg}}^{\text{n-prong}} &= \frac{\text{\# of tau candidates with n reconstructed tracks, passing ID}}{\text{\# of tau candidates with n reconstructed tracks}}\end{aligned}\tag{5.1}$$

The background rejection is given by  $(1 - \epsilon_{\text{bkg}}^{\text{n-prong}})$  [66] [67].

---

<sup>6</sup>n-prong describes the number of charged tracks which are related to the  $\tau_h$  candidate (1 charged track is a 1-prong candidate, 3 charged tracks is a 3-prong candidate) [39]

### 5.1.2. Projective Likelihood Estimator

The likelihood function is essentially a product of probability density functions (PDF) of the given input variables:

$$\mathcal{L}_{S(B)} = \prod_{k=1}^{n_{var}} p_{S(B),k}(k_k(i)), \quad (5.2)$$

with the signal (background) PDF  $p_{S(B),k}$  of the  $k$ -th identification variable  $x_k$ . To provide optimal separation between signal and background, the likelihood ratio  $y_{\mathcal{L}}(i)$  is used, which is defined by [66] [67]:

$$y_{\mathcal{L}}(i) = \frac{\mathcal{L}_S(i)}{\mathcal{L}_S(i) + \mathcal{L}_B(i)}. \quad (5.3)$$

### 5.1.3. Boosted Decision Trees

A Boosted Decision Tree sets cuts on one input variable at a time. Essentially, the optimal separation for signal and background is determined for each variable. These cuts are used to split the whole training sample into child nodes. Unlike the rectangular cut classifier however, it does not reject the events that did not pass. Instead, it applies the same method again on all child nodes, splitting each in another set of child nodes. The process is continued until a given stop criterion is met. Depending on the majority of the events in each of the final nodes, they are considered as signal or background. In a Boosted Decision Tree (BDT), this is done for several trees, which in the end form one classifier by using a weighted sum of all trees [66][67].

## 5.2. Reduction of $W$ +jets Background

To train the multivariate classifiers for the  $W$ +jets background reduction, the  $W$ +jets Monte Carlo samples (Table A.1) in the signal region were used. Those were normalized as described in Section 4.3.1.

For a good stable training output with no overtraining, samples with high statistics are required. Overtraining is an effect, which occurs when not enough data points, but too many model parameters exist. In this case, the program has not enough degrees of freedom to provide a good performance output. Overtraining can be tested by comparing the classifier outputs of the training and testing samples. If there is a mismatch, the classifier was overtrained [66]. As seen in Table 4.1, the  $W$ +jets samples as well as the signal sample have a very small number of events left, considering that these samples have to be split in a training sample as well as a test sample.

Thus, the event selection was slightly adjusted. The cuts which are especially used for  $W$ +jets background rejection, namely the cut on  $E_T^{miss}$  and  $m_T$ , were not applied. Additionally, the requirement of only one hadronic tau candidate in each event was also not employed. The resultant event yield scaled to  $L_{\text{int}} = 4.7 \text{ fb}^{-1}$  is considered large enough to start the training:

$$N_{\text{MC}}(W \rightarrow l\nu_l) : 24708$$

$$N_{\text{MC}}(A/H/h \rightarrow \tau_\mu\tau_h) : 1176$$

### 5.2.1. Variable Decision

In this section a brief justification of the variables used in the training is given. From a list of variables tested, they are the subset which gave the best performance results. All variables which were considered in the training are listed in Table C.1. This final selection is shown in Figure 5.1 for background and signal respectively. Figure C.1 depicts the linear correlation coefficients for these variables.

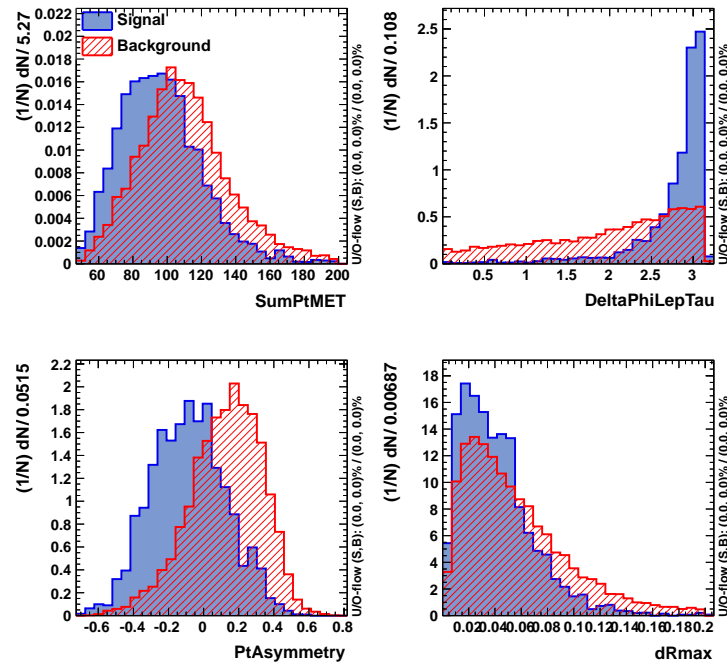


**Figure 5.1.:** Variable selection for the training against the  $W$ +jets background. Blue is the signal distribution, shown in red is the  $W$ +jets background.



**Sum of the  $p_T$  of reconstructed objects** The variable depicted in the upper left corner of Figure 5.1 is obtained via:

$$\text{SumPtMET} = p_{T,\mu} + p_{T,\tau} + E_T^{\text{miss}}. \quad (5.4)$$

It can be seen, that the  $W$ +jets events have overall a slightly higher total energy than is predicted for the signal. Therefore, the background distribution is shifted to the right.

**The angular difference in the transverse plane of the reconstructed objects** In the upper right corner of Figure 5.1 the distributions for the variable

$$\text{DeltaPhiLepTau} = |\Phi_\mu - \Phi_\tau| \quad (5.5)$$

are shown. This variable provides information about the geometry of the decay process. The signal decay signature is mainly a back-to-back decay. Thus, the muon and the hadronic tau candidate leave the interaction point in opposite directions under an angle of  $180^\circ$  to each other. Contrary to that, the  $W$ +jets decays have a less correlated angular dependence.

**The difference in the  $p_T$  of the reconstructed objects** The lower left part of Figure 5.1 shows the  $\text{PtAsymmetry}$  which relates the  $p_T$  of muon and hadronic tau to each other:

$$\text{PtAsymmetry} = \frac{p_{T,\mu} - p_{T,\tau}}{p_{T,\mu} + p_{T,\tau}}, \quad (5.6)$$

Essentially, it describes the difference in the transverse momenta of the objects, normalised to the sum of the momenta. The peak of the signal sample is found at approximately 0, which means that the muon and the hadronic tau generally have the same  $p_T$ . In the  $W$ +jets decays however, the muon candidate has a higher transverse momentum, which can be seen as a right shift of the distribution.

**The Tau ID variable  $\Delta R_{\text{max}}$**  The variable  $\Delta R_{\text{max}}$  (or  $\text{dRmax}$ ) is one of the variables, which is used for the training of the Likelihood ratios and the BDT for the tau identification. When a tau candidate decays hadronically, a narrow jet of hadrons can be seen. This jet has core tracks, which should be close to the axis of the tau candidate, if the origin of the jet really was such a tau lepton.  $\Delta R_{\text{max}}$  describes the maximal distance between the core tracks and the tau axis. Therefore, the signal distribution has its peak at small values, whilst the  $W$ +jets distribution is a little bit broader, where the jets get misidentified as

hadronic taus.

### 5.2.2. Multivariate Analysis and Performance

Before starting the training of the multivariate methods, it is possible to preprocess the described input variables. The benefits of preprocessing are the reduction of variable correlation, getting more suitable variable shapes for the training or saving response time [66]. In this analysis, two of the preprocessing variable transformations were applied to the Likelihood estimator as well as the BDT classifier.

**Decorrelation** This transformation is especially important for the Likelihood classifier, since the Likelihood ratio ignores any correlation between the discriminating variables. This can lead to performance loss. The same applies to an extent to the BDT. To decorrelate variables, the square root of the covariance matrix is computed. The inverse of this diagonalised matrix is then multiplied to the vector of variables for decorrelation. Decorrelation is computed for signal and background separately. For classifiers, which do not distinguish between signal and background hypotheses, the users chooses which transformation is used. The Likelihood classifier uses both transformations, since it does distinguish between signal and background hypotheses [66].

**"Gaussianisation"** The Gaussian transformation of the variables is necessary, because the decorrelation method requires Gaussian distributed input variables. The Gaussianisation is done in two steps. The first step is, to gain a uniform variable distribution. Secondly, this uniform distribution is turned into a Gaussian by using the inverse error function [66].

Additionally to the preprocessing transformations, configuration options can be used to improve the performance of the classifiers. A list of the options used for each classifier can be found in Table C.2. The results of the training are shown in Figure 5.2 for the Likelihood and the BDT classifier. There is no response plot available for the rectangular cut classifier, since it only provides a binary response. It can be seen, that a good separation between background and signal was achieved for both classifiers.

Next to these plots and the plots for the overtraining check in Figure C.2, the separation, the discrimination significance and the so called ROC curve are used to evaluate the performance of the classifiers. The Receiver Operating Characteristic (ROC) curves shown in Figure 5.3 give the background rejection versus the signal efficiency. The aim is to maximise the integral of this curve. Figure 5.3 shows, that the performance of the

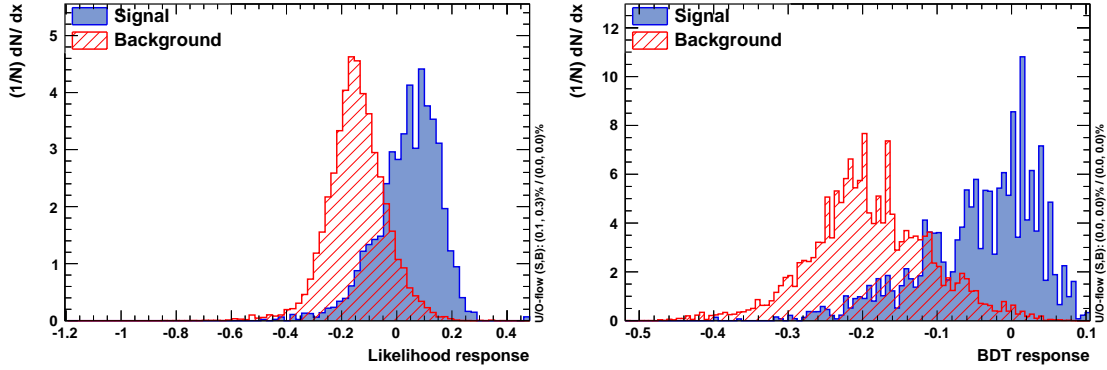


**Figure 5.2.:** Final Likelihood (left) and BDT (right) score for the training against the  $W$ +jets background. As in Figure 5.1, the signal contribution is shown in blue, the  $W$ +jets background contribution is shown in red. These plots are used to validate the cut score on the trained method.

Likelihood and the BDT are very similar. Overall, the rectangular cut classifier does not show such a good performance.

The value of the separation between background and signal is obtained by

$$\langle S^2 \rangle = \frac{1}{2} \int \frac{(\hat{y}_S(y) - \hat{y}_B(y))^2}{\hat{y}_S(y) + \hat{y}_B(y)} dy, \quad (5.7)$$

with  $\hat{y}_S$  and  $\hat{y}_B$  being the signal and background PDFs of the classifiers  $y$ . If the background and the signal are identical,  $\langle S^2 \rangle$  is zero, in the case of no overlap it is one. Therefore, this value is required to be as high as possible. The resultant separation for the Likelihood and the BDT is given in Table 5.1.

Eventually, the discrimination significance of the classifier is considered. To evaluate the discrimination significance, the classifier means for signal and background are subtracted. This is then normalised to the quadratic sum of the root-mean-squares of both. The discrimination significance is also stated in Table 5.1 [66].

	BDT	Likelihood
Significance	1.26	1.01
Separation	0.49	0.48

**Table 5.1.:** Separation and Discrimination Significance for the  $W$ +jets background, for the two investigated multivariate methods, BDT and Likelihood.

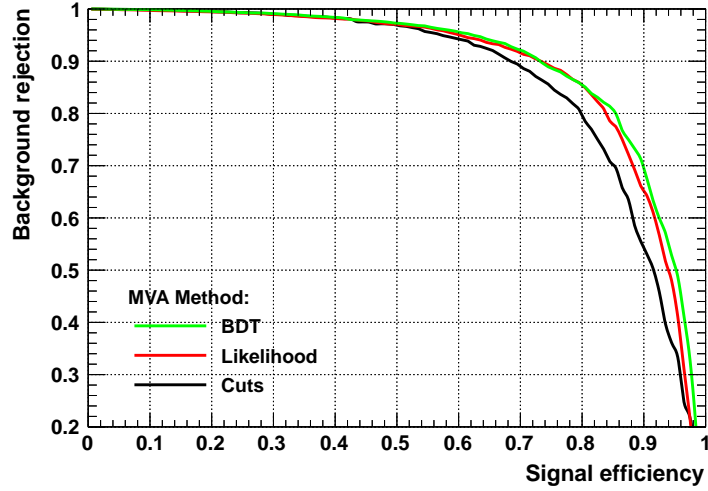


**Figure 5.3.:** The background rejection over the signal efficiency for all three investigated methods.

Since all classifiers seem to provide a good performance, they are implemented in the event selection to compare their results. The cut scores on BDT and Likelihood are obtained from the distributions in Figure 5.2. They are  $-0.11$  for the BDT and  $-0.05$  for the Likelihood, respectively. For the rectangular cut classifier, a signal efficiency of 75 % was set, since at that point the classifier still provides a good background rejection (see Figure 5.3).

### 5.2.3. Results and Conclusion

The resulting event yields of the new event selection are given in Table 5.2. The relative amount, by which the event yields were reduced with respect to Table 4.1 are also stated. The optimisation step was successful, since a reduction of the  $W$ +jets background by about 43 % to 57 % was achieved. A remarkable side effect is, that all top backgrounds are reduced by 73 % - 91 %. This is due to the fact, that the decay products of the standard model top are  $W$  bosons and  $b$  quarks [48]. Hence, training multivariate methods against  $W$ +jets background also reduces the top background.

For the remaining analysis, the BDT classifier was applied (from now on referred to as  $\text{BDT}_W$ ). The rectangular cut classifier reduces the signal by 26 % and has a worse performance in the ROC curve. Comparing the discrimination significance and the separation between BDT and Likelihood, one can see, that the BDT gives a better performance. Additionally, the Likelihood classifier reduces the signal slightly more but does not cut back

as much  $W$ +jets and top background. Thus, with regards to future analyses with more statistics, the BDT classifier was chosen. Figure 5.4 gives a visualisation of the effect of the  $\text{BDT}_W$  by showing the  $m_{\text{vis}}$  distribution with applied  $\text{BDT}_W$  and without applied  $\text{BDT}_W$ .

Process	BDT		Likelihood		Rectangular Cuts	
	# Events	%	# Events	%	# Events	%
$\gamma^*/Z \rightarrow \mu^+\mu^-/e^+e^-$	306	29	295	31.6	268	37.8
$\gamma^*/Z \rightarrow \tau^+\tau^-$	4133	20.3	4157	19.9	3705	28.6
$W \rightarrow l\nu_l$	404	48.7	448	43.1	335	57.4
QCD	2387	26.1	2358	27	2203	31.8
top	34	80.2	47	72.7	16	90.7
$A/H/h \rightarrow \tau_\mu\tau_{had}$	334	16.3	331	17	295	26.1

**Table 5.2.:** Event yields after application of multivariate methods against the  $W$ +jets background, for  $L_{\text{int}} = 4.7 \text{ fb}^{-1}$ . Additionally the relative amount, by which the event yields got reduced in comparison to Table 4.1 is given.

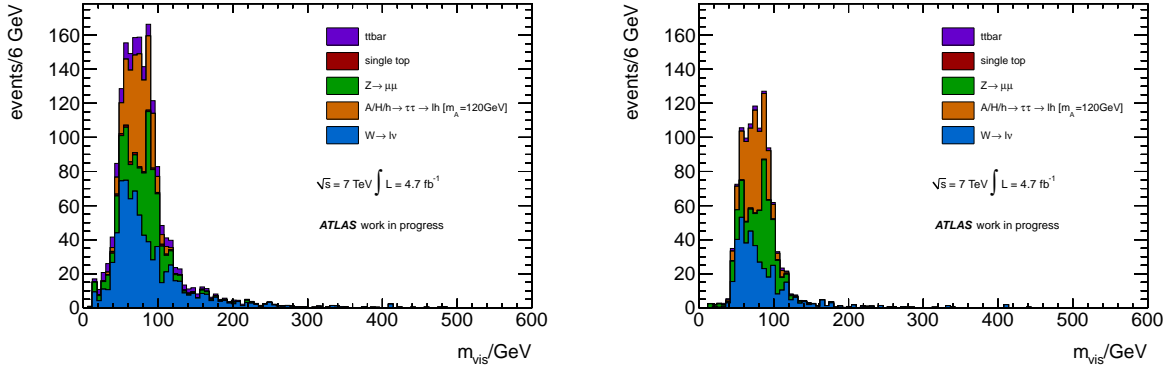


**Figure 5.4.:** The  $m_{\text{vis}}$  distribution before (left) and after (right) the new  $\text{BDT}_W$  was applied, for  $L_{\text{int}} = 4.7 \text{ fb}^{-1}$ . The  $\gamma^*/Z \rightarrow \tau\tau$  and QCD background are not shown to emphasise the effect on the  $W$ +jets sample.

## 5.3. Reduction of QCD Background

As described above, the data in control region C is used as QCD background training sample. To provide good statistics and therefore a good performance result, the event selection is reduced again, as outlined in the previous section. This means, the cuts on  $E_T^{miss}$ ,  $m_T$  and the number of hadronic taus were not applied. Instead, the  $BDT_W$  was added to the event selection, in order to reduce the very prominent  $W$ +jets background in control region C.

The event yields of the selection with added  $BDT_W$  and without the  $BDT_W$  in region C are summarised in Table 5.3. As expected, the top background is largely reduced as well. Overall, the relative amount of QCD events in region C increases by over 20 % by simply applying the  $BDT_W$ . Although the QCD background provides the main background in the region, the relative QCD content is still only 81.75 %. Hence, the sample is still heavily contaminated with other backgrounds. It can also be seen, that the signal and the signal-like  $\gamma^*/Z \rightarrow \tau\tau$  decays are negligible in region C (0.04 % for signal, 1.77 % for  $\gamma^*/Z \rightarrow \tau\tau$ ). This is an important aspect, since the training should provide a good rejection performance against the background, but not the signal.

### 5.3.1. Variable Decision

The variable selection was proven to be quite difficult. Since the tau identification is using a BDT which is already trained against QCD jets and since the background sample is no pure QCD sample, it was rather challenging to find well separating variables. The final selection out of all the variables of Table C.1 is described in this section.

It was found, that the Likelihood and the BDT classifiers needed more variables for a good performance than against the  $W$ +jets background. To achieve a good performance, the rectangular cut classifier was particularly problematic. A different variable selection had to be chosen for this method. The linear correlation coefficients are shown in Figure C.3 and the variable distributions of the final selection are depicted in 5.5.

#### 5.3.1.1. Variables for the BDT and Likelihood Classifiers

The following 6 variables gave the best performance for the Likelihood and BDT method:

**Sum of the  $p_T$  of reconstructed objects** For the QCD background, this variable, which is given by Equation 5.4, has smaller values in comparison to the signal. Thus, QCD events which are misidentified as signal events, are in general low energy events.

Process	# Events without $\text{BDT}_W$	# Events with $\text{BDT}_W$
$\gamma^*/Z \rightarrow \mu^+\mu^-/e^+e^-$	2447	1004
$\gamma^*/Z \rightarrow \tau^+\tau^-$	424	244
$W \rightarrow l\nu_l$	7724	1229
top ( $t\bar{t}$ and single $t$ events)	278	38
$A/H/h \rightarrow \tau_\mu\tau_{had}$	8	5
data	26427	13807
relative amount of QCD in data	58.83 %	81.75 %

**Table 5.3.:** Event selection for QCD background reduction with and without applied  $\text{BDT}_W$ , for  $L_{\text{int}} = 4.7 \text{ fb}^{-1}$ . For the estimation of the QCD content in this region, the electroweak background and top background as well as the signal were subtracted from the data. The remaining events are assumed to be from QCD jet production, which takes up a relative amount as stated in the table.

**The angular difference in the transverse plane of the reconstructed objects** The definition of this variable can be found in Equation 5.5. It can be seen, that the signal events as well as the QCD background events are mostly back-to-back decays. Although there is no apparent separation between background and signal for this variable, the performance of the classifiers improves by adding it to the variable set.

**The difference in the  $p_T$  of the reconstructed objects** The  $\text{PtAsymmetry}$ , as defined by Equation 5.6, is depicted in the upper right corner of Figure 5.5. In comparison to the signal, the QCD events are even more symmetric. This means that the misidentified muon and hadronic tau candidates have identical transverse momenta. The signal distribution for this variable is a lot broader.

**The transverse momentum of the leading hadronic tau candidate** Not applying the requirement of one hadronic tau candidate in the event can result in events with more than one tau. The tau with the higher transverse momentum in these events, is called the leading tau. In events with only one tau, this variable describes the  $p_T$  of this tau. It is shown in the lower left edge of Figure 5.5. The QCD events generally consist of low energetic hadronic jets misidentified as taus, which is why the distribution of this variable shows exponential behaviour.

**The number of tracks from the leading hadronic tau candidate** The  $\text{LeadNTauTracks}$  variable describes the number of charged tracks following the decay of the leading hadronic tau. The background events have an overlap in the 3-prong decay (3 charged tracks). On

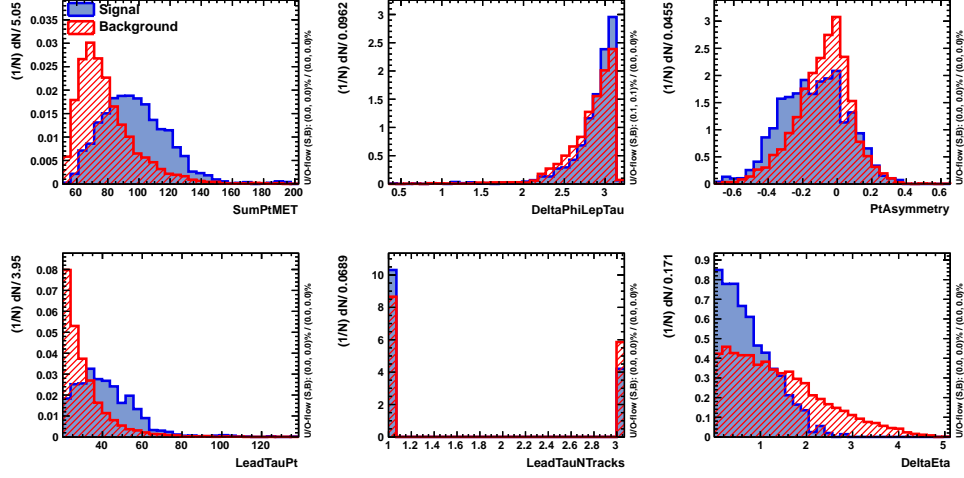


**Figure 5.5.:** Variable selection for the training against the QCD background for the BDT and Likelihood classifiers. Blue is the signal distribution, shown in red is the QCD background.

the other hand, the signal process shows more 1-prong (1 charged track) decays than the QCD background.

**The angular difference in the  $\eta$  direction of the reconstructed objects** The variable depicted in the lower right corner of Figure 5.5 describes the  $\eta$ -difference between the muon and the hadronic tau candidate:

$$\text{DeltaEta} = |\eta_{\mu} - \eta_{\tau}| \quad (5.8)$$

The signal decay products leave the interaction point generally in approximately the same  $\eta$ -direction. Hence, DeltaEta is considerably small for these events. The decay objects of the QCD background show a less correlated behaviour, which is why this distribution appears to be broader.

### 5.3.1.2. Variables for the Rectangular Cut Classifier

The variable selection described above gave a bad performance for the rectangular cut classifier. Therefore, the amount of variables used was reduced to the following selection: SumPtMET, DeltaPhiLepTau, LeadTauPt and DeltaEta. It was found that the rectangular cut method usually gave better training results, when only a few input variables were chosen.



### 5.3.2. Multivariate Analysis

For the training, the same preprocessing transformations were applied as in the training against the  $W$ +jets background. In order to improve the separation of the Likelihood and the BDT classifiers and to prevent overtraining, the configuration options of both methods had to be adjusted. The overtraining test plots are shown in Figure C.4 and the new configuration options are listed in Table C.3. Changing the configuration options of the rectangular cut classifier had no positive effect on its performance.

The response plots for Likelihood and BDT are depicted in Figure 5.6. Even with changing the configuration options, the separation between background and signal could not be improved by much, especially for the Likelihood method. This can also be seen in Table 5.4, where the discrimination significance and the separation for BDT and Likelihood are listed. Although the performance of the BDT classifier is not as good as the one achieved for the  $W$ +jets background, it still provides better results than the Likelihood method.

The ROC curve in Figure 5.7 shows almost identical behaviour for BDT and Likelihood. The rectangular cut performance, however, seems to be very unstable. All in all, the performance output of all three methods is not as good as for the  $W$ +jets training. This is probably due to the contamination of other backgrounds in the sample, which show different characteristics to the QCD background. Thus, it seems to be difficult to define a straight variable behaviour for the background sample. Additionally, the selection on the tau ID has already been applied. Hence, the part of the QCD background which is easy

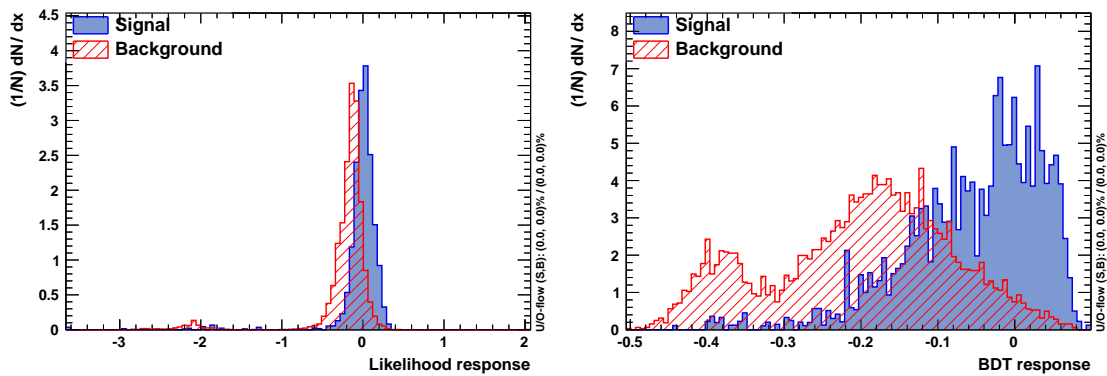


**Figure 5.6.:** Final Likelihood (left) and BDT (right) score for the training against the QCD background. As in Figure 5.5, the signal contribution is shown in blue, the QCD background contribution is shown in red. These plots are used to validate the cut score on the trained method.

	BDT	Likelihood
Significance	1.01	0.41
Separation	0.38	0.34

**Table 5.4.:** Separation and Discrimination Significance for the QCD background, for the two investigated multivariate methods, BDT and Likelihood.

to separate from the signal has already been rejected.

Nevertheless, the training output for all three classifiers was implemented in the event selection, to compare the results. Therefore a cut on the BDT score at  $-0.12$  was applied and the Likelihood selection was set on  $-0.1$  (extracted from Figure 5.6). For the rectangular cut classifier, the signal efficiency was set to 75 %.

### 5.3.3. Results and Conclusion

The results of the event selection are shown in Table 5.5, with the relative reduction in the event yield in comparison to Table 5.2 also stated. The Likelihood classifier has the worst QCD background reduction rate. The best result is delivered by the BDT, although the signal loss is a bit higher than for the other two classifiers. After careful consideration, the decision was made to apply the BDT classifier in the further event selection. Even though the cut classifier gives a similar event yield, its performance output is not regarded stable enough. In Figure 5.8, the visible mass distribution is depicted for the event selection without the  $\text{BDT}_{\text{QCD}}$  and with the  $\text{BDT}_{\text{QCD}}$ . The resulting reduction of the QCD background is very high. To check if the discriminating input variables have the same shape for the QCD content in the signal region as in the region C, as was assumed, control plots were made. For this, the cut on the applied  $\text{BDT}_{\text{QCD}}$  was inverted, hence a QCD enriched region was created. The same was carried out for the event selection in region C. Figure C.5 and Figure C.6 show the resulting distributions. The difference in both regions between the data and the Monte Carlo simulated backgrounds represents the QCD background. It can be seen, that for all distributions the shape in region A and C are similar, thus the assumption made at the start of the analysis was correct.

Applying both BDT cuts in the event selection improves the signal to background ratio from  $\frac{s}{\sqrt{b}} = 4.03$  for the event selection in Table 4.1 to

$$\frac{s}{\sqrt{b}} = 4.36, \quad (5.9)$$

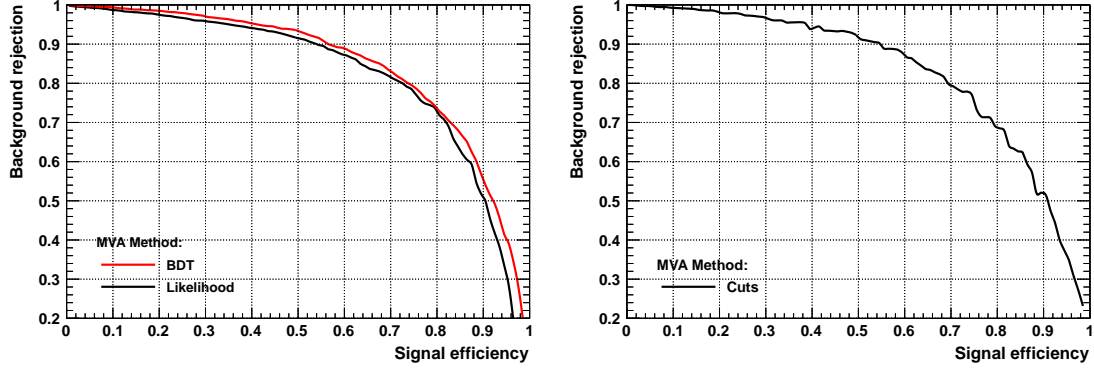


**Figure 5.7.:** The background rejection over the signal efficiency for all three investigated methods. The ROC curves for BDT and likelihood are shown on the left, the ROC curve for the rectangular cut option is shown on the right.

when assuming a signal with  $m_A = 120 \text{ GeV}$  and  $\tan\beta$ . The overall signal efficiency loss is 29.8 % whilst the background is reduced by 57.9 %. Thus, the optimisation is considered to be succesful. The significance with  $W$ +jets and QCD background only( $\frac{s}{\sqrt{b_W+b_{\text{QCD}}}}$ ) could be increased from 6.29 to 9.13. Unfortunately the irreducible  $\gamma^*/Z \rightarrow \tau\tau$  is too large to get an overall good significance for the chosen signal process.

Process	BDT		Likelihood		Rectangular Cuts	
	# Events	%	# Events	%	# Events	%
$\gamma^*/Z \rightarrow \mu^+\mu^-/e^+e^-$	209	31.7	223	27.1	213	30.4
$\gamma^*/Z \rightarrow \tau^+\tau^-$	2960	28.4	3390	18	3114	24.7
$W \rightarrow l\nu_l$	241	40.4	252	37.2	253	37.4
QCD	699	70.7	989	58.6	861	63.9
top	22	35.3	20	41.2	27	20.6
$A/H/h \rightarrow \tau_\mu\tau_{had}$	280	16.2	292	12.6	293	12.3

**Table 5.5.:** Event yields after application of multivariate methods against the QCD background, for  $L_{\text{int}} = 4.7 \text{ fb}^{-1}$ . Additionally the amount, by which the event yields got reduced in comparison to Table 5.2 is given.

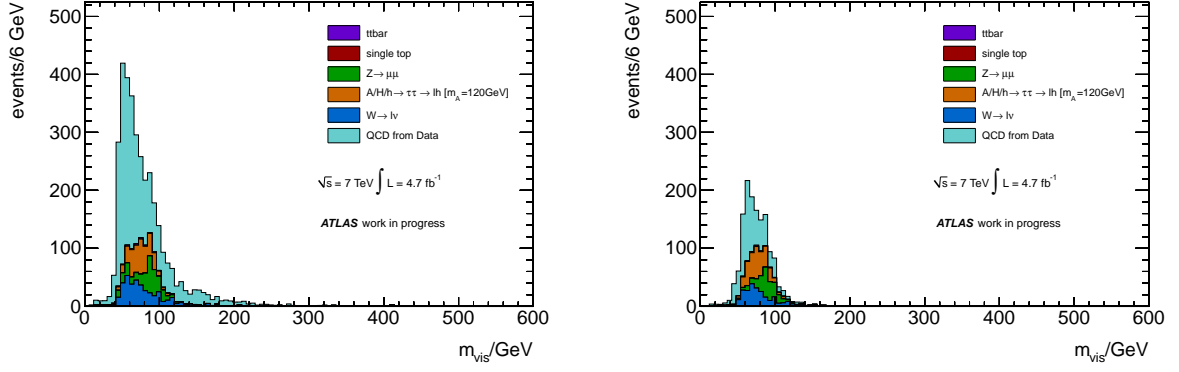


**Figure 5.8.:** The  $m_{\text{vis}}$  distribution before (left) and after (right) the new  $\text{BDT}_{\text{QCD}}$  was applied, for  $L_{\text{int}} = 4.7 \text{ fb}^{-1}$ . The  $\gamma^*/Z \rightarrow \tau\tau$  background is not shown to emphasise the effect on the QCD background.

## 6. Systematic Uncertainties

The description of the physics events, as well as the detector response in the Monte Carlo simulations is not perfect. Hence, several corrections have to be applied to the samples to match the real data. Also, the uncertainties on the background estimation have to be evaluated [68]. First, the uncertainties applied on the whole event yield are outlined. This is followed by an overview of the systematics evaluated for the reconstructed physics objects and the systematics on the background estimation processes.

### 6.1. General Systematics

In this section the systematics which were applied on the whole shape and normalisation of the samples, are described. Namely, these are the uncertainty on the luminosity, the theoretical uncertainty on the cross-sections and the statistic uncertainties. The effects of all these uncertainties on the event yields are listed in Table 6.1.

#### 6.1.1. Luminosity

The uncertainty on the luminosity is the same for all samples. To achieve a precise measurement of the physics processes, the exact determination of the delivered luminosity is crucial. Especially for the estimation of the background processes and for the purpose of evaluating the sensitivity for new physics, knowledge on the correct luminosity is important [69]. The systematic uncertainty for the integrated luminosity in this analysis is determined to 3.9% [57].

#### 6.1.2. Cross-Section

The theoretical uncertainties for the background processes are given in Table 6.1. These uncertainties are directly proportional to the resulting event yield. Hence, changing the cross-section of a sample by 5% also changes the outcoming event yield by 5%. For the  $t\bar{t}$  and single- $t$  backgrounds, no uncertainty on the cross-section was taken into account, since these backgrounds are negligible in comparison to the other backgrounds.

For the signal samples, the uncertainty on the cross-section differs for the various production processes and also depends on the type of the Higgs boson,  $m_A$  and  $\tan\beta$ . More details are given in [70] and [71]. Thus, for the gluon fusion samples, the uncertainty on the cross-section for  $\tan\beta = 20$  and  $m_A < 300$  GeV is smaller than 15 %. The upper limit on the cross-section variation of all b-associated samples is +9 %. The estimation of the lower limit for these samples is more complicated. As example, the value < 20 % is given for all samples with  $m_A > 120$  GeV [68].

### 6.1.3. Statistical Uncertainties

The statistical uncertainty is generally calculated by taking the square-root of the given event yields. Thus, the statistical uncertainty on the data was evaluated by  $\Delta N_{\text{data}} = \sqrt{N_{\text{data}}}$ . For Monte Carlo samples, the uncertainty has to be rescaled to the integrated luminosity. Hence, the statistical uncertainty was determined on the raw Monte Carlo samples and then scaled with the luminosity weight given in Equation 4.3:

$$\Delta N_{\text{MC}} = w \cdot \sqrt{N_{\text{MC}}}. \quad (6.1)$$

Process	Luminosity		Cross-section		Statistical	
	$\Delta N_{\text{events}}$	Uncertainty	$\Delta N_{\text{events}}$	Uncertainty	$\Delta N_{\text{events}}$	Uncertainty
$\gamma^*/Z \rightarrow \mu^+\mu^-/e^+e^-$	$\pm 8$	3.9 %	$\pm 11$	5 %	$\pm 12$	5.5 %
$\gamma^*/Z \rightarrow \tau^+\tau^-$	$\pm 115$	3.9 %	$\pm 148$	5 %	$\pm 57$	1.9 %
$W \rightarrow l\nu_l$	$\pm 9$	3.9 %	$\pm 12$	5 %	$\pm 16$	6.8 %
top	$\pm 1$	3.9 %	—	—	$\pm 1$	3.9 %
$A/H/h \rightarrow \tau_\mu\tau_{had}$	$\pm 11$	3.9 %	—	—	$\pm 12$	4.2 %

**Table 6.1.:** General systematic uncertainties and statistical uncertainties for all samples, for  $L_{\text{int}} = 4.7 \text{ fb}^{-1}$ . For each systematic error source, the fluctuation in the event yield as well as the relative change in the event yield is given. The QCD background is not listed, since the estimation process of the QCD background is more complex. Since the contribution of all combined top quark backgrounds is very small, no systematics on the cross-section was considered. The systematic uncertainties of the Higgs signal samples are described in the text.

## 6.2. Systematics on the Muon Candidate

For the reconstruction of the muon candidate, uncertainties on the muon energy scale, the  $p_T$  resolution and the identification efficiencies are considered. Table 6.2 summarises the effects on the event yields of all evaluated uncertainties. In Figure D.1, the effects on the visible mass distribution of the uncertainties in comparison to the normal event selection is shown.

### 6.2.1. Energy Scale

The uncertainty on the muon energy scale had to be estimated. Thus, the transverse momentum of the muon was changed by  $\pm 1\%$ . The resulting visible distributions are shown in Figure D.1. For determining the systematic uncertainty, the difference between the resulting event yields after changing the  $p_T$  and the event yields with the normal measured  $p_T$  was taken.

### 6.2.2. Resolution

The systematic uncertainty on the  $p_T$  resolution is also taken into account. Essentially, invariant mass distributions of a  $Z \rightarrow \mu\mu$  decay are compared between data and Monte Carlo samples, showing different  $p_T$  resolutions for data and Monte Carlo. Thus, the difference on the  $p_T$  resolution of the muon candidates can be obtained [72]. To achieve the data resolution, the muon  $p_T$  is smeared by using a dedicated software tool. Before the smearing, the muon preselection was applied. The difference in the event yields between smeared and unsmeared samples is taken as systematic uncertainty.

### 6.2.3. Identification Efficiency

The muon identification efficiencies differ between data and Monte Carlo simulation. Thus, a scale factor, which depends on  $\eta$  and the muon  $p_T$ , was applied to the Monte Carlo samples. This was carried out as an event weight applied by a provided software tool, after the muon preselection was employed. Again, the difference between scaled and unscaled event yields are used as systematic uncertainties.

## 6.3. Systematics on the Hadronic Tau Candidate

As main systematic uncertainties for the hadronic tau candidate reconstruction, the tau energy scale and the tau identification efficiency were taken into account. The effects on

Process	Muon Energy Ecale		Muon Resolution		Muon Ident. Efficiency	
	$\Delta N_{\text{events}}$	Uncertainty	$\Delta N_{\text{events}}$	Uncertainty	$\Delta N_{\text{events}}$	Uncertainty
$\gamma^*/Z \rightarrow \mu^+\mu^-/e^+e^-$	$^{+2}_{-3}$	$^{+0.9}_{-1.3} \%$	$\pm 2$	0.8 %	$\pm 3$	1.5 %
$\gamma^*/Z \rightarrow \tau^+\tau^-$	$^{+65}_{-87}$	$^{+2.2}_{-2.9} \%$	$\pm 11$	0.4 %	$\pm 40$	1.4 %
$W \rightarrow l\nu_l$	$^{+0}_{-2}$	$^{+0}_{-0.9} \%$	$\pm 2$	0.9 %	$\pm 4$	1.4 %
top	$\pm 0$	$^{+0.6}_{-1.7} \%$	$\pm 0$	0.1 %	$\pm 0$	1.6 %
$A/H/h \rightarrow \tau_\mu \tau_{had}$	$^{+5}_{-4}$	$^{+1.7}_{-1.5} \%$	$\pm 2$	0.5 %	$\pm 4$	1.4 %

**Table 6.2.:** Muon systematic uncertainties for all samples. For each systematic, the fluctuation in the event yield as well as the relative change in the event yield is given, for  $L_{\text{int}} = 4.7 \text{ fb}^{-1}$ . The QCD is not listed, since the estimation process of the QCD background is more complex.

the event yields are listed in Table 6.3 and the resulting  $m_{vis}$  distributions are depicted in Figure D.2.

### 6.3.1. Energy Scale

Similar to the muon candidates, the systematic uncertainty on the tau energy scale was determined. To obtain the systematic uncertainty, the  $p_T$  was varied between  $\pm 3.5 \%$  and  $\pm 9.5 \%$ , depending on the number of charged tracks found and the  $\eta$ - and  $p_T$ -range, in which the candidate was reconstructed [58]. In Table D.1, the specific variation values are listed. The procedure was carried out before the tau selection criteria were applied. Using the differences between the changed event yields and the obtained event yields without varying the tau  $p_T$ , the systematic uncertainty was estimated.

### 6.3.2. Identification Efficiency

The tau identification efficiencies were calculated by [58]. For hadronic taus with a  $p_T > 20 \text{ GeV}$  and a medium BDT criterion against the QCD background<sup>7</sup>, the uncertainty on the tau identification efficiency is 9.9 %. The uncertainty was applied as an event weight after selecting the hadronic tau candidate. It transfers linearly to the event yields, as shown in Table 6.3.

<sup>7</sup>Meant is the BDT, which was applied in the preselection, not the one obtained during the selection optimisation process.



Process	Tau Energy Scale		Tau Identification Efficiency	
	$\Delta N_{\text{events}}$	Uncertainty	$\Delta N_{\text{events}}$	Uncertainty
$\gamma^*/Z \rightarrow \mu^+\mu^-/e^+e^-$	$+4$ $-7$	$+1.8$ $-3.5$ %	$\pm 21$	9.9 %
$\gamma^*/Z \rightarrow \tau^+\tau^-$	$+109$ $-153$	$+3.7$ $-5.2$ %	$\pm 293$	9.9 %
$W \rightarrow l\nu_l$	$+17$ $-19$	$+7.1$ $-7.9$ %	$\pm 24$	9.9 %
top	$+1$ $-2$	$+6.3$ $-10.3$ %	$\pm 2$	9.9 %
$A/H/h \rightarrow \tau_\mu\tau_{had}$	$+8$ $-10$	$+2.8$ $-3.5$ %	$\pm 28$	9.9 %

**Table 6.3.:** Tau systematic uncertainties for all samples. For each systematic, the fluctuation in the event yield as well as the relative change in the event yield is given, for  $L_{\text{int}} = 4.7 \text{ fb}^{-1}$ . The QCD is not listed, since the estimation process of the QCD background is more complex.

## 6.4. Systematics on the Background Estimation

Finally, the systematic uncertainties for the  $W$ +jets background and the QCD background estimation are evaluated. The effects on the event yields for both samples are summarised in Table 6.4.

### 6.4.1. $W$ +jets Scaling Factor

To obtain the uncertainty on the scaling factor  $k_W$ , the combined uncertainty on the subtracted Monte Carlo samples was used. The combined uncertainties were evaluated by

$$\Delta N_{\text{total}} = \sqrt{\Delta N_{\text{stat}}^2 + \Delta N_{\text{lumi}}^2 + \Delta N_{\text{xsec}}^2 + \cdots + \Delta N_{\text{id-eff}}^2} \quad (6.2)$$

In the case of asymmetric uncertainties, two values were determined, one for the positive uncertainties and one for the negative uncertainties. The results were applied as additional scaling weights to the Monte Carlo samples, before they were subtracted from the data in the  $W$ +jets control region. Two new scaling factors were calculated. The difference to the scaling factor  $k_W$  obtained in Section 4.3.1 was taken as uncertainty on  $k_W$ :

$$k_W = 0.51 \pm 0.01 \quad (6.3)$$

With these new scaling factors, new event yields for the  $W$ +jets samples were attained. The differences in the event yields was used to estimate the systematic uncertainty for the  $W$ +jets samples.

### 6.4.2. QCD Estimation

For the uncertainty on the QCD estimation, the uncertainties in each control region have to be considered. In all three control regions, the above stated uncertainties were evaluated again. Also, in region B and D the statistical uncertainties were determined [73]. The combined systematic uncertainties (obtained with Equation 6.2) are stated in Table D.4 and the statistical uncertainties are listed in Table D.3. Additionally, the event yields in the QCD control regions after applying the optimised event selection, are summarised in Table D.2.

Furthermore, the uncertainties on the  $k_W$  scaling factor were considered in each region. Thus, the uncertainties for the  $k_W$  factor in the same sign regions C and D were provided by the same procedure as described in Section 6.4.1:

$$k_W(SS) = 0.61 \pm 0.01 \quad (6.4)$$

The combined uncertainties were then calculated by:

$$\Delta N_{\text{region}} = \sqrt{\Delta N_{\text{data},\text{region}}^2 + \Delta N_{\text{MC},\text{region}}^2}, \quad (6.5)$$

where  $\Delta N_{\text{data},\text{region}}$  is the statistical uncertainty for the data and  $\Delta N_{\text{MC},\text{region}}$  the uncertainty on the Monte Carlo simulations obtained by Equation 6.2 for each region. As stated above, the statistical uncertainties in region C were not considered. The resulting uncertainties on  $r_{\text{OS/SS}}$  are:

$$r_{\text{OS/SS}} = 1.14_{-0}^{+0.01} \quad (6.6)$$

Using the propagation of uncertainty, the uncertainty on the QCD event yield in the signal region is estimated:

$$\Delta N_A^{\text{QCD}} = \sqrt{\left(\frac{\Delta N_B}{N_D} \cdot N_C\right)^2 + \left(\frac{N_B}{N_D^{-2}} \cdot N_C \cdot \Delta N_D\right)^2 + \left(\frac{N_B}{N_D} \cdot \Delta N_C\right)^2} \quad (6.7)$$

## 6.5. Results and Conclusion

In Table 6.5 the combined systematic and statistical uncertainties for each background sample, estimated by Equation 6.2, are listed. The main uncertainties are provided by the uncertainty on the tau identification efficiency. Also, the contributions of the tau energy scale uncertainties are considerably large. Hence, future analyses may study potential improvements on the reconstruction of the hadronic tau candidates to reduce the uncer-

Process	$W$ +jets estimation		QCD estimation	
	$\Delta N_{\text{events}}$	Uncertainty	$\Delta N_{\text{events}}$	Uncertainty
$W \rightarrow l\nu_l$	$^{+4}_{-3}$	$^{+1.5}_{-1.4} \%$	—	—
QCD	—	—	$^{+87}_{-60}$	$^{+12.4}_{-8.6} \%$

**Table 6.4.:** Systematic uncertainties on the background estimation, for  $L_{\text{int}} = 4.7 \text{ fb}^{-1}$ . For each systematic, the fluctuation in the event yield as well as the relative change in the event yield is given.

Process	uncertainty
$\gamma^*/Z \rightarrow \mu^+\mu^-/e^+e^-$	$^{+13.3}_{-13.6} \%$
$\gamma^*/Z \rightarrow \tau^+\tau^-$	$^{+12.7}_{-13.4} \%$
$W \rightarrow l\nu_l$	$^{+15.4}_{-15.9} \%$
QCD	$^{+12.4}_{-8.6} \%$
top ( $t\bar{t}$ and single $t$ events)	$^{+13.3}_{-15.4} \%$

**Table 6.5.:** Combined relative uncertainties evaluated out of the systematic uncertainties and the statistic uncertainties with Equation 6.2, for  $L_{\text{int}} = 4.7 \text{ fb}^{-1}$ .

ainties in the Monte Carlo samples. The positive and negative uncertainties are in the same order of magnitude, apart from the uncertainties on the QCD background, which is due to the complex estimation procedure for this background. Little changes in the uncertainties for the subtracted Monte Carlo samples, thus have a large impact on the uncertainties for the QCD background.



# 7. Results

## 7.1. Signal Efficiency Loss

The optimisation of the event selection was carried out with the  $m_A = 120$  GeV,  $\tan\beta = 20$  signal sample. With the selected methods, the overall signal efficiency loss for this sample is 29.8 %. It is now essential to know, how the chosen classifiers behave for other values of  $m_A$  and other values of  $\tan\beta$ . To get a general understanding, how the different Higgs samples respond to varying classifier combinations and to cross check the behaviour of the chosen BDT classifiers, all possible arrangements are compared.

The Higgs samples used are generated for

$$m_A = (90, 110, 120, 130, 140, 170, 200, 250, 300) \text{ GeV}.$$

The cross-section of the Higgs bosons is proportional to  $\tan^2\beta$  [74], thus samples for different  $\tan\beta$  values can be obtained by changing the cross-section accordingly. Hence, the resulting signal efficiency loss for the same  $m_A$  mass point but different  $\tan\beta$  is in the same order of magnitude for all  $\tan\beta$  values. The signal event yields for the selection without applying the classifiers and for all classifier combinations is shown in Tables E.1 - E.10, for an integrated luminosity of  $L_{\text{int}} = 4.7 \text{ fb}^{-1}$ . For the analysis,  $\tan\beta$  values from 5 to 50 were considered, in steps of 5. Table 7.1 shows the signal efficiency loss for different mass points and all classifier combinations. The given values are the average over all considered  $\tan\beta$ .

All classifier combinations show essentially the same behaviour. For the mass point used for the training and all mass points with similar values, the signal efficiency loss is around 30 %. In the high and low mass regions, the signal efficiency loss is considerably higher. This behaviour can especially be seen when using the rectangular cut classifier against the  $W$ +jets background. Therefore, in order to achieve better responses for all mass regions, the training has to be carried out separately for the low and high mass regions in future analyses.

$m_A/\text{GeV}$ :	90	110	120	130	140	170	200	250	300
BDT <sub>W</sub> +BDT <sub>QCD</sub>	50.2 %	31.3 %	30.1 %	28.4 %	26.4 %	32.8 %	42.2 %	51 %	55 %
BDT <sub>W</sub> +LLH <sub>QCD</sub>	42.8 %	25.2 %	27.1 %	26.7 %	25 %	34.4 %	49.1 %	45.7 %	78.9 %
BDT <sub>W</sub> +Cut <sub>QCD</sub>	46.9 %	28.2 %	26.7 %	24.3 %	23.7 %	30.5 %	40.2 %	47.5 %	49.8 %
LLH <sub>W</sub> +BDT <sub>QCD</sub>	49.2 %	31 %	30 %	26.4 %	23.1 %	21.3 %	22.8 %	27.4 %	31 %
LLH <sub>W</sub> +LLH <sub>QCD</sub>	40.8 %	24.1 %	27.2 %	24.9 %	22.4 %	24.2 %	33.9 %	57.6 %	72.7 %
LLH <sub>W</sub> +Cut <sub>QCD</sub>	44.9 %	27.5 %	26.3 %	21.9 %	20.1 %	18.4 %	20.1 %	22.7 %	24.1 %
Cut <sub>W</sub> +BDT <sub>QCD</sub>	57.4 %	39.8 %	37.2 %	40 %	36.8 %	51.5 %	65.4 %	83.4 %	91.3 %
Cut <sub>W</sub> +LLH <sub>QCD</sub>	51.4 %	35.6 %	34.9 %	39.2 %	35.8 %	52.4 %	68.3 %	85 %	91.3 %
Cut <sub>W</sub> +Cut <sub>QCD</sub>	57.3 %	37.6 %	35.1 %	37.9 %	35.2 %	49.7 %	64.7 %	82.1 %	90.5 %

**Table 7.1.:** Signal efficiency loss for different Higgs masses  $m_A$  for different variations of multivariate methods, for  $L_{\text{int}} = 4.7 \text{ fb}^{-1}$ . The given values are the average over different  $\tan\beta$  values (from  $\tan\beta = 5$  to  $\tan\beta = 50$  in steps of 5). LLH stands for the Likelihood classifier.

## 7.2. Significance

To describe the sensitivity of an experiment, the significance  $Z$  is used. For substantially large backgrounds in comparison to the signal, the significance is evaluated by

$$Z = \frac{s}{\sqrt{b + (\Delta b)^2}}. \quad (7.1)$$

In this equation,  $s$  describes the signal event yield and  $b$  stands for the combined background event yield. For a discovery, the significance has to be at least  $Z = 5$  [75]. The uncertainties in Table 6.5 are taken into consideration as value  $\Delta b$  in Equation 7.1.

The significance values for different  $\tan\beta$  and  $m_A$  hypotheses are shown in Figure 7.1, where only Monte Carlo samples and the results of the background estimation were used for  $s$  and  $b$ . No working point exceeds the  $Z = 5$  necessary for a discovery with a luminosity of  $L_{\text{int}} = 4.7 \text{ fb}^{-1}$ . One reason for that is the relatively large irreducible  $\gamma^* / Z \rightarrow \tau\tau$  background and the resulting large uncertainties on this background. Additionally, the analysis was only carried out in the decay channel  $A/H/h \rightarrow \tau^+\tau^- \rightarrow \mu + \tau_{\text{had}} + \nu_\mu + 2\nu_\tau$ . Combining results with the electron channel may improve the discovery potential.

## 7.3. Comparison between Backgrounds and Data

In order to find potential discoveries, the data taken has to be compared to the estimated background with considering the evaluated uncertainties as well. In Table 7.2 the resulting event yields for all background processes and the data are summarised. The visible mass

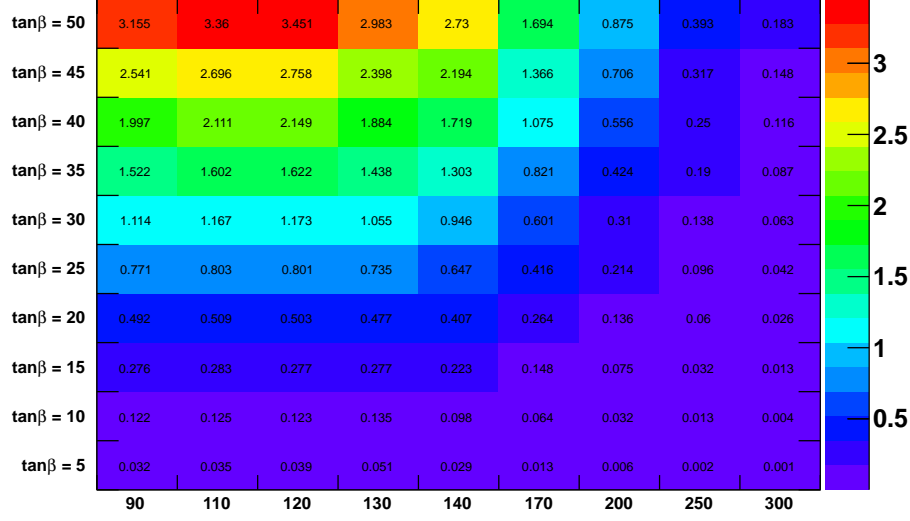


**Figure 7.1.:** The significance evaluated by Equation 7.1 after applying the optimised event selection for different Higgs samples, for  $L_{\text{int}} = 4.7 \text{ fb}^{-1}$ . The x-axis depicts the Higgs mass  $m_A$ , the y-axis shows different values of  $\tan\beta$ .

distribution  $m_{vis}$  for background and data is depicted in Figure 7.2. Additionally, the kinematic variables for both, muon and hadronic tau respectively, are shown in Figure E.1.

It can be seen in general, that there is a slight overestimation of the background processes. Especially comparing the sum of all background samples to the data in Table 7.2 shows, that the Monte Carlo samples seem to slightly miscalculate the expected background. However, within the uncertainties, both event yields overlap. Nevertheless, a potential miscalculation might be due to an overestimation of the  $Z$ +jets background. As in the  $W$ +jets samples, the Monte Carlo miscalculates the possibility of misidentifying associated jets as hadronic tau candidates [64]. Obtaining a normalisation factor by defining a  $Z$ +jets control region might solve the slight overestimation. The shapes of the distributions (kinematic variables in Figure E.1 as well as the  $m_{vis}$  distribution in Figure 7.2) however mostly agree between the data and the background, within the given uncertainties.

Sample	events
$\gamma^*/Z \rightarrow \mu^+\mu^-/e^+e^-$	$209 \pm 12(\text{stat.}) \pm_{26}^{25}(\text{syst.})$
$\gamma^*/Z \rightarrow \tau^+\tau^-$	$2960 \pm 57(\text{stat.}) \pm_{392}^{372}(\text{syst.})$
$W \rightarrow l\nu_l$	$241 \pm 16(\text{stat.}) \pm_{34}^{33}(\text{syst.})$
QCD	$699 \pm_{60}^{87}(\text{syst.})$
top ( $t\bar{t}$ and single $t$ events)	$22 \pm 1(\text{stat.}) \pm 3(\text{syst.})$
Sum	$4131 \pm 60(\text{stat.}) \pm_{399}^{384}(\text{syst.})$
Data	$3910 \pm 63(\text{stat.})$

**Table 7.2.:** Remaining Events after all new selection criteria have been applied, for all background distributions without any signal, for  $L_{\text{int}} = 4.7 \text{ fb}^{-1}$ . For comparison, the event yields are added and the data is also stated.

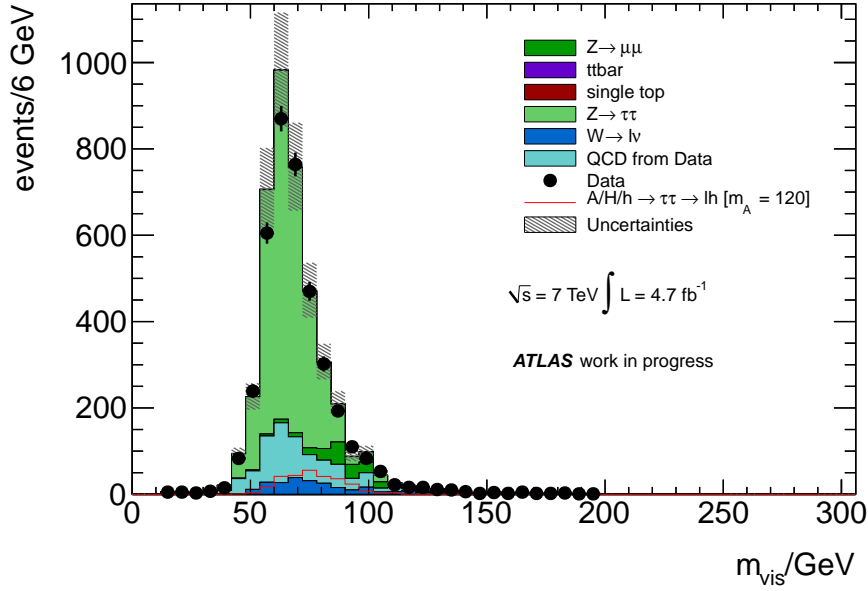


**Figure 7.2.:** The final distribution of the visible mass,  $m_{\text{vis}}$ , after applying the optimised event selection with the two BDT classifiers, for  $L_{\text{int}} = 4.7 \text{ fb}^{-1}$ . The data and error bars are also depicted.



## 8. Conclusion

By using multivariate methods, the event selection in the MSSM Higgs boson search in the decay channel  $A/H/h \rightarrow \tau^+\tau^- \rightarrow \mu + \tau_{had} + \nu_\mu + 2\nu_\tau$  was optimised in this analysis. Three different classifiers were trained to reject the  $W$ +jets background and the QCD events, respectively. In both cases, the performance of all three classifiers were compared and the Boosted Decision Tree classifier was showing the best results. Especially with respect to future analyses with increased statistics, the BDT classifiers occur to be the best choice, since the output was stable and the signal efficiency loss in contrast to the background rejection was improved in comparison to the other classifiers.

The optimisation of the MSSM Higgs Boson search was successful. The overall background was reduced by 57.9%. Especially, the training against the specific backgrounds which were tried to be reduced, was very effective. The  $W$ +jets background was reduced by 69.3%. As a side effect of the  $W$ +jets rejection, the  $t\bar{t}$  and single- $t$  backgrounds were reduced by 87.2%. Similar results were achieved for the QCD jet background, which was overall reduced by 78.4%. The signal efficiency loss depends very much on the chosen Higgs sample, but for the low mass region, excluding Higgs bosons for  $m_A = 90$  GeV and below, the signal efficiency loss is about 30%. For  $m_A = 200$  GeV and above it is recommended to use separately trained multivariate classifiers in future analyses. The  $\frac{s}{\sqrt{b}}$  significance was improved by 8.1% to

$$\frac{s}{\sqrt{b}} = 4.36,$$

for the  $m_A = 120$  GeV,  $\tan\beta = 20$  working point, respectively. The BDT classifiers were implemented in the event selection after the cuts on the missing transverse energy and the transverse mass.

For a discovery of the Higgs boson, the signal would not yet be significant enough. The irreducible  $\gamma^*/Z \rightarrow \tau\tau$  background is still too substantial. Thus, future analyses may study different ways to separate between the signal and the  $\gamma^*/Z \rightarrow \tau\tau$  process. To reduce background in general, and hence increase the significance in this search channel, combining the analysis in the  $A/H/h \rightarrow \tau^+\tau^- \rightarrow \mu + \tau_{had} + \nu_\mu + 2\nu_\tau$  channel with the analysis in the  $A/H/h \rightarrow \tau^+\tau^- \rightarrow e + \tau_{had} + \nu_e + 2\nu_\tau$  channel may improve the results. Furthermore,

carrying out an exclusive analysis, so therefore using a b-tag on jets containing b-quarks, reduces the background considerably [41]. Within the systematic and statistical uncertainties, the estimated background agrees well with the data. Still, a slight overestimation of the background becomes apparent in the Monte Carlo simulations. Thus, a cross-check with a data-driven background estimation for the  $\gamma^*/Z \rightarrow ll$  is recommended in future analyses. Also, an improvement of the hadronic tau candidate reconstruction in order to reduce the large systematic uncertainties on the tau identification efficiency and the tau energy scale, may increase the possibility to find a potential signal.

# A. Appendix - Monte Carlo Samples and Event Selection

Background Process	Dataset Number	Generator	$\sigma/\text{pb}^{-1}$
$t\bar{t}$	105200, 105204	MC@NLO	329.1
single $t$ , $t$ -channel and $s$ -channel	117360 - 117365	ACERMC	22.3
single $t$ , $Wt$ -channel	108346	MC@NLO	13.1
$W^\pm \rightarrow \nu_e e^\pm$	107680 - 107685	ALPGEN	10486
$W^\pm \rightarrow \nu_\mu \mu^\pm$	107690 - 107695	ALPGEN	10483
$W^\pm \rightarrow \nu_\tau \tau^\pm$	107700 - 107705	ALPGEN	10481
$\gamma^*/Z \rightarrow e^+e^-$ , $10 \text{ GeV} < m_{ll} < 40 \text{ GeV}$	116250 - 116255	ALPGEN	3895
$\gamma^*/Z \rightarrow \mu^+\mu^-$ , $10 \text{ GeV} < m_{ll} < 40 \text{ GeV}$	116260 - 116265	ALPGEN	3894
$\gamma^*/Z \rightarrow \tau^+\tau^-$ , $10 \text{ GeV} < m_{ll} < 40 \text{ GeV}$	116270 - 116275	ALPGEN	3895
$\gamma^*/Z \rightarrow e^+e^-$	107650 - 107655	ALPGEN	1073
$\gamma^*/Z \rightarrow \mu^+\mu^-$	107660 - 107665	ALPGEN	1072
$\gamma^*/Z \rightarrow \tau^+\tau^-$	107670 - 107675	ALPGEN	1073

**Table A.1.:** Background Monte Carlo Samples used in the analysis, with the number of the used dataset and the Monte Carlo generator. Also, the cross-section,  $\sigma$ , for each process is given.

b-associated production $A/H/h \rightarrow \tau^+\tau^- \rightarrow l + \text{hadrons} + 2\nu_\tau + \nu_l$ :		
$m_A$	Generator	$\sigma \times \mathcal{BR}(\text{pb})$
90	SHERPA	17.72
110	SHERPA	9.56
120	SHERPA	6.991
130	SHERPA	5.59
140	SHERPA	3.84
170	SHERPA	2.09
200	SHERPA	1.13
250	SHERPA	0.45
300	SHERPA	0.19
gluon fusion $A/H/h \rightarrow \tau^+\tau^- \rightarrow l + \text{hadrons} + 2\nu_\tau + \nu_l$ :		
$m_A$	Generator	$\sigma \times \mathcal{BR} \text{ (pb)}$
90	POWHEG+PYTHIA	18.08
110	POWHEG+PYTHIA	6.69
120	POWHEG+PYTHIA	4.12
130	POWHEG+PYTHIA	3.62
140	POWHEG+PYTHIA	2.1
170	POWHEG+PYTHIA	0.76
200	POWHEG+PYTHIA	0.31
250	POWHEG+PYTHIA	0.09
300	POWHEG+PYTHIA	0.027

**Table A.2.:** Signal Monte Carlo Samples used in the analysis, with the production cross-sections for  $A/H/h$ , multiplied by the branching ratios for  $A/H/h \rightarrow \tau\tau$  and  $\tau\tau \rightarrow lh$  in the case of  $\tan\beta = 20$ .

$m_A$	$m_h$	$m_H$
90	89.6	130.6
110	109	131.1
120	118.2	132
130	125.2	134.9
140	128.9	142.1
170	129.4	170.7
200	129.7	200.5
250	129.8	250.4
300	129.8	300.4

**Table A.3.:** Masses for the neutral MSSM Higgs bosons in the  $m_h^{\max}$  benchmark scenario for  $\tan\beta = 20$  [68].

Object	Selection
vertex	minimum number of associated tracks = 4 type = 1 (primary vertex)
muons	$p_T > 10 \text{ GeV}$ $ \eta  < 2.5$ loose staco muons
	<b>Track requirements:</b> expected BLayer Hit = 0 or number of BLayer Hits $> 0$ number of Pixel Hits + number of Dead Pixels $> 1$ number of SCT Hits + number of Dead SCT $> 5$ Pixel Holes + SCT Holes $< 3$ for $ \eta  < 1.9$ , require TRT Hits + TRT Outliers $> 5$ and $\frac{\text{TRT Outliers}}{\text{TRT Hits} + \text{TRT Outliers}} < 0.9$ for $ \eta  > 1.9$ and TRT Hits + TRT Outliers $> 5$ , require $\frac{\text{TRT Outliers}}{\text{TRT Hits} + \text{TRT Outliers}} < 0.9$  dilepton veto (require exactly one muon)
taus	$p_T > 20 \text{ GeV}$ $ \eta  < 2.5$ author cuts = 1 or 3 number or tracks = 1 or 3 $ Q  = 1$ BDT medium ID BDT based electron veto score = 0.51
jets	$p_T > 20 \text{ GeV}$ $ \eta  < 4.5$ anti- $k_T$ jets with $\Delta R = 0.4$
MET	$\text{MET\_LocHadTopo} + \text{MET\_MuonBoy} - \text{MET\_RefMuon\_Track}$
Overlap Removal	$\Delta R < 0.2$ carried out in the order muon, electron, tau, jet
trigger for muon channel	before run period I: EF_mu18_MG from period J: EF_mu18_MG_medium

**Table A.4.:** Event Preselection criteria for the MSSM Higgs boson search in the channel  $A/H/h \rightarrow \tau^+\tau^- \rightarrow \mu + \tau_{had} + \nu_\mu + 2\nu_\tau$ .

Object	Selection
jets	for data use BCH corrected $p_T$ $\left(p_T = p_T \cdot \frac{1-\text{BCH\_Corr\_Cell}}{1-\text{BCH\_Corr\_Jet}}\right)$ $p_T > 20 \text{ GeV}$ <b>reject events within:</b> $-0.2 < \eta < 1.6$ $-0.988 < \Phi < -0.392$
taus	<b>reject events within:</b> $-0.1 < \eta < 1.55$ $-0.9 < \Phi < -0.5$

**Table A.5.:** Cuts on different objects for the treatment of the liquid argon hole during data run period 180614 - 184169 (applied on data and MC), for the MSSM Higgs boson search in the channel  $A/H/h \rightarrow \tau^+\tau^- \rightarrow \mu + \tau_{had} + \nu_\mu + 2\nu_\tau$ .

Object	Selection
muons	$p_T > 20 \text{ GeV}$ combined muons <b>isolation criteria:</b> $\frac{etcone20}{p_T} < 0.04$ <sup>2</sup> $\frac{ptcone40}{p_T} < 0.06$ <sup>3</sup>
taus	number of hadronic tau candidates = 1
charge	$Q_{lep} \cdot Q_\tau = -1$
MET	$E_T^{miss} > 20 \text{ GeV}$
$m_T$ (compare to eq. 4.4)	$m_T < 30 \text{ GeV}$

**Table A.6.:** Analysis Level Selection criteria for the MSSM Higgs boson search in the channel  $A/H/h \rightarrow \tau^+\tau^- \rightarrow \mu + \tau_{had} + \nu_\mu + 2\nu_\tau$ .

<sup>2</sup>For a cone of  $\Delta R < 0.2$  around the muon track, the sum of all track  $E_T$  has to be lower than 4 % of the muon  $p_T$ .

<sup>3</sup>For a cone of  $\Delta R < 0.4$  around the muon track, the sum of all track  $p_T$  has to be lower than 6 % of the muon  $p_T$ .

## B. Appendix - Background Estimation

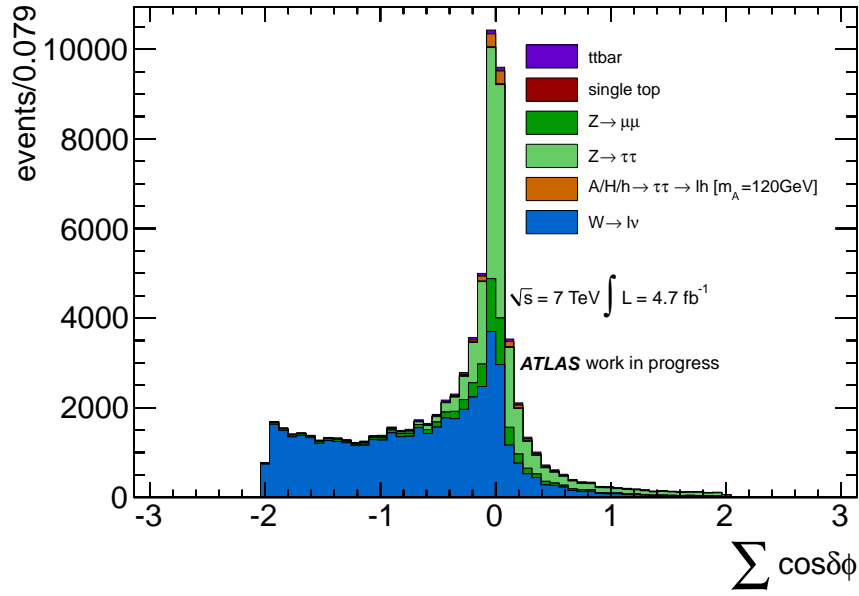


**Figure B.1.:** The  $\sum \cos \Delta \Phi$  distribution for all process samples, for  $L_{\text{int}} = 4.7 \text{ fb}^{-1}$ . The small  $\sum \cos \Delta \Phi$  is dominated by the  $W$ +jets background.

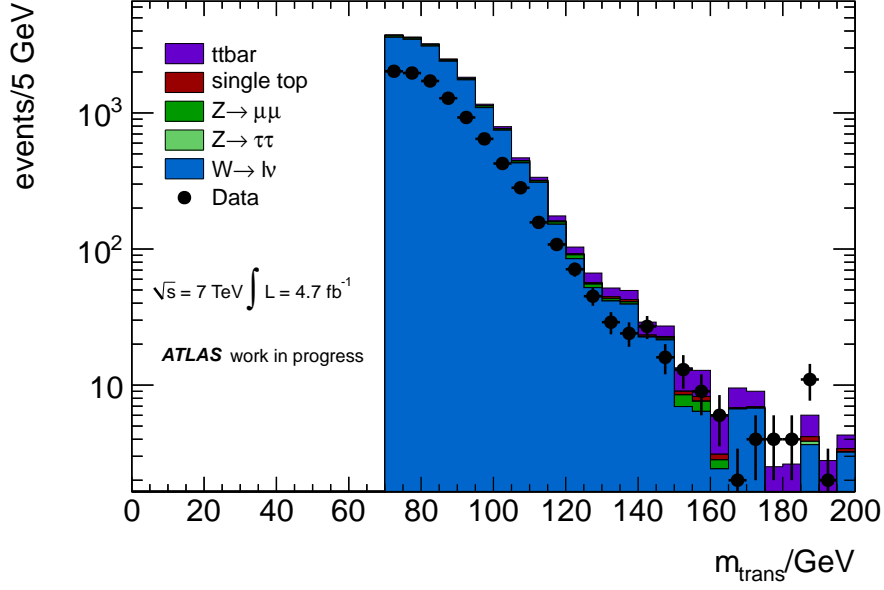


**Figure B.2.:** The transverse mass  $m_T$  in the  $W$ +jets control region before renormalisation and after the cut on  $m_T$  in a logarithmic scale, for  $L_{\text{int}} = 4.7 \text{ fb}^{-1}$ . The ratio between the data and the  $W$ +jets Monte Carlo simulation seems to be constant, which is why  $k_W$  is estimated by using the integral over the data and the  $W$ +jets events.

Region	Selection Cuts
A	$Q_\tau \cdot Q_\mu = -1$ $\frac{\text{etcone20}}{p_T} < 0.04$ $\frac{\text{ptcone40}}{p_T} < 0.06$ (compare to Table A.6)
B	$Q_\tau \cdot Q_\mu = -1$ $\frac{\text{etcone20}}{p_T} > 0.04$ $\frac{\text{ptcone40}}{p_T} > 0.06$
C	$Q_\tau \cdot Q_\mu = 1$ $\frac{\text{etcone20}}{p_T} < 0.04$ $\frac{\text{ptcone40}}{p_T} < 0.06$ (compare to Table A.6)
D	$Q_\tau \cdot Q_\mu = 1$ $\frac{\text{etcone20}}{p_T} > 0.04$ $\frac{\text{ptcone40}}{p_T} > 0.06$

**Table B.1.:** Control region cuts for the QCD background estimation. Region A is the signal region, where all cuts are applied as described in Section 4.2. Region B to D are QCD enriched control regions, where one or two cuts from region A are reversed.



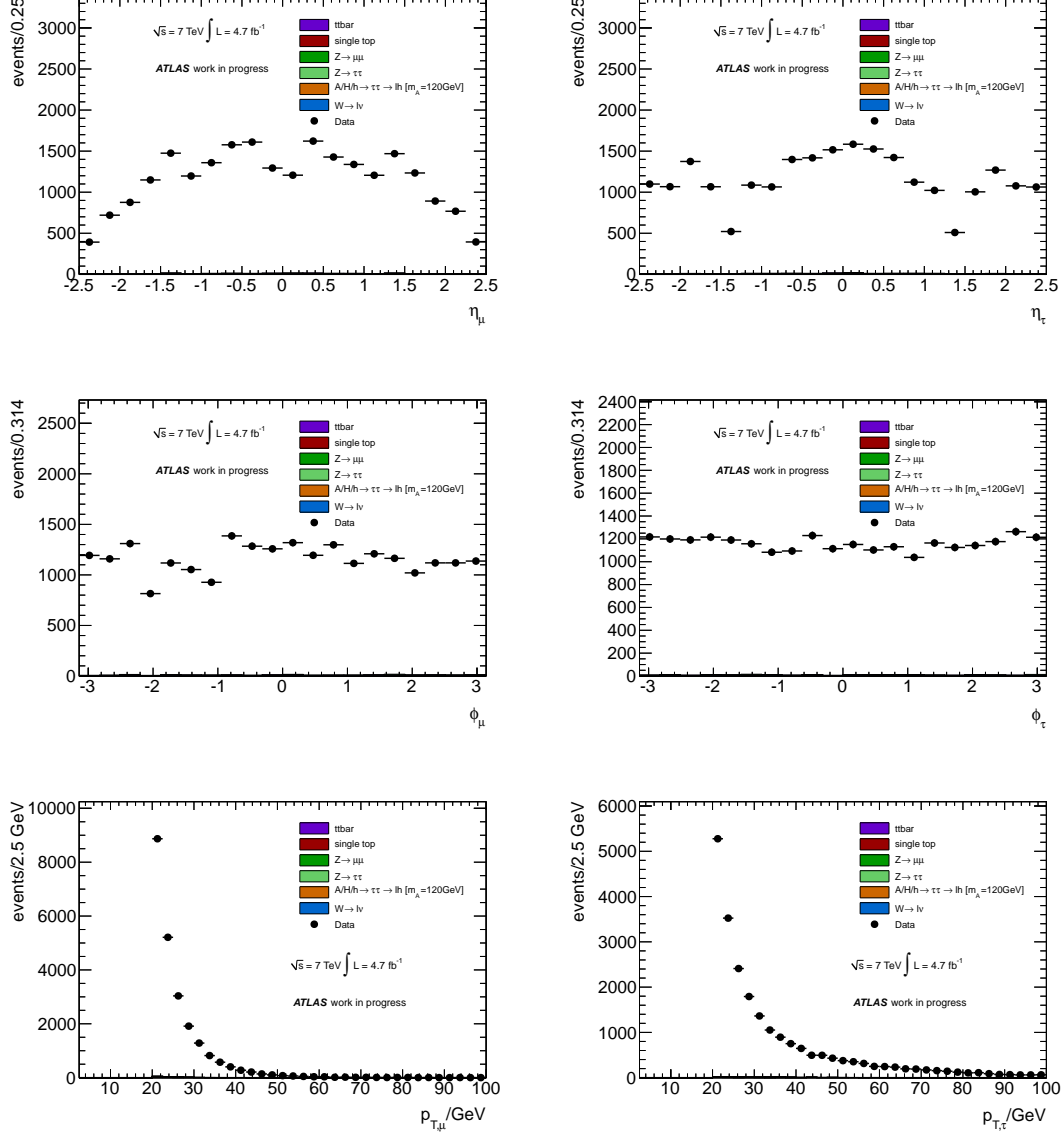


**Figure B.3.:** Plots for the kinematic variables  $\eta$  (first row),  $\Phi$  (second row) and  $p_T$  (third row) for QCD control region B, for  $L_{\text{int}} = 4.7 \text{ fb}^{-1}$ . The muon distributions are depicted on the left, the tau variables are shown on the right. The simulated Monte Carlo background samples are also plotted, but they show too low statistics in this region. It can be seen, that this region is highly dominated by QCD background (difference between data and the Monte Carlo samples).

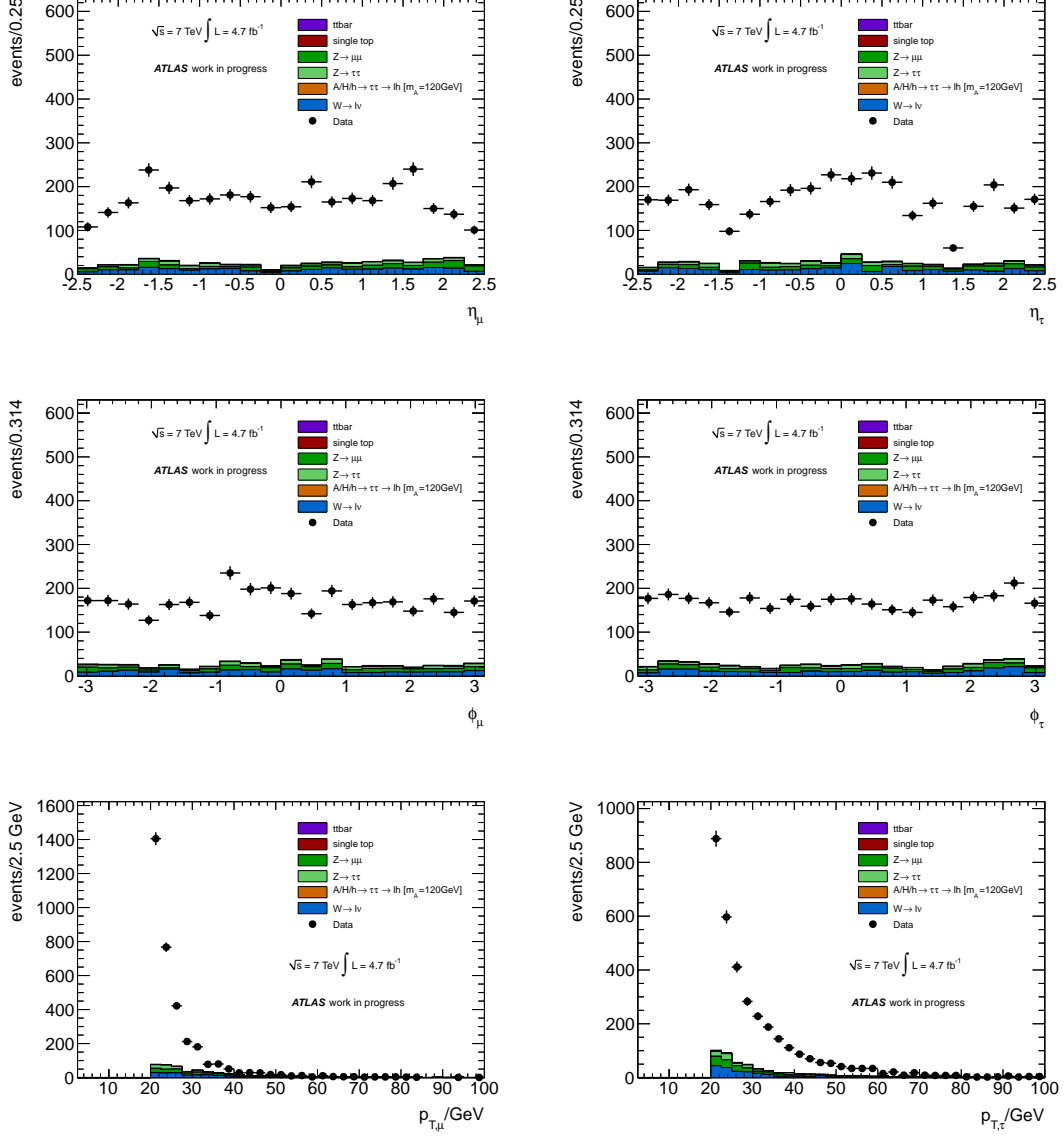


**Figure B.4.:** Plots for the kinematic variables  $\eta$  (first row),  $\Phi$  (second row) and  $p_T$  (third row) for QCD control region C, for  $L_{\text{int}} = 4.7 \text{ fb}^{-1}$ . The muon distributions are depicted on the left, the tau variables are shown on the right. The simulated Monte Carlo background samples are also plotted. It can be seen, that this region is dominated by QCD background (difference between the data and the Monte Carlo samples). Nevertheless, a significant contribution from the other background distributions apparent is also apparent.

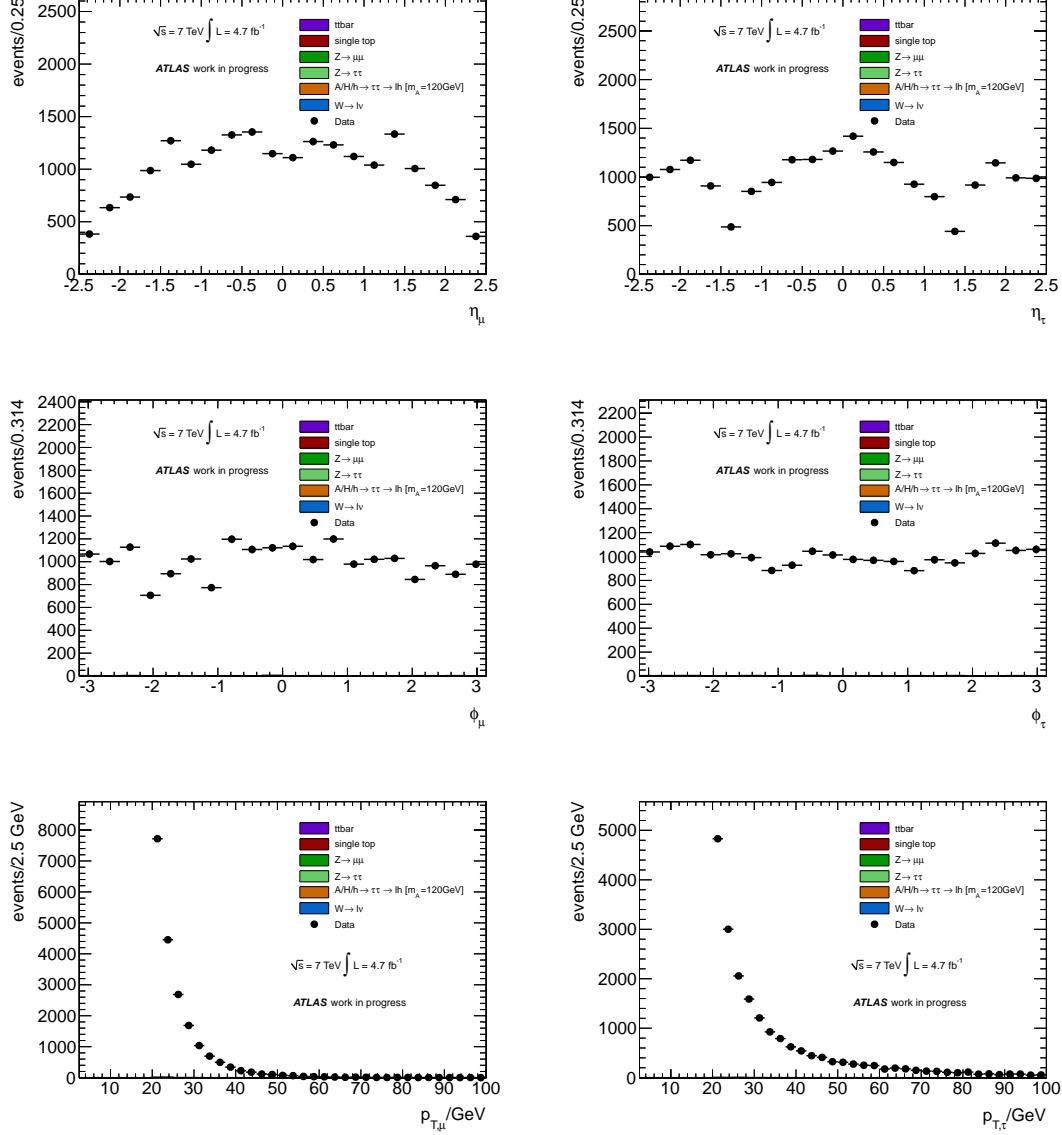


**Figure B.5.:** Plots for the kinematic variables  $\eta$  (first row),  $\Phi$  (second row) and  $p_T$  (third row) for QCD control region D, for  $L_{\text{int}} = 4.7 \text{ fb}^{-1}$ . The muon distributions are depicted on the left, the tau variables are shown on the right. The simulated Monte Carlo background samples are also plotted, but they show too low statistics in this region. It can be seen, that this region is highly dominated by QCD background (difference between the data and the Monte Carlo samples).

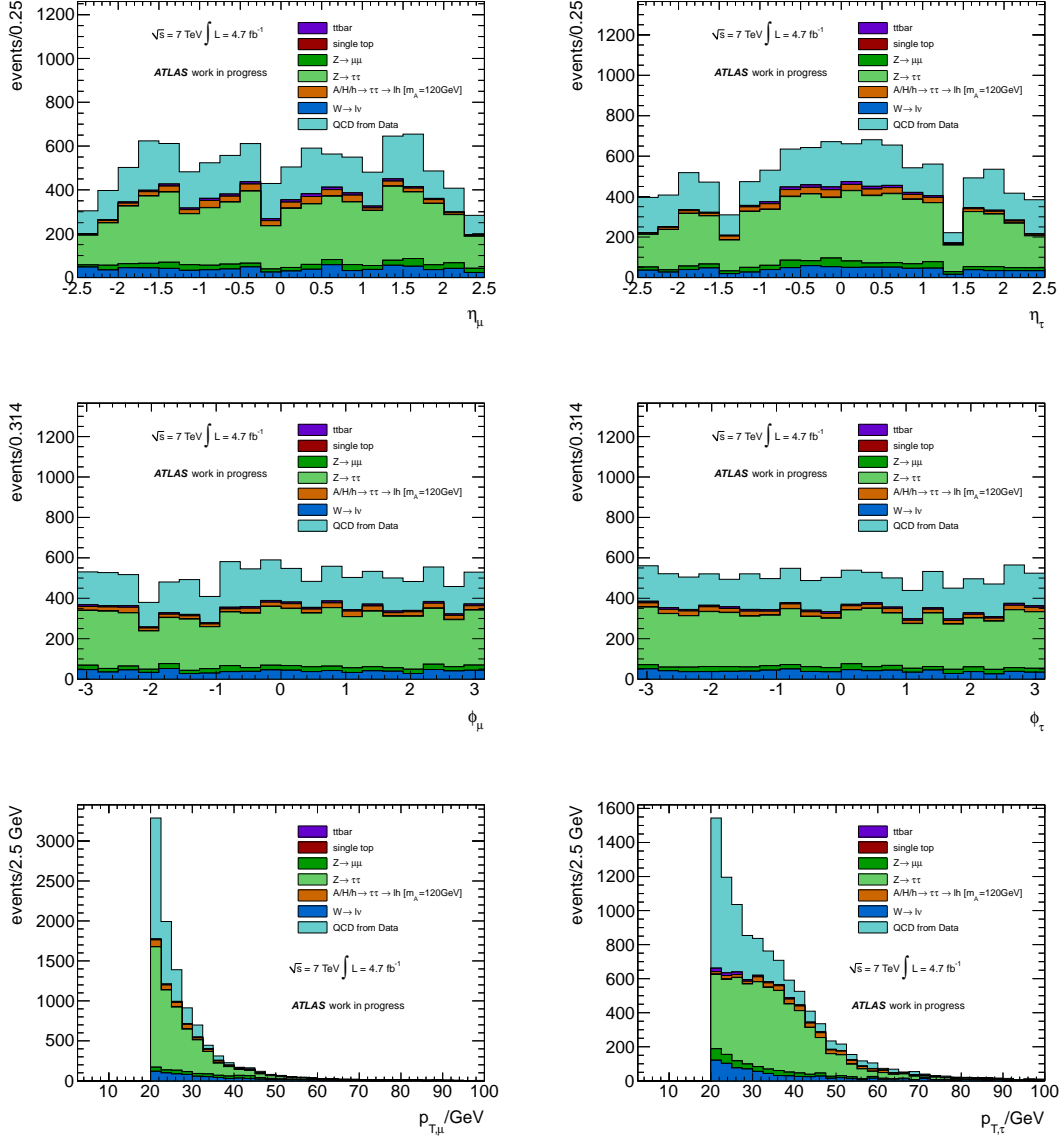


**Figure B.6.:** Plots for the kinematic variables  $\eta$  (first row),  $\Phi$  (second row) and  $p_T$  (third row) for signal region A, for  $L_{\text{int}} = 4.7 \text{ fb}^{-1}$ . The muon distributions are depicted on the left, the tau variables are shown on the right. The QCD background is estimated with the procedure described in Section 4.3.2, using the histograms in Figures B.3, B.4 and B.5.

## C. Appendix - Optimisation of the Event Selection

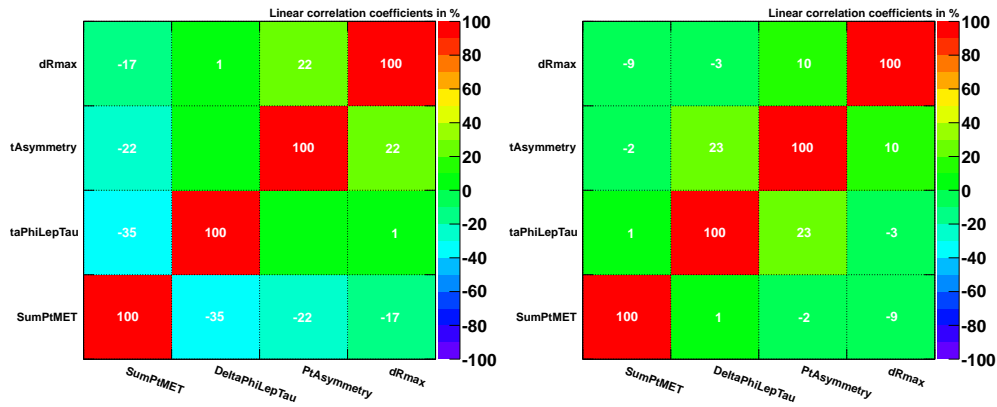


**Figure C.1.:** Linear Correlation Coefficients for the Variables involved in the  $W$ +jets background reduction for the signal (left) and background (right) sample. All Variables used have no linear correlation.

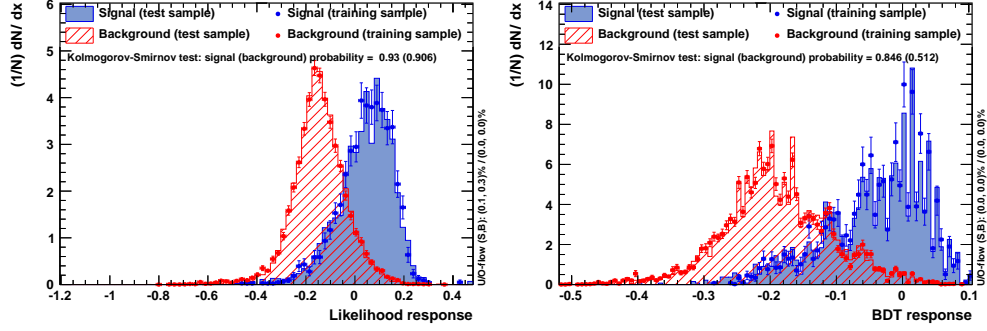


**Figure C.2.:** Overtraining check for the  $W$ +jets background reduction for the Likelihood (left) and BDT (right) classifier respectively. No significant overtraining can be seen.

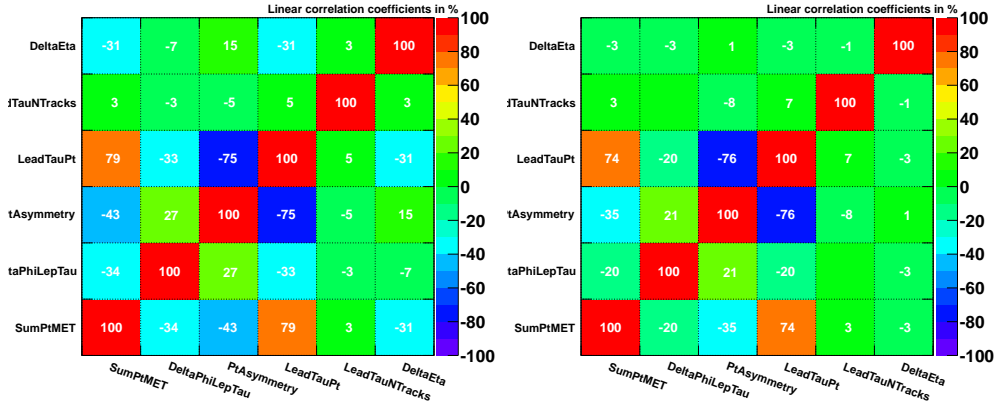


**Figure C.3.:** Linear Correlation Coefficients for the Variables involved in the QCD background reduction for the signal (left) and background (right) sample. All Variables used have no linear correlation between each other

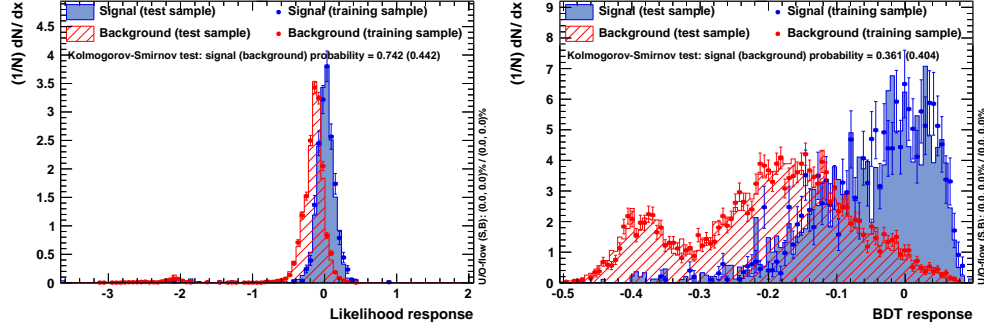


**Figure C.4.:** Overtraining check for the QCD background reduction for the Likelihood (left) and BDT (right) classifier respectively. No significant overtraining can be seen.

Variable	Definition
SumPtMET	$p_{T,\mu} + p_{T,\tau} + E_T^{miss}$
TransMassLepMET	see eq. 4.4
DeltaPhiLepTau	$ \Phi_\mu - \Phi_\tau $
DeltaPhiMETTau	$ \Phi_{MET} - \Phi_\tau $
MuEtCone20Rel	$\frac{etcone20}{p_T}$
MuPtCone40Rel	$\frac{ptcone40}{p_T}$
NJets	number of jets found in the event
MET	missing transverse energy of the event
LeadTauPt	$p_T$ of the hadronic tau candidate with the highest momentum in the event
DeltaEta	$ \eta_\mu - \eta_\tau $
PtAsymmetry	$\frac{p_{T,\mu} - p_{T,\tau}}{p_{T,\mu} + p_{T,\tau}}$
DeltaPhiMETLep	$ \Phi_\mu - \Phi_{MET} $
dRmax	distance between the axis of the hadronic tau candidate and the core track
LeadTauNTracks	number of tracks of the hadronic tau candidate with the highest $p_T$ in the event
DeltaRTauMET	distance $\Delta R$ between the hadronic tau candidate and the missing transverse energy signature

**Table C.1.:** List of all variables considered for multivariate training.

Classifier	Type	Option	Value
Rectangular Cuts	kCuts	FitMethod	MC
		EffMethod	EffSel
		SampleSize	200000
		VarProp	FSmart
Projective Likelihood	kLikelihood	VarTransform	G, D
		CreateMVAPdfs	true
		TransformOutput	true
		NAvEvtPerBin	50
		MinNSmooth	1
		MaxNSmooth	3
		VarTransform	G, D
Boosted Decision Tree	kBDT	BoostType	AdaBoost
		SeparationType	GiniIndex
		CreateMVAPdfs	true
		IgnoreNegWeightsInTraining	true
		NNodesMax	10
		MaxDepth	50
		nCuts	15
		PruneMethod	NoPruning

**Table C.2.:** List of the configuration options used in the multivariate training against the  $W$ +jet background. A description of all options can be found in [66].



Classifier	Type	Option	Value
Rectangular Cuts	kCuts	FitMethod	MC
		EffMethod	EffSel
		SampleSize	200000
		VarProp	FSmart
Projective Likelihood	kLikelihood	VarTransform	G, D
		CreateMVAPdfs	true
		TransformOutput	true
		NAvEvtPerBin	20
		MinNSmooth	1
		MaxNSmooth	1
		VarTransform	G, D
Boosted Decision Tree	kBDT	BoostType	AdaBoost
		SeparationType	GiniIndex
		CreateMVAPdfs	true
		IgnoreNegWeightsInTraining	true
		NNodesMax	5
		MaxDepth	3
		nCuts	25
		PruneMethod	NoPruning
		NTrees	200
		NodePurityLimit	0.5
		nEventsMin	600

**Table C.3.:** List of the configuration options used in the multivariate training against the QCD background. A description of all options can be found in [66].

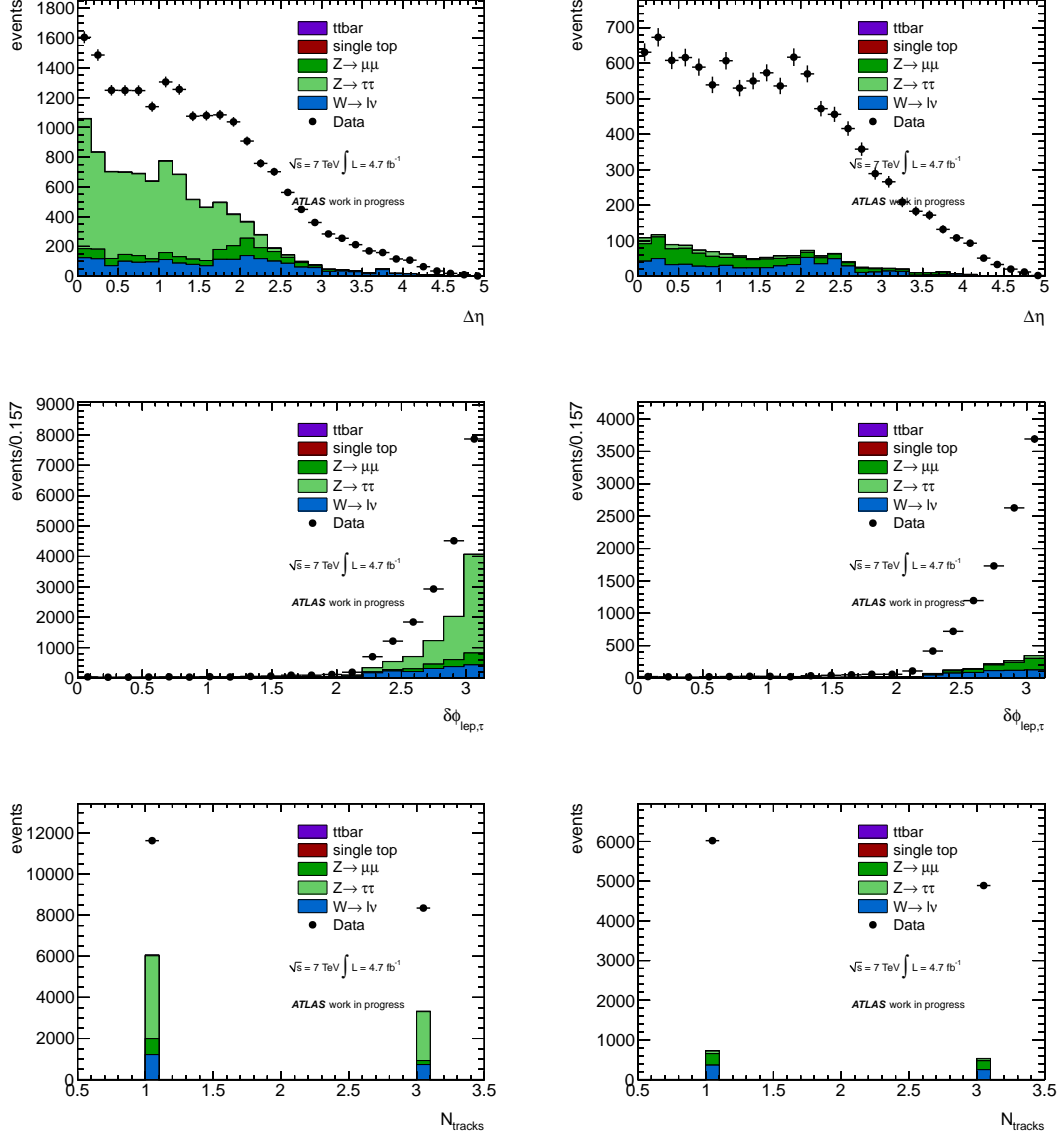


**Figure C.5.:** Control plots for the used QCD training variables, for  $L_{\text{int}} = 4.7 \text{ fb}^{-1}$ . To show that the assumption was correct, that the data shape in region C is equal to the shape of the QCD in region A, the cut on the  $\text{BDT}_{\text{QCD}}$  was inverted and therefore a new QCD enriched region formed. The left column shows the variables for signal region A, after the inverted cut was applied, the right column shows the same for region C. The shown variables are DeltaEta (first row), DeltaPhiLepTau (second row) and LeadNTauTracks (third row)

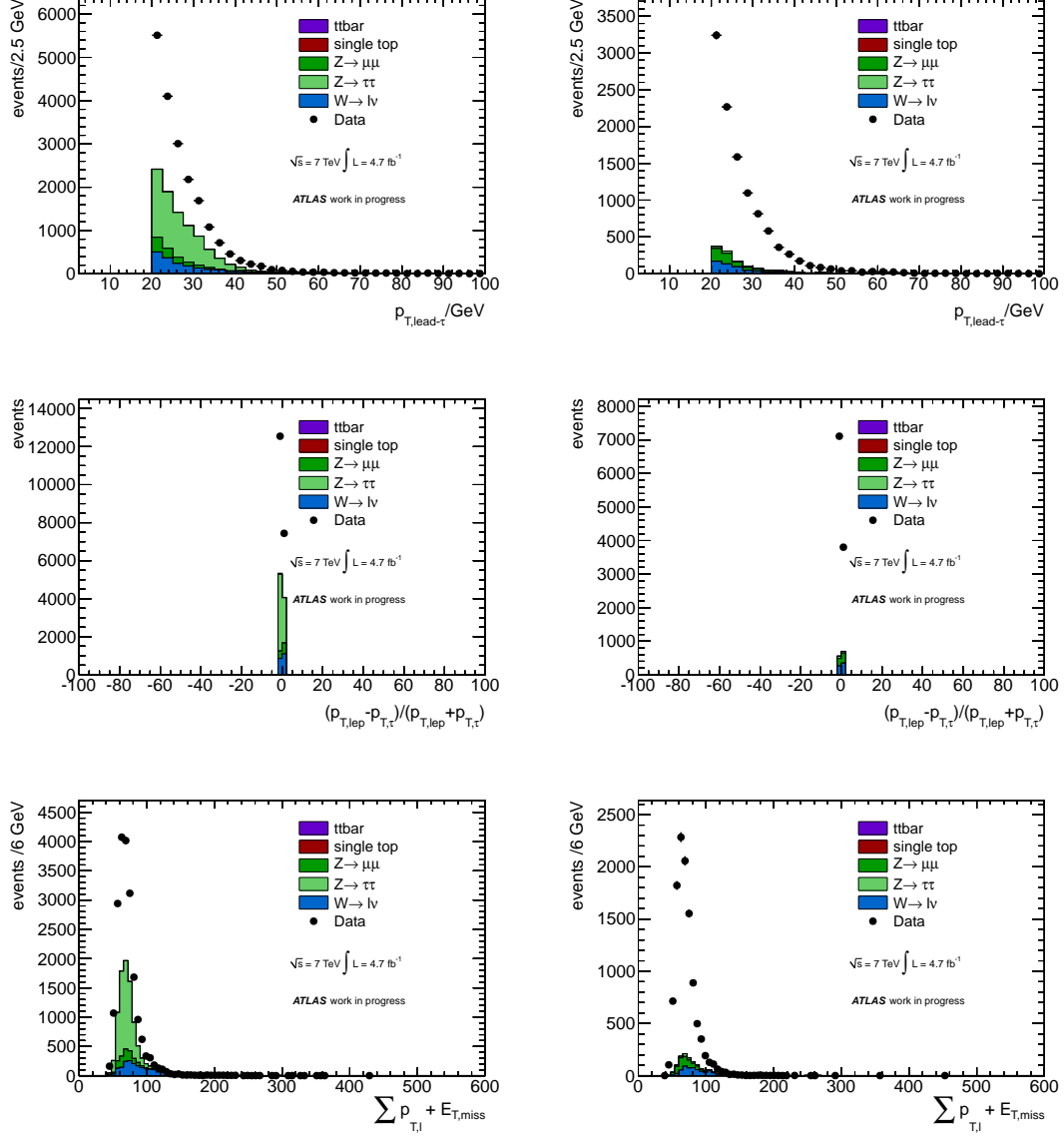


**Figure C.6.:** Control plots for the used QCD training variables, for  $L_{\text{int}} = 4.7 \text{ fb}^{-1}$ . To show that the assumption was correct, that the data shape in region C is equal to the shape of the QCD in region A, the cut on the  $\text{BDT}_{\text{QCD}}$  was inverted and therefore a new QCD enriched region formed. The left column shows the variables for signal region A, after the inverted cut was applied, the right column shows the same for region C. The shown variables are LeadTauPt (first row), PtAsymmetry (second row) and SumPtMET (third row)



## D. Appendix - Systematics

$p_T$ range/GeV	$ \eta  < 1.3$	$1.3 <  \eta  < 1.6$	$ \eta  > 1.6$
1-prong			
15 – 20	5.5 %	5 %	4.5 %
20 – 30	4.5 %	5 %	4.5 %
> 30	3.5 %	5 %	4.5 %
3-prong			
15 – 20	6.5 %	9.5 %	6.5 %
20 – 30	6.5 %	5.5 %	5.5 %
30 – 40	5.5 %	5.5 %	5.5 %
> 40	4.5 %	5 %	5 %

**Table D.1.:** Systematic uncertainties for the energy scale of the hadronic tau, taken from [58].

Process	Region B	Region C	Region D
$\gamma^*/Z \rightarrow \mu^+\mu^-/e^+e^-$	2	44	1
$\gamma^*/Z \rightarrow \tau^+\tau^-$	54	32	5
$W \rightarrow l\nu_l$	8	70	2
top ( $t\bar{t}$ and single $t$ events)	26	4	19
$A/H/h \rightarrow \tau_\mu\tau_{had}$	5	1	0
data	6194	765	5394

**Table D.2.:** Event yield for all three QCD control regions after the new event selection was applied, for  $L_{\text{int}} = 4.7\text{fb}^{-1}$ . The QCD content in each region is obtained by subtracting the simulated background from the data. In all three regions the contributions from the signal are negligible.

Process	Region B		Region C		Region D	
	$\Delta N_{\text{events}}$	Uncertainty	$\Delta N_{\text{events}}$	Uncertainty	$\Delta N_{\text{events}}$	Uncertainty
$\gamma^*/Z \rightarrow \mu^+\mu^-/e^+e^-$	$\pm 1$	52 %	$\pm 7$	15.9 %	$\pm 1$	79.3 %
$\gamma^*/Z \rightarrow \tau^+\tau^-$	$\pm 7$	13.2 %	$\pm 4$	10.9 %	$\pm 2$	39.4 %
$W \rightarrow l\nu_l$	$\pm 2$	25.7 %	$\pm 9$	13.1 %	$\pm 1$	35.1 %
top	$\pm 2$	8.6 %	$\pm 1$	16.6 %	$\pm 2$	9.9 %
$A/H/h \rightarrow \tau_\mu\tau_{had}$	$\pm 2$	32.8 %	$\pm 1$	74.4 %	$\pm 0$	0 %
data	$\pm 79$	1.3 %	$\pm 28$	3.6 %	$\pm 73$	1.4 %

**Table D.3.:** Statistical Uncertainties for the QCD control regions for all samples and data, for  $L_{\text{int}} = 4.7 \text{ fb}^{-1}$ . For each region, the fluctuation in the event yield as well as the relative change in the event yield is given.

Process	Region B Uncertainty	Region C Uncertainty	Region D Uncertainty
$\gamma^*/Z \rightarrow \mu^+\mu^-/e^+e^-$	$\pm 19.6 \%$	$+34.2 \%$ $-26.6 \%$	$\pm 46.3 \%$
$\gamma^*/Z \rightarrow \tau^+\tau^-$	$+20 \%$ $-100.4 \%$	$+34.7 \%$ $-92.5 \%$	$+47.7 \%$ $-47.2 \%$
$W \rightarrow l\nu_l$	$+37.3 \%$ $-26.7 \%$	$+34.1 \%$ $-35.3 \%$	$+49.5 \%$ $-57.3 \%$
top	$+19.3 \%$ $-21.8 \%$	$+34.4 \%$ $-72.5 \%$	$+46.6 \%$ $-46.4 \%$
$A/H/h \rightarrow \tau_\mu\tau_{had}$	$+27.7 \%$ $-33.9 \%$	$+34.3 \%$ $-37.2 \%$	$+46.9 \%$ $-50.2 \%$

**Table D.4.:** Total Systematic Uncertainties for the QCD control regions for all samples and data, for  $L_{\text{int}} = 4.7 \text{ fb}^{-1}$ . For each region, the relative change in the event yield is given.

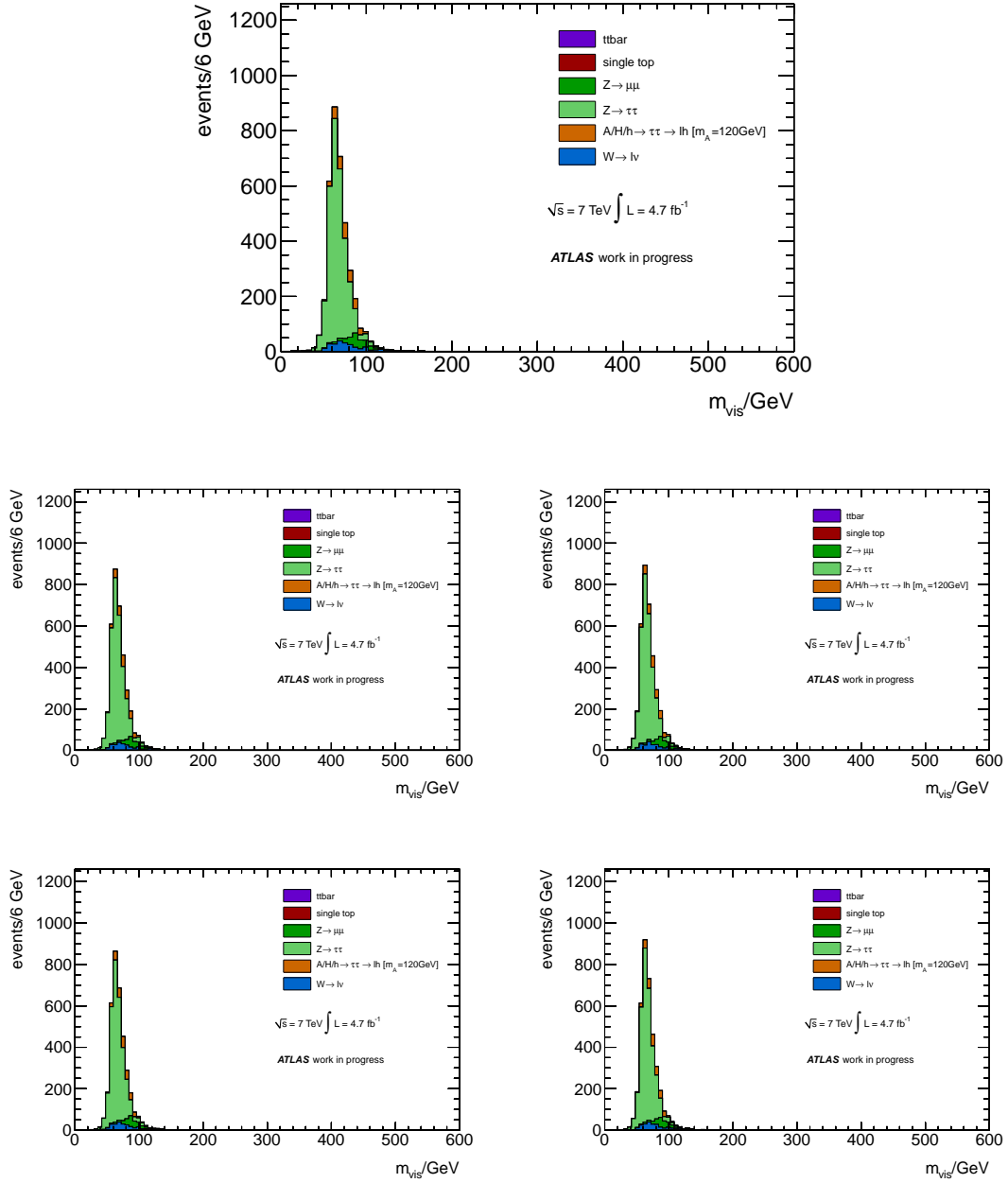


**Figure D.1.:** The  $m_{vis}$  distribution after the new event selection had been applied (first row) and with the muon systematics applied, for  $L_{int} = 4.7 \text{ fb}^{-1}$ : The left plot in the second row shows the change in the distribution, after applying the muon resolution systematic, whilst the right plot in the second row shows the event yield after adding the muon identification efficiency. The third row shows the energy scale systematics for lowering the muon  $p_T$  (left) and raising the muon  $p_T$  (right).

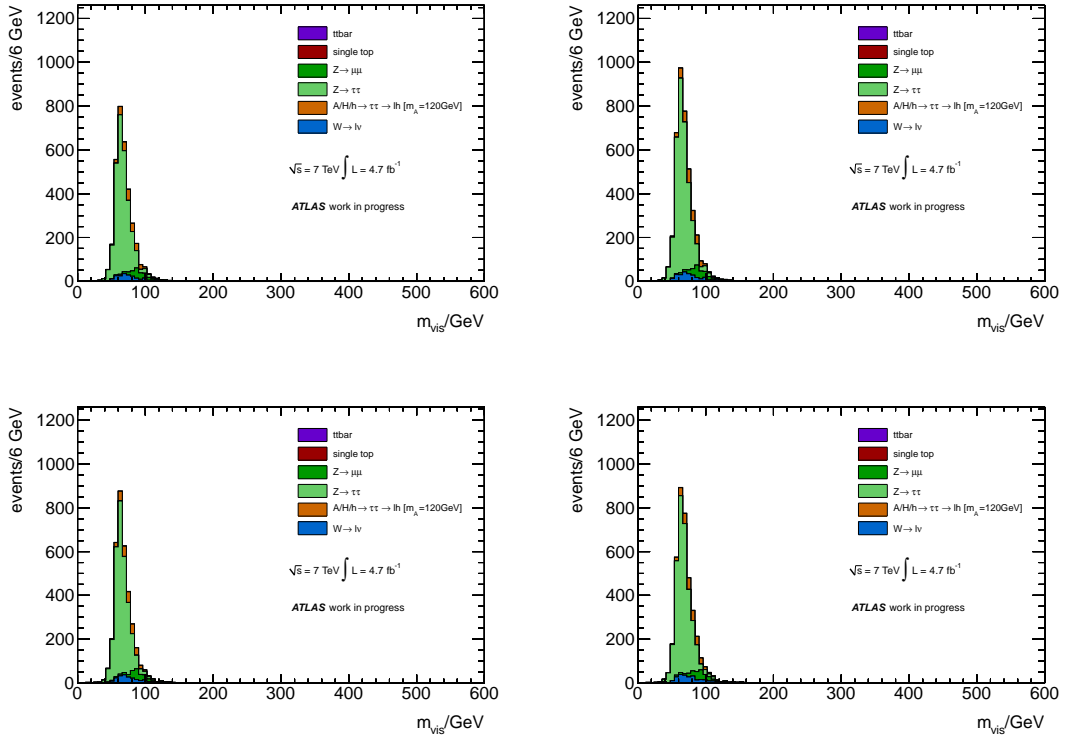


**Figure D.2.:** The  $m_{vis}$  distribution after the new event selection had been applied with the hadronic tau systematics applied, for  $L_{\text{int}} = 4.7 \text{ fb}^{-1}$ : The first row shows the event yield after applying the tau efficiency for negative scaling (left) and positive scaling (right). The second row depicts the energy scale changes, for lowering the tau  $p_T$  (left) and raising the tau  $p_T$  (right).



## E. Appendix - Results

$\tan\beta$	90	110	120	130	140	170	200	250	300
5	36	29	32	42	23	12	6	2	1
10	136	101	98	106	75	53	31	14	5
15	308	229	220	215	169	122	72	36	16
20	551	413	399	369	306	218	131	68	32
25	863	651	636	568	486	343	206	108	52
30	1248	946	932	813	709	495	298	156	78
35	1706	1300	1290	1107	976	677	407	215	108
40	2239	1713	1709	1449	1288	886	534	282	143
45	2848	2187	2193	1844	1643	1126	678	359	182
50	3536	2727	2745	2293	2045	1396	840	444	226

**Table E.1.:** The Event yield for different Higgs masses and  $\tan\beta$  before applying the optimised event selection, for  $L_{\text{int}} = 4.7 \text{ fb}^{-1}$ .

$\tan\beta$	90	110	120	130	140	170	200	250	300
5	18	20	22	28	16	8	3	1	0
10	68	70	69	75	55	36	18	7	2
15	154	158	154	154	125	82	42	18	7
20	274	284	280	266	227	147	76	33	14
25	430	448	446	410	361	232	120	53	24
30	621	650	654	588	527	335	173	77	35
35	849	893	904	802	726	458	236	106	49
40	1113	1177	1198	1050	958	599	310	139	65
45	1416	1503	1537	1337	1223	762	394	177	82
50	1759	1873	1924	1663	1522	944	487	219	102

**Table E.2.:** The Event yield for different Higgs masses and  $\tan\beta$  after applying the new event selection with the  $\text{BDT}_W$  and  $\text{BDT}_{\text{QCD}}$ , for  $L_{\text{int}} = 4.7 \text{ fb}^{-1}$ .

$\tan\beta$	90	110	120	130	140	170	200	250	300
5	21	21	23	28	16	7	3	1	0
10	78	76	72	77	56	35	16	5	1
15	176	172	161	158	127	80	37	12	3
20	315	309	292	272	231	144	67	22	7
25	493	488	466	420	367	226	105	35	11
30	713	708	682	603	537	327	152	50	16
35	974	973	943	823	740	447	208	69	23
40	1279	1282	1250	1078	977	586	273	90	30
45	1627	1637	1603	1372	1246	744	347	115	39
50	2019	2040	2006	1707	1551	922	429	1142	48

**Table E.3.:** The Event yield for different Higgs masses and  $\tan\beta$  after applying the new event selection with the the  $\text{BDT}_W$  and  $\text{Likelihood}_{\text{QCD}}$ , for  $L_{\text{int}} = 4.7 \text{ fb}^{-1}$ .

$\tan\beta$	90	110	120	130	140	170	200	250	300
5	19	21	23	30	17	8	4	1	0
10	73	73	72	79	57	37	19	8	3
15	164	165	162	163	129	85	43	19	8
20	292	297	293	281	235	152	78	36	16
25	458	468	467	433	373	239	124	57	26
30	662	680	685	622	546	346	179	82	39
35	905	934	947	847	752	473	244	113	54
40	1187	1230	1255	1110	992	620	320	149	72
45	1511	1571	1610	1413	1266	787	407	189	92
50	1876	1959	2015	1758	1576	976	504	234	114

**Table E.4.:** The Event yield for different Higgs masses and  $\tan\beta$  after applying the new event selection with the the  $\text{BDT}_W$  and  $\text{Cut}_{\text{QCD}}$ , for  $L_{\text{int}} = 4.7 \text{ fb}^{-1}$ .

$\tan\beta$	90	110	120	130	140	170	200	250	300
5	18	20	22	29	17	9	5	2	0
10	70	70	69	77	57	42	24	10	4
15	157	158	154	158	130	96	56	26	11
20	280	285	280	273	236	172	101	49	22
25	438	449	446	421	376	271	159	79	36
30	633	653	654	603	549	391	231	114	54
35	866	896	904	822	757	535	315	156	75
40	1136	1181	1198	1077	998	701	413	206	99
45	1445	1508	1537	1371	1274	890	525	261	126
50	1794	1880	1923	1706	1586	1104	650	324	156

**Table E.5.:** The Event yield for different Higgs masses and  $\tan\beta$  after applying the new event selection with the the  $\text{Likelihood}_W$  and  $\text{BDT}_{\text{QCD}}$ , for  $L_{\text{int}} = 4.7 \text{ fb}^{-1}$ .

$\tan\beta$	90	110	120	130	140	170	200	250	300
5	22	22	22	29	17	9	4	1	0
10	81	77	71	79	58	40	20	6	1
15	183	174	161	162	131	93	48	15	4
20	326	313	292	279	239	166	87	29	9
25	511	494	465	430	380	261	137	46	14
30	739	718	681	618	556	377	198	66	21
35	1009	986	941	842	765	516	270	91	29
40	1324	1299	1247	1103	1009	676	354	120	39
45	1685	1659	1599	1404	1288	858	450	153	50
50	2092	2068	2002	1746	1603	1064	557	189	62

**Table E.6.:** The Event yield for different Higgs masses and  $\tan\beta$  after applying the new event selection with the the Likelihood<sub>W</sub> and Likelihood<sub>QCD</sub>, for  $L_{\text{int}} = 4.7 \text{ fb}^{-1}$ .

$\tan\beta$	90	110	120	130	140	170	200	250	300
5	20	21	23	31	18	9	5	2	1
10	75	73	72	82	60	43	25	11	4
15	170	167	163	168	135	100	58	28	12
20	303	300	295	290	246	179	105	53	24
25	476	472	470	447	390	281	165	84	40
30	687	686	689	641	571	406	239	121	59
35	939	943	953	873	786	554	326	167	82
40	1232	1242	1263	1144	1037	726	427	219	109
45	1568	1586	1620	1456	1323	922	543	278	139
50	1947	1977	2028	1811	1646	1144	673	345	172

**Table E.7.:** The Event yield for different Higgs masses and  $\tan\beta$  after applying the new event selection with the the Likelihood<sub>W</sub> and Cut<sub>QCD</sub>, for  $L_{\text{int}} = 4.7 \text{ fb}^{-1}$ .

$\tan\beta$	90	110	120	130	140	170	200	250	300
5	16	17	19	23	13	5	2	0	0
10	58	61	62	63	47	26	11	2	0
15	132	138	139	129	107	59	25	6	1
20	235	249	252	223	195	106	45	11	3
25	368	392	401	345	311	167	72	18	5
30	531	570	588	495	455	242	104	26	7
35	726	783	813	675	626	331	142	36	9
40	952	1031	1077	885	827	433	186	47	13
45	1211	1317	1382	1126	1055	550	236	60	16
50	1504	1641	1729	1401	1313	682	292	74	20

**Table E.8.:** The Event yield for different Higgs masses and  $\tan\beta$  after applying the new event selection with the the Cut<sub>W</sub> and BDT<sub>QCD</sub>, for  $L_{\text{int}} = 4.7 \text{ fb}^{-1}$ .

$\tan\beta$	90	110	120	130	140	170	200	250	300
5	18	18	20	23	14	5	2	0	0
10	67	65	64	63	48	25	10	2	0
15	150	148	144	131	109	58	23	5	1
20	268	266	261	226	198	105	42	10	3
25	419	420	416	350	316	164	66	16	5
30	606	610	609	502	462	238	95	24	7
35	828	838	842	685	636	325	130	32	9
40	1086	1104	1116	897	839	426	170	43	13
45	1382	1409	1431	1143	1071	541	216	54	16
50	1716	1757	1791	1421	1333	670	268	67	20

**Table E.9.:** The Event yield for different Higgs masses and  $\tan\beta$  after applying the new event selection with the the  $\text{Cut}_W$  and  $\text{Likelihood}_{\text{QCD}}$ , for  $L_{\text{int}} = 4.7 \text{ fb}^{-1}$ .

$\tan\beta$	90	110	120	130	140	170	200	250	300
5	16	18	20	24	14	6	2	0	0
10	59	63	64	65	48	27	11	3	1
15	132	143	144	134	110	62	26	7	2
20	235	258	260	231	200	110	46	12	3
25	368	406	415	357	318	174	73	19	5
30	532	591	608	512	466	251	106	28	7
35	726	811	840	698	642	343	145	39	10
40	953	1068	1112	915	847	449	190	51	14
45	1212	1364	1427	1165	1081	571	241	65	17
50	1505	1700	1786	1449	1346	708	299	80	22

**Table E.10.:** The Event yield for different Higgs masses and  $\tan\beta$  after applying the new event selection with the the  $\text{Cut}_W$  and  $\text{Cut}_{\text{QCD}}$ , for  $L_{\text{int}} = 4.7 \text{ fb}^{-1}$ .

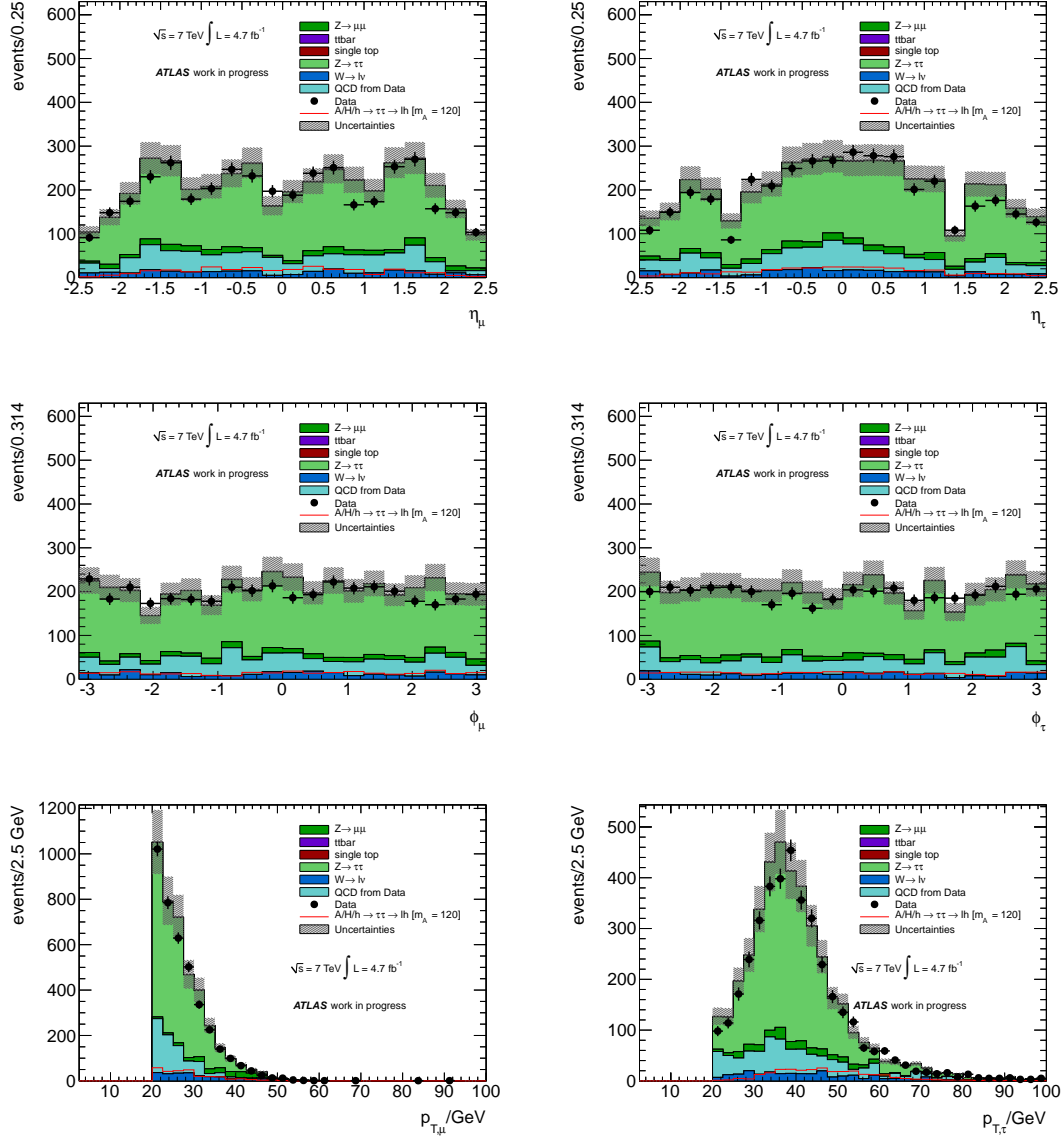


**Figure E.1.:** Plots for the kinematic variables  $\eta$  (first row),  $\Phi$  (second row) and  $p_T$  (third row) after applying the optimised event selection, with data and uncertainties, for  $L_{\text{int}} = 4.7 \text{ fb}^{-1}$ . The muon distributions are depicted on the left, the tau variables are shown on the right.



# Bibliography

- [1] O. Igonkina. *Supersymmetry and Beyond Standard Model Higgs Searches at ATLAS*. ATL-PHYS-PROC-2012-023, 2012.
- [2] D. Griffiths. *Introduction to Elementary Particle Physics*. WILEY-VCH Verlag GmbH & Co. KGaA, Weinheim, second edition, 2008.
- [3] M. Herrero. *The Standard Model*. arXiv:hep-ph/9812242v1.
- [4] K. Nakamura et al. *Review of Particle Physics*. J. Phys. G: Nucl. Part. Phys. 37 075021, 2012.
- [5] Z. Ligeti. *Introduction to Heavy Meson Decays and CP Asymmetries*. eConf C020805 (2002) L02.
- [6] J. Greensite R. Alkofer. *Quark Confinement: The Hard Problem of Hadron Physics*. J. Phys. G: Nucl. Part. Phys. 34 S3.
- [7] P. Langacker. *Introduction to the Standard Model and Electroweak Physics*. arXiv:0901.0241v1.
- [8] A. Pich. *Aspects of Quantum Chromodynamics*. arXiv:hep-ph/0001118v1.
- [9] W. Hollik. *Electroweak Theory*. J. Phys.: Conf. Ser. 53 7, 2006.
- [10] P. Benton. *Precision Electroweak Tests of the Standard Model*. Rep. Prog. Phys. 65 1271.
- [11] K. Fukushima et al. *The Chiral Magnetic Effect*. Phys. Rev. D78 074033, 2008.
- [12] G. Altarelli. *The Standard Electroweak Theory and Beyond*. arXiv:hep-ph/9811456v1.
- [13] B. Povh et al. *Teilchen und Kerne - Eine Einführung in die physikalischen Konzepte*. Springer-Verlag Berlin Heidelberg, Heidelberg, eight edition, 2009.

- [14] C. Quigg. *Electroweak Symmetry Breaking and the Higgs Sector*. Acta. Phys. Polon. B30 2145-2192.
- [15] S. P. Martin. *A Supersymmetry Primer*. arXiv:hep-ph/9709356v6.
- [16] D. I. Kazakov. *Beyond the Standard Model (In search of Supersymmetry)*. arXiv:hep-ph/0012288v2.
- [17] G. Bertone et al. *Particle Dark Matter: Evidence, Candidates and Constraints*. Phys.Rept.405:279-390.
- [18] S. Heinemeyer. *MSSM Higgs Physics at Higher Orders*. Int.J.Mod.Phys.A21:2659-2772.
- [19] P. Bryant L. Evans. *LHC machine*. Institute of Physics Publishing, JINST 3 S08001, 2008.
- [20] European Laboratory for Particle Physics. *Background Information on LEP, CERN'S Large Electron-Positron Collider*. <http://cdsweb.cern.ch/record/884035/files/CM-P00056254.pdf>.
- [21] European Organisation for Nuclear Research. *LHC Design Report, Vol I*. <http://cdsweb.cern.ch/record/782076>.
- [22] European Organisation for Nuclear Research. *LHC Design Report, Vol III*. <https://cdsweb.cern.ch/record/823808>.
- [23] The ATLAS Collaboration. *The ATLAS Experiment at the CERN Large Hadron Collider*. Institute of Physics Publishing, JINST 3 S08003.
- [24] The CMS Collaboration. *The CMS experiment at the CERN LHC*. Institute of Physics Publishing, JINST 3 S08004.
- [25] The LHCb Collaboration. *The LHCb Detector at the LHC*. Institute of Physics Publishing, JINST 3 S08005.
- [26] European Organisation for Nuclear Research. *LHC Design Report, Vol II*. [https://edms.cern.ch/file/445914/9/Vol\\_2\\_Chapter\\_2.pdf](https://edms.cern.ch/file/445914/9/Vol_2_Chapter_2.pdf), 2004.
- [27] The ALICE Collaboration. *The ALICE Experiment at the CERN LHC*. Institute of Physics Publishing, JINST 3 S08002.



- [28] F. Gianotti. *Update on the Standard Model Higgs Searches in ATLAS*. joint CMS/ATLAS seminar.
- [29] G. Tonelli. *Update on the Standard Model Higgs Searches in CMS*. joint CMS/ATLAS seminar.
- [30] H. Abreu et al. *Performance of the electronic readout of the ATLAS liquid argon calorimeters*. Institute of Physics Publishing, JINST 5 P09003.
- [31] Cheuk-Yin Wong. *Introduction to High-Energy Heavy-Ion Collisions*. World Scientific Publishing Co Pte Ltd, [http://www.worldscibooks.com/etextbook/1128/1128\\_chap2\\_3.pdf](http://www.worldscibooks.com/etextbook/1128/1128_chap2_3.pdf), 1994.
- [32] Cheuk-Yin Wong. *Introduction to High-Energy Heavy-Ion Collisions*. World Scientific Publishing Co Pte Ltd, [http://www.worldscibooks.com/etextbook/1128/1128\\_chap2\\_4.pdf](http://www.worldscibooks.com/etextbook/1128/1128_chap2_4.pdf), 1994.
- [33] A. Ahmad et al. *The silicon microstrip sensors of the ATLAS semiconductor tracker*. Nuclear Instruments & Methods in Physics Research, Nucl. Instrum. Meth. A 578 (2007) 98.
- [34] G. Aad et al. *ATLAS pixel detector electronics and sensors*. Institute of Physics Publishing, JINST 3 P07007.
- [35] E. Abat et al. *The ATLAS Transition Radiation Tracker (TRT) proportional drift tube: design and performance*. Institute of Physics Publishing, JINST 3 P02013.
- [36] J. Wotschack. *ATLAS Muon Chamber Construction Parameters for CSC, MDT, and RPC chambers*. ATLAS Note, ATL-MUON-PUB-2008-006.
- [37] P. Bagnaia et al. *Calibration model for the MDT chambers of the ATLAS Muon Spectrometer*. ATLAS Note, ATL-MUON-PUB-2008-004.
- [38] C. Gabaldon. *Performance of the ATLAS Trigger System*. Institute of Physics Publishing, JINST 7 C01092.
- [39] The ATLAS Collaboration. *Search for neutral MSSM Higgs bosons decaying to  $\tau^+\tau^-$  pairs in proton-proton collisions at  $\sqrt{s} = 7$  TeV with the ATLAS Experiment*. ATLAS-CONF-2011-024, 2011.
- [40] M. Spira et al. *Higgs Boson Production at the LHC*. Nucl. Phys. B453:17-82, 1995.

- [41] C. Jackson S. Dawson. *Higgs Production in Association with Bottom Quarks at Hadron Colliders*. Mod. Phys. Lett. A21 89-110, 2006.
- [42] M. Spira. *HIGLU: A Program for the Calculation of the Total Higgs Production Cross Section at Hadron Colliders via Gluon Fusion including QCD Corrections*. arXiv:hep-ph/9510347v1, 1995.
- [43] W. Kilgore R. Harlander. *Next-to-Next-to-Leading Order Higgs Production at Hadron Colliders*. Phys. Rev. Lett. 88 201801, 2002.
- [44] R. Harlander et al. *Bottom-quark associated Higgs-boson production: reconciling the four- and five-flavour scheme approach*. arXiv:1112.3478v1, 2011.
- [45] M. Mühlleitner et al. *MSSM Higgs Boson Production via Gluon Fusion: The Large Gluino Mass Limit*. JHEP 0904 023, 2009.
- [46] T. Aaltonen et al. *Search for Higgs Bosons Produced in Association with b-Quarks*. arXiv:1106.4782v2, 2012.
- [47] S. Kuehn. *Physics with  $\tau$  leptons in ATLAS*. ATL-PHYS-PROC-2011-143, 2011.
- [48] D. Gerdes. *Top Quark Physics Results from CDF and D0*. ECONF C 960625:OPS005, 2011.
- [49] T. Gleisberg et al. *Event generation with SHERPA 1.1*. JHEP 0902 007, 2009.
- [50] T. Sjöstrand et al. *PYTHIA 6.4 Physics and Manual*. JHEP 0605 026, 2006.
- [51] M. Carena et al. *Suggestions for Benchmark Scenarios for MSSM Higgs Boson Searches at Hadron Colliders*. Eur. Phys. J. C26:601-607, 2003.
- [52] The ATLAS Collaboration. *Search for neutral MSSM Higgs boson decaying to  $\tau^+\tau^-$  pairs in proton-proton collisions at  $\sqrt{s} = 7$  TeV with the ATLAS detector*. ATLAS-CONF-2011-132, 2011.
- [53] M. Mangano et al. *ALPGEN, a generator for hard multiparton processes in hadronic collisions*. JHEP 0307 001, 2003.
- [54] B. Webber S. Frixione. *The MC@NLO 3.3 Event Generator*. arXiv:hep-ph/0612272v1, 2006.
- [55] E. Richter-Was B. Kersevan. *The Monte Carlo Event Generator ACERMC 2.0 with Interfaces to PYTHIA 6.2 and HERWIG 6.5*. arXiv:hep-ph/0405247v1, 2004.

- [56] The ATLAS Collaboration. *Muon Performance in Minimum Bias pp Collision Data at  $\sqrt{s} = 7$  TeV with ATLAS*. ATLAS-CONF-2010-036, 2010.
- [57] The ATLAS Collaboration. *Search for the Standard Model Higgs boson in the  $H \rightarrow \tau^+\tau^-$  decay mode with  $4.7\text{ fb}^{-1}$  of ATLAS data at  $\sqrt{s} = 7$  TeV*. ATLAS-CONF-2012-014, 2012.
- [58] The ATLAS Collaboration. *Performance of the Reconstruction and Identification of Hadronic Tau Decays with ATLAS*. ATLAS-CONF-2011-152, 2011.
- [59] M. Cacciari et al. *The anti- $k_t$  jet clustering algorithm*. JHEP 0804 063, 2008.
- [60] The ATLAS Collaboration. *Performance of the Missing Transverse Momentum Reconstruction in Proton-Proton Collisions at  $\sqrt{s} = 7$  TeV with ATLAS*. Eur. Phys. J. C 72 1844, 2012.
- [61] A. Banfi et al. *NLL+NNLO predictions for jet-veto efficiencies in Higgs-boson and Drell-Yan production*. arXiv:1203.5773v1, 2012.
- [62] G. Bozzi et al. *Transverse-momentum resummation and the spectrum of the Higgs boson at the LHC*. Nucl. Phys. B737:73-120, 2006.
- [63] The ATLAS Collaboration. *Data-Quality Requirements and Event Cleaning for Jets and Missing Transverse Energy Reconstruction with the ATLAS Detector in Proton-Proton Collisions at a Center-of-Mass Energy of  $\sqrt{s} = 7$  TeV*. ATLAS-CONF-2010-038, 2010.
- [64] The ATLAS Collaboration.  *$Z \rightarrow \tau\tau$  cross section measurement on proton-proton collision at 7 TeV with the ATLAS experiment*. ATLAS-CONF-2012-006, 2012.
- [65] The ATLAS Collaboration. *Measurement of the Mis-identification Probability of  $\tau$  Leptons from Hadronic Jets and from Electrons*. ATLAS-CONF-2011-113, 2011.
- [66] A. Høcker et al. *TMVA 4 - Toolkit for Multivariate Data Analysis with ROOT - Users Guide*, November 3 2009.
- [67] The ATLAS Collaboration. *Reconstruction, Energy Calibration, and Identification of Hadronically Decaying Tau Leptons in the ATLAS Experiment*. ATLAS-CONF-2011-077, 2011.
- [68] T. Bristow et al. *Search for Neutral MSSM Higgs Bosons  $H \rightarrow \tau^+\tau^- \rightarrow l\tau_h$  produced in 7 TeV Collisions with the ATLAS Detector*. ATL-COM-PHYS-2012-094, 2012.

- [69] The ATLAS Collaboration. *Luminosity Determination in pp Collisions at  $\sqrt{s} = 7$  TeV using the ATLAS Detector in 2011*. ATLAS-CONF-2011-116, 2011.
- [70] S. Dittmaier et al. *Handbook of LHC Higgs cross sections: 1. Inclusive observables*. arXiv:1101.0593v3, 2011.
- [71] S. Dittmaier et al. *Handbook of the LHC Higgs Cross Sections: 2. Differential Distributions*. arXiv:1201.3084v1, 2012.
- [72] A. Salvucci. *Measurement of muon momentum resolution of the ATLAS detector*. ATL-PHYS-PROC-2012-013, 2012.
- [73] C. Ander et al. *Search for Standard Model  $H \rightarrow \tau^+\tau^- \rightarrow l\tau_h$  with the ATLAS Detector in 7 TeV Proton-Proton Collisions*. ATL-COM-PHYS-2012-037, 2012.
- [74] J. Schaarschmidt. *The Discovery Potential of Neutral Supersymmetric Higgs Bosons with Decay to Tau Pairs at the ATLAS Experiment*. CERN-THESIS-2010-164, 2010.
- [75] G. Cowan et al. *Asymptotic formulae for likelihood-based tests of new physics*. Eur. Phys. J. C71 1554, 2011.

# Danksagung

An dieser Stelle möchte ich mich bei der Teilchenphysik-Gruppe am Institut für Kern- und Teilchenphysik bedanken. Insbesondere gilt mein Dank meinen Betreuern, Dr. Wolfgang Mader und Jun.-Prof. Arno Straessner, die mir die Diplomarbeit am IKTP ermöglicht und mich die gesamte Zeit über unterstützt haben. Des Weiteren möchte ich der ATLAS Arbeitsgruppe am IKTP danken. Insbesondere hervorheben möchte ich Felix Friedrich, Christian Gumpert, Marcus Morgenstern und Sebastian Wahrmund für ihre Hilfe in allen technischen und physikalischen Fragen, sowie für eine konstruktive Arbeitsatmosphäre.

Ferner möchte ich meinen Eltern danken, die mir diese Ausbildung ermöglicht und mich immer finanziell und moralisch unterstützt haben. Besonderer Dank gilt auch meinen Freunden, für den Rückhalt und den nötigen Ausgleich neben der Arbeit.

Finally, I would like to thank my fiancé Andrew Caruana for all his support and motivation during difficult times. Furthermore, my thanks goes to his family, for their encouragement throughout the last year.

# Erklärung

Hiermit versichere ich, dass ich die vorliegende Arbeit ohne unzulässige Hilfe Dritter und ohne Benutzung anderer als der angegebenen Hilfsmittel angefertigt habe. Die aus fremden Quellen direkt oder indirekt übernommenen Gedanken sind als solche kenntlich gemacht. Die Arbeit wurde bisher weder im Inland noch im Ausland in gleicher oder ähnlicher Form einer anderen Prüfungsbehörde vorgelegt.

Stefanie Langrock  
Dresden, Mai 2012